Diss. ETH No. 18214

Emissions-Controlled Diesel Engine

A dissertation submitted to the
SWISS FEDERAL INSTITUTE OF TECHNOLOGY ZURICH
for the degree of
Doctor of Sciences

presented by

Ezio Alfieri

Dipl. Masch.-Ing. ETH
born 30 August 1979
citizen of Pedrinate, TI

accepted on the recommendation of

Prof. Dr. L. Guzzella, examiner
Prof. Dr. H. P. Geering, co-examiner

2009

"When I'm driving, I'm happy!"
Giovanni Piffaretti (December 20th, 2007)

Abstract

Legislation concerning the pollutant emissions of diesel passenger cars is becoming increasingly restrictive, especially for NO_x and particulate matter (PM). A novel approach to control the pollutant emissions in diesel engines is thus proposed that extends the standard feedforward control in the air and fuel path with a true emissions-feedback structure. In order to prove the feasibility of such an approach, a multivariable emissions-feedback controller is designed for the NO_x emissions and for the air/fuel ratio, which is used as an indicator for the PM emissions, due to the fact that compact and low-cost PM sensors are not yet commercially available. The controlled inputs are the command signal of the exhaust gas recirculation (EGR) valve and the injection timing. Besides the boost pressure that is regulated independently by the standard controller, those are the inputs that most significantly affect the formation of NO_x and PM emissions. Moreover, with this choice, the resulting $2{\times}2$ system is reduced to a convenient triangular structure.

Since the new sensors are sensitive to pressure variations, they have to be placed in the low-pressure tract of the exhaust manifold, i.e., downstream of the turbine. Obviously, time delays due to the gas transport now become relevant for the control system. The multivariable controller proposed consists thus of two separate internal model SISO control (IMC) loops developed with a simplified model of the plant and connected by a decoupling term. The IMC structure has the advantage that can compensate for the time delays in the control loop. Since the controller has to work well in the entire range of operating points, a scheduling of its parameters is necessary. The parameters of the controller are thus generated automatically starting from the engine model in order to reduce the efforts of calibrating the control system in the entire operating range of the engine.

The validity and feasibility of the proposed control structure is demonstrated experimentally. A test-bench comparison between the emissions-controlled and the standard engine shows that, with this new control structure, the tracking performance and the driveability of the engine during a driving cycle are at least as good as those of the standard engine. The benefits of the novel approach are several; the two most important are the following: 1) The engine can operate in a small range of uncertainty for the $\mathrm{NO_x}$ and PM emissions even in the case of relaxed manufacturing tolerances and ageing of the injectors and of the EGR valve, and 2) the fuel consumption of the engine can be reduced substantially, if the setpoints for the emissions controller are determined by following an adequate control strategy based on the maximization (within the legislated limits) of the $\mathrm{NO_x}$ emissions.

Riassunto

Le norme riguardanti le emissioni dei veicoli a motore stanno diventando sempre più severe, specialmente quelle per le emissioni di $\mathrm{NO_x}$ e di particelle fini (PM) dei motori diesel. In questa tesi viene quindi proposto un sistema innovativo per il controllo delle emissioni inquinanti dei motori diesel usati nelle autovetture moderne. Con questo nuovo approccio si estende il controllo classico delle emissioni, che si basa principalmente sul pilotaggio del percorso dell'aria e del carburante, con un vero sistema di regolazione per le emissioni. Per dimostrare la fattibilità di tale approccio è stato sviluppato un regolatore multi variabile per le emissioni di $\mathrm{NO_x}$ e per il rapporto di miscela (AFR) nello scarico. Il segnale di una sonda lambda è usato come indicatore per le particelle, poiché sul mercato non sono ancora disponibili sensori compatti e a basso costo per misurare la concentrazione di PM. Le entrate per il regolatore sono il segnale di comando della valvola per il ricircolo dei gas di scarico (EGR) e il segnale che determina l'angolo di iniezione del carburante. Infatti, oltre alla pressione di sovralimentazione, che è controllata indipendentemente dalla centralina originale del motore, questi sono i due parametri che influenzano maggiormente la formazione di emissioni di $\mathrm{NO_x}$ e PM. Inoltre, con questa scelta dei parametri, ne risulta un sistema 2×2 con una struttura triangolare conveniente per lo sviluppo di un regolatore.

Siccome i nuovi sensori adottati sono sensibili alla variazione di pressione, essi devono essere montati nella parte a bassa pressione dello scarico, quindi dopo la turbina. Ovviamente, i tempi morti dovuti al trasporto dei gas di scarico fino ai sensori diventano rilevanti per il sistema che deve essere controllato. Il regolatore multi variabile proposto consiste quindi in due circuiti indipendenti, basati su una struttura IMC (Internal Model

Control) che è in grado di compensare i tempi morti. Questi due circuiti sono sviluppati partendo da un modello semplificato del percorso da regolare e sono connessi tramite un elemento che disaccoppia i due canali. Considerando che il regolatore deve essere in grado di funzionare adeguatamente in tutto il campo di operazione del motore, è necessaria una parametrizzazione. Vista la complessità del sistema, per ridurre il tempo necessario alla calibrazione del regolatore in ogni punto del campo di operazione, i parametri sono generati automaticamente partendo dal modello matematico del motore.

La validità e la fattibilità del sistema di controllo proposto sono dimostrate sperimentalmente sul banco di prova. Un confronto tra il motore dotato di sistema di regolazione delle emissioni e quello convenzionale mostra che la capacità di seguire un profilo di emissioni e la guidabilità del motore con il nuovo sistema di controllo sono almeno buone quanto quelle del motore convenzionale. I benefici di questo approccio innovativo sono diversi, i più importanti sono i seguenti: 1) il motore può operare in un'area di incertezza più ristretta per quanto riguarda le emissioni di NO_x e PM, anche in caso di tolleranze di produzione più rilassate e usura degli iniettori e della valvola EGR, e 2) il consumo di carburante può essere ridotto sostanzialmente, determinando le mappe dei valori desiderati per le emissioni di NO_x e AFR secondo un'adeguata strategia basata sulla massimizzazione (entro i limiti consentiti) delle emissioni di NO_x.

Acknowledgements

This thesis is based on my research performed at the Measurement and Control Laboratory of the Swiss Federal Institute of Technology (ETH) in Zurich between 2003 and 2008. It was carried out with the support of the Research Association for Combustion Engines (FVV), Frankfurt, Germany, and by the Swiss Federal Office for the Environment (BAFU), Bern, Switzerland.

I wish to thank my advisor, Prof. Dr. Lino Guzzella, for proposing the project and for providing support throughout the course of this work. Thanks are also due to Dr. Chris Onder for his most valuable support.

Furthermore, I would like to thank Prof. Dr. Hans Peter Geering for accepting to be my co-examiner.

A special thanks goes to Dr. Alois Amstutz for his valuable support for technical problems, and also for motivating me when I occasionally lost the direct way to reach the goal of the project. I appreciated very much to work with him during this period of time.

I would also like to thank the industrial research group for the initiation of the project, proposed by Dr. Rainer Buck of Robert Bosch GmbH, first lead by Dr. Klaus Allmendinger, and then by Zandra Jansson of Daimler AG. It gave interesting inputs to the project bringing the interests of the industry partners.

I immensely appreciated the fellowship and the support of the entire staff of the Measurement and Control Laboratory. In particular, I would mention my past and present colleagues, among them Alexander Schilling, Yves Hohl, and Michael Benz, with whom I shared the office, Mikael Bianchi, Marzio Locatelli, Raphaël Suard, and Charlie Boston.

I would like to thank the technical staff, Oskar Brachs, Jan Prikyl, and of course Hansueli Honegger, who has always been disposable for patching hardware problems and who contributed to create a funny atmosphere in the catacombs of the laboratory. Special thanks go to Brigitte Rohrbach for carefully reviewing all the earlier publications written in English and in German.

As they played an important role, I cannot forget to thank Manuel Urstöger, Simon Tanaka, and Roman Felix, the diploma and term-paper students, who helped me by the realization of some parts of this thesis.

This thesis could not have been accomplished without the support of my family, that gave me the opportunity to study at ETH, and of my girlfriend Arianna Arrigoni, who supported me during the entire thesis.

Contents

Abstract i

Riassunto iii

Acknowledgements v

Nomenclature xi

1 Introduction 1
- 1.1 Pollutant Emissions of Diesel Engines 2
  - 1.1.1 Nitrogen Oxides 2
  - 1.1.2 Particulate Matter 3
  - 1.1.3 Emissions Legislation 3
- 1.2 State of the Art 3
- 1.3 Actual Research Topics 5
- 1.4 Feedback Control of the Emissions 5
- 1.5 Structure of the Thesis 8

2 Test Bench 9
- 2.1 Bypass and Measurement Setup 10
- 2.2 Dynamics of Sensors and Actuators 11
  - 2.2.1 EGR Valve 12
  - 2.2.2 Air/Fuel-Ratio Sensor 13
  - 2.2.3 NO_x Sensor 14
- 2.3 Exhaust Gas Measurement Devices 16
  - 2.3.1 Cambustion fNOx400: NO and NO_x 16

2.3.2 AVL Micro Soot Sensor: PM 17
2.3.3 Horiba MEXA 1300 FRI: CO and CO_2 17

3 Preliminary Study 19
3.1 Choice of the Control Signals 19
3.2 Empirical Engine Model 20
3.2.1 Analysis of the Static Gains 20
3.2.2 Frequency Response Measurements 23
3.3 Plant Model 26
3.3.1 Plant Approximation 26
3.3.2 Diagonalization of the Plant 27
3.4 Solution to the Control Problem 28

4 Nonlinear Engine Model 31
4.1 Mass Flow Through Orifices 33
4.1.1 Throttle 34
4.1.2 EGR Valve 35
4.1.3 Turbine with Variable Geometry 37
4.2 Air/Fuel Ratio 38
4.2.1 Residual Gas 38
4.2.2 Gas Mixing Dynamics 39
4.2.3 Fresh Air Fraction 40
4.3 Receivers 41
4.3.1 Intake Manifold 42
4.3.2 Exhaust Manifold 42
4.4 Heat Exchange Processes 43
4.4.1 EGR Cooler 43
4.4.2 Heat Exchange in the Exhaust Manifold 45
4.5 Engine Processes 49
4.5.1 Volumetric Efficiency 50
4.5.2 Torque Generation 51
4.5.3 Temperature of the Exhaust Gases 53
4.6 Modeling Time Delays 54
4.6.1 Delays Due to the Combustion Process 55
4.6.2 Delay in the Intake Manifold 56

4.6.3 Delay in the Exhaust Manifold 56
4.7 NO_x Model 57
4.8 Validation of the Nonlinear Model 58
4.9 Linearization of the Engine Model 59
4.9.1 Theory 60
4.9.2 Realization 61

5 SISO Air/Fuel-Ratio Controller 63
5.1 Analysis of the Plant 64
5.2 Internal Model Controller 66
5.3 H_∞-Method 67
5.3.1 Automatic Design of the Controller 69
5.3.2 Parametrization of the Controller 71
5.4 Comparison of the Feedback Controllers 72
5.5 Static Feedforward Controllers 73
5.5.1 Nonlinear Feedforward Controller 73
5.5.2 Disturbance Compensator 76
5.5.3 Simulation with the Feedforward Controllers 76
5.6 Experimental Results 77

6 MIMO Emissions Controller 81
6.1 Analysis of the Plant 83
6.2 Robustness Analysis 85
6.3 Experimental Results 86
6.3.1 Step Between Two Operating Points 87
6.3.2 Setpoint Tracking during a Driving Cycle 90
6.3.3 Range of Uncertainty and Sensor Drifts 92

7 Setpoints Optimization 95
7.1 Control Strategy 95
7.2 Formulation of the Problem 96
7.2.1 Fuel Consumption Model 97
7.2.2 Calculation of the Overall NO_x Mass 98
7.3 Solution to the Problem 100
7.3.1 Analysis of the Driving Cycle 100

7.3.2 Optimization with Constraints 103
7.3.3 Results of the Optimization 104
7.4 Empirical Model for the PM 105
7.5 Experimental Results 106

8 Summary and Conclusions 107

References 115

Curriculum Vitae 117

Nomenclature

Abbreviations

AFR	Air/fuel ratio
BMEP	Brake mean effective pressure
CA	Crank Angle
ECU	Electronic control unit
EGR	Exhaust gas recirculation
HFM	Hot-film air-mass meter
IMC	Internal model controller
LPV	Linear parameter varying
MIMO	Multiple input multiple output
PM	Particulate matter
QSS	Quasi static simulation
SI	Spark ignited
SISO	Single input single output
SOI	Start of injection
VGT	Variable geometry turbine

Subscripts

$_a$	air
$_e$	engine
$_f$	fuel
$_{amb}$	ambient
$_{ax}$	axial
$_{cd}$	conduction
$_{cr}$	critical

cv	convection
cyl	cylinder
c	compression
d	displacement
egr	exhaust gas recirculation
eg	exhaust gas
em	exhaust manifold
fc	fresh charge
ic	intercooler
im	intake manifold
in	input / inside
nom	nominal
opt	optimal
out	output / outside
rad	radiation
ra	radial
ref	reference
rg	residual gas
sec	section
sh	shell
s	stroke
th	throttle
w	wall

Symbols

$\dot{m}$	Mass flow	$^{\mathrm{kg}}/_{\mathrm{s}}$
$\dot{Q}$	Heat flux	W
$\dot{V}$	Volume flow	$^{\mathrm{m}^3}/_{\mathrm{s}}$
A	Area	m^2
c_p, c_v	Specific heat at constant pressure / volume	$^{\mathrm{J}}/_{\mathrm{kg\ K}}$
D	Distance	m
d	Diameter	m
Gr	Grashof number	-
H	Specific enthalpy	$^{\mathrm{J}}/_{\mathrm{kg}}$

h	Heat transfer coefficient	$\mathrm{W}/\mathrm{m}^2\,\mathrm{K}$
k	Thermal conductivity	$\mathrm{W}/\mathrm{m\,K}$
L	Length	m
M	Torque	Nm
N	Rotational speed	$1/\mathrm{min}$
Nu	Nusselt number	-
p	Pressure	Pa
Pr	Prandtl number	-
Q	Heat	J
R	Specific gas constant	$\mathrm{J}/\mathrm{kg\,K}$
r	Heat transfer resistance	$\mathrm{m}^2\,\mathrm{K}/\mathrm{W}$
Ra	Rayleigh number	-
Re	Reynolds number	-
s	Laplace variable	-
T	Temperature	K
u	Control signal / input	-
V	Volume	m^3
v	Velocity	m/s
x_{egr}	EGR rate	-
y	Measured signal / output	-
α	Thermal diffusivity	m^2/s
δ	Time delay	s
ϵ_c	Compression ratio	-
η_{vol}	Engine volumetric efficiency	-
γ	Fresh air fraction	-
κ	Specific heats ratio	-
λ	Relative air/fuel ratio	-
μ	Dynamic viscosity	$\mathrm{kg}/\mathrm{m\,s}$
ν	Kinematic viscosity	m^2/s
Ψ	Flow function	-
ρ	Density	kg/m^3
σ_0	Stoichiometric air/fuel ratio	-
τ	Time constant	s
ε_{egr}	Efficiency of the EGR cooler	-

Chapter 1

Introduction

Diesel engines are more efficient than gasoline engines of the same power, especially when operating in partial load. This results in lower fuel consumption and thus in lower carbon dioxide emissions. In the context of global warming due to greenhouse gases like CO_2, those emissions caused by private transport attracted a great deal of attention in the media, and thus, reducing those emissions has become a very important issue. While diesel engines have been widely used in applications that require their reliability and high torque output for a long time such as trucks, heavy equipment, and busses, their use in passenger cars in Europe has experienced a boom in the last decade, and the market share is still growing.

This is mainly due to the technical advances regarding diesel technology in the nineties. New fuel-injection systems connected to a common rail, the feedback-controlled exhaust gas recirculation (EGR), and the turbocharger with variable geometry turbine (VGT) have decisively closed the gap towards gasoline engines by improving the fuel consumption, the driveability, and the pollutant emissions of modern diesel engines. Modern electronic control units (ECU) with increasing capabilities and functionalities have been also a precondition for this growth. Nowadays, it is possible to read and evaluate a multiplicity of sensors, to simulate models, and to control the available actuators in real-time in order to guarantee optimal engine operating conditions.

Although the new technologies like the EGR, the VTG, and exhaust aftertreatment systems helped to reduce the NO_x and particulate matter

(PM) emissions considerably, further measures are to be taken in order to meet the increasingly restrictive emission standards.

This thesis proposes thus a novel approach that has the goal to control NO_x and particulate matter (PM) emissions in closed loop, with the adoption and evaluation of new on-board exhaust gas sensors.

In this chapter the topics necessary for understanding the problematic are introduced and the objectives of this thesis are exposed.

1.1 Pollutant Emissions of Diesel Engines

The raw emissions of diesel engines are lower than those of comparable gasoline engines. The NO_x emissions, for instance, are 70% lower, and the CO emissions are 90% lower. But, due to an excess of oxygen in the exhaust pipe, a conventional three-way catalytic converter could not be adopted in diesel engines to further reduce the emissions as in SI engines.

The main factors affecting the formation of the NO_x and PM emissions in the combustion process of a diesel engine are illustrated in the following paragraphs. However, a detailed phenomenological description of the emissions formation is not necessary for the scope of this work. Only the understanding of the qualitative relation between engine parameters and emissions formation is required for proposing an effective control structure and strategy for regulating the NO_x and PM emissions.

1.1.1 Nitrogen Oxides

The parameters that most significantly affect the formation of NO_x in diesel engines are the in-cylinder gas temperature, the availability of oxygen, the cylinder pressure, as well as the residence time of the fuel/gas mixture in locations with favorable temperatures and oxygen concentration for the formation of nitric oxides [31]. These parameters depend on the charge pressure, on the EGR rate, and on an earlier or a later start of injection (SOI).

1.1.2 Particulate Matter

The generation of PM is an actual topic for many researchers. The PM consists mainly of soot, while the remainder is called soluble organic fraction. The production process of soot consists of two principal events, namely the soot formation and oxidation. These processes run in parallel in the cylinder.

Soot mainly originates from the incomplete combustion of the fuel. Roughly speaking, soot is generated between 1600 and 1800 K, and between 50 and 100 bar, especially at low air/fuel ratio (AFR) values. Even if the engine runs in lean conditions overall, locally, there are always regions around the injected fuel spray where the mixture has an AFR of ≤ 1. A more detailed description of the soot processes can be found in [61], for instance.

Even in the absence of simple correlations that can predict the overall PM production quantitatively, it can be stated that the in-cylinder gas temperature and the availability of oxygen are the main factors influencing the formation of PM.

1.1.3 Emissions Legislation

Legislation concerning the pollutant emissions of diesel passenger cars is becoming increasingly restrictive, especially for $\mathrm{NO_x}$ and PM. Figure 1.1 shows the evolution of the European emissions legislation from their introduction in 1992 (Euro 1) until nowadays (Euro 5). During these 17 years, the limit for $\mathrm{NO_x}$ has been reduced by 82% and that for PM by 97%.

1.2 State of the Art

Modern diesel engines are complex systems that burn a carefully controlled mixture of fresh air, burnt gases, and fuel in order to produce the desired mechanical work at the lowest possible fuel consumption and pollutant emissions. The mixture entering the cylinder is controlled very precisely by sophisticated control loops, like the fuel injection, the EGR

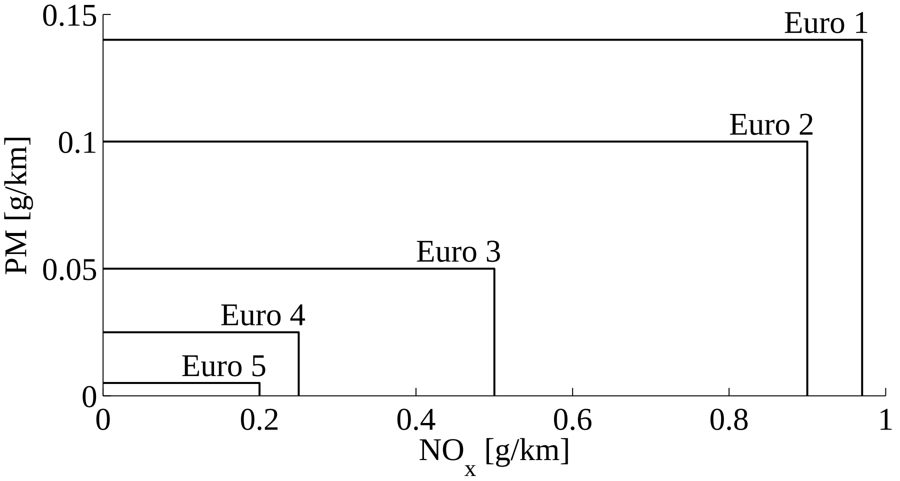

Figure 1.1: Evolution of the European emissions legislation.

path, the turbocharger with VGT, etc. The setpoints for these loops are determined by the manufacturers by an accurate calibration of the engines such that the best possible tradeoff between the conflicting requirements is achieved and such that these calibrations work well for all engines in spite of manufacturing tolerances and for the complete time span required by the legislation (Fig. 1.2).

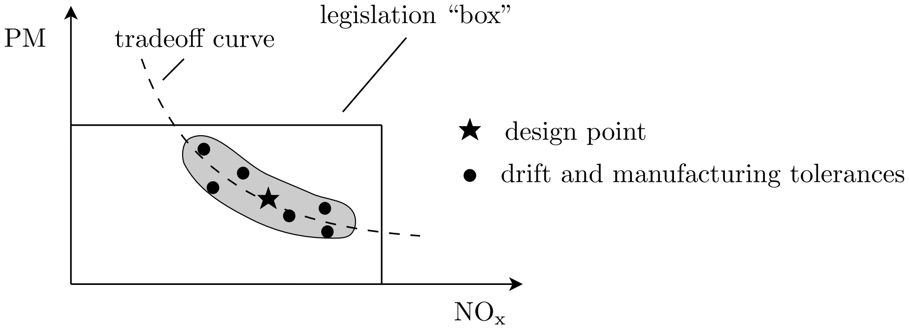

Figure 1.2: State of the art for tuning the engine emissions and typical NO$_x$-PM tradeoff curve in diesel engines.

The state of the art for controlling (indirectly) the EGR flow is to use the air mass flow $\dot{m}_a$ entering the engine as the controller input. Figure 1.3 shows a conventional EGR control loop, where λ is the AFR normalized by stoichiometry, u_{egr} the EGR-valve control signal, $\dot{m}_f$ the injected fuel quantity, and HFM the hot-film air-mass meter. While conventional controllers of the EGR system offer fast reactions, they rely on data measured *before* combustion takes place. The conventional control structure is therefore basically a feedforward controller for the AFR.

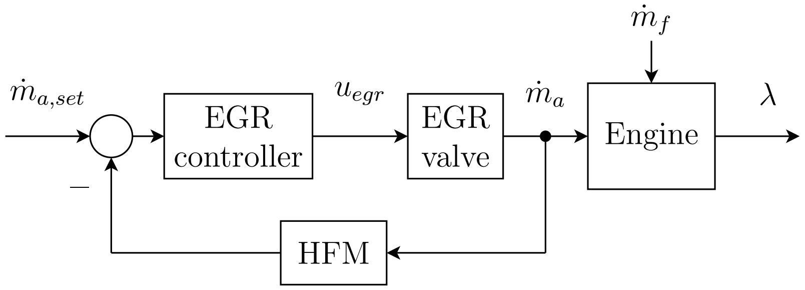

Figure 1.3: Conventional EGR control loop.

Moreover, exhaust gas aftertreatment systems are adopted in standard production engines, that can deal with the $\mathrm{NO_x}$ and PM emissions of diesel engines. An overview of the actual technology is given in [35], for instance.

1.3 Actual Research Topics

Some contributions in the literature can be found about emissions reduction techniques. However, much of the ongoing research is essentially based on the control of the EGR valve and of the VGT actuator. Since both EGR and turbine flows are driven by the exhaust gas, there is clearly a strong coupling between the two flows. Model based control systems that coordinate the EGR and VGT actuators for emissions reduction especially during fast transient operations are investigated in [33,42,47,48,59,62,63,67], for instance.

While further improvements along these lines are still possible, for instance with higher injection pressures, more flexible injection systems, and an improved and coordinated control of the EGR valve and of the VGT, it is clear that a radically new approach is needed to achieve substantial progress without increasing significantly the system costs.

1.4 Feedback Control of the Emissions

The idea of controlling the emissions in a closed-loop structure is based on the results of some researchers who already investigated the adoption of after-combustion measurement devices for designing closed-loop control systems. For instance, more than ten years ago the authors of [6] suggested that the relative AFR signal could be used to control the EGR flow in diesel passenger cars (Fig. 1.4). It was the first time the diesel "emissions" were controlled in a closed loop.

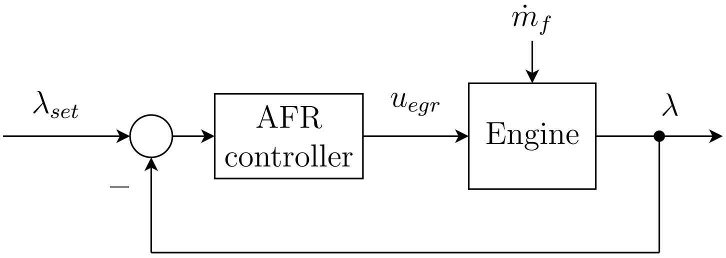

Figure 1.4: Air/fuel-ratio control loop

The advantages are clear: manufacturing tolerances, aging and drift of several engine components can be compensated by the adoption of only one exhaust gas sensor combined with such a control structure.

As a first step towards fully emissions-controlled diesel engines and to prove the feasibility of this new approach, this work proposes to measure the NO_x concentration in and the AFR of the exhaust gases on-board, and to use this information to control the engine system. The AFR is considered to be a proxy for the PM emissions and, due to the fact that compact and low-cost PM sensors are not yet commercially available [30], a wide-range AFR sensor is used to generate a representative signal for the PM concentration (see Fig. 1.5), while the NO_x concentration is measured with a thick-film ZrO_2 sensor [38].

A true emission-feedback engine control system, which includes the option of performing powerful engine monitoring functions (as described in [55], for instance), has several advantages: 1) It permits the engine to be operated in a smaller range of uncertainty from a defined design point; 2) with an adequate control strategy (as described further below) lower fuel consumption levels can be achieved while still respecting the emission limits; 3) it can handle larger manufacturing tolerances, e.g. for the injectors, by compensation of deviations and on-line calibration and, thus, substantially reduce the system costs; and 4) it allows changing conditions such as environmental changes and engine ageing to be monitored. Since

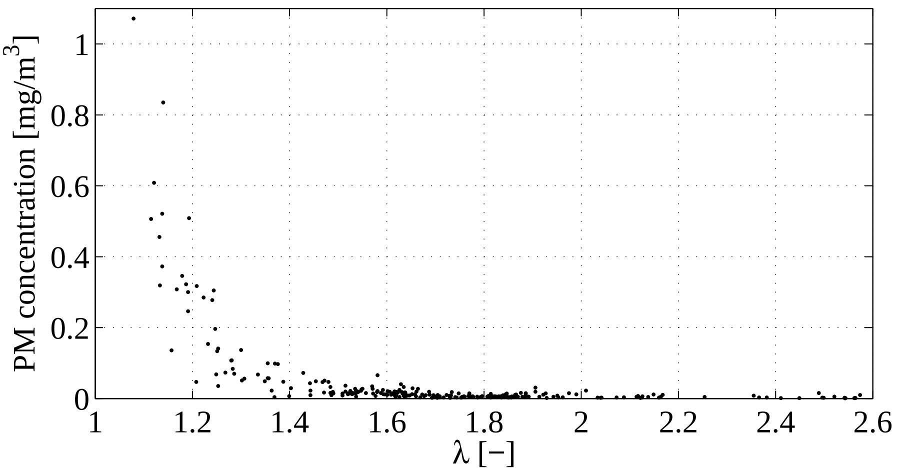

Figure 1.5: Correlation between AFR and PM concentration for a typical diesel engine in various operating points.

this thesis is just a first step toward designing a fully emissions-controlled engine, the optional engine monitoring tools and thus the points 3) and 4) are not included in the investigations, but could be topics for future work.

Of course, all these advantages come at the price of a more difficult control problem. In fact, measuring relevant information after the engine increases the delays present in the control loops and, thus, reduces the bandwidths achievable with conventional control structures. Moreover, multivariable cross-couplings become more important such that they must be included in the system design.

In order to be applied on a standard-production ECU, the new emissions control system has to meet the following requirements: 1) The control quality, namely the tracking performance during a driving cycle (especially of the AFR), and the driveability have to be at least as good as those attained by using the conventionally controlled engine; 2) the application has to be simple to avoid any fine-tuning of the controller on the test bench, and considering that the memory and the computing power of an ECU are limited; and 3) a high level of automation in the entire design process of the controller has to be achieved, from the calibration of the engine model to the design and parametrization of the controller. In this way, besides reducing the efforts to calibrate the control system, the results obtained in this work can be easily transferred to other engines.

The multivariable emissions controller proposed adopts a new control strategy based on the maximization (within the legislated limits, of course) of the $\mathrm{NO_x}$ mass produced during a defined driving cycle. Actually, with the constraint defined by the maximal amount of $\mathrm{NO_x}$, the AFR and $\mathrm{NO_x}$ setpoints for the emissions controller can be optimized such that the fuel consumption is reduced. Moreover, due to the monotonically decreasing $\mathrm{NO_x}$-PM tradeoff curve, the PM production is automatically minimized as well.

This work proposes thus to extend the classical approach, which is essentially a feedforward only, with a true feedback structure for the emissions. It is important to mention that the main objective of this thesis is to prove the validity and the feasibility of such an approach and not to improve on existing control systems.

1.5 Structure of the Thesis

This thesis is structured as follows: Chap. 2 describes the data acquisition setup of the test bench, as well as the elements used in the feedback loop and the measurement devices necessary for calibrating the mathematical model of the plant. In Chap. 3 a preliminary study is introduced that investigates the characteristics of the control system, suggests simplifications of the plant, and proposes a scheme for the solution of the control problem. A nonlinear physics-based engine model is designed and linearized in a grid of relevant operating points as described in Chap. 4. Since the multivariable plant to be controlled has a convenient triangular structure, a SISO feedback controller for the air/fuel ratio is investigated in Chap. 5, first, and then the results obtained are extended to the MIMO emissions controller in Chap. 6. A control strategy based on the optimization of the setpoints for the emissions controller is proposed in Chap. 7 with the goal to minimize the fuel consumption. Chap. 8 is dedicated to the conclusions.

Chapter 2

Test Bench

All the experiments conducted in this work are carried out on a fast (15 Hz bandwidth) dynamic engine test bench (see Fig. 2.1).

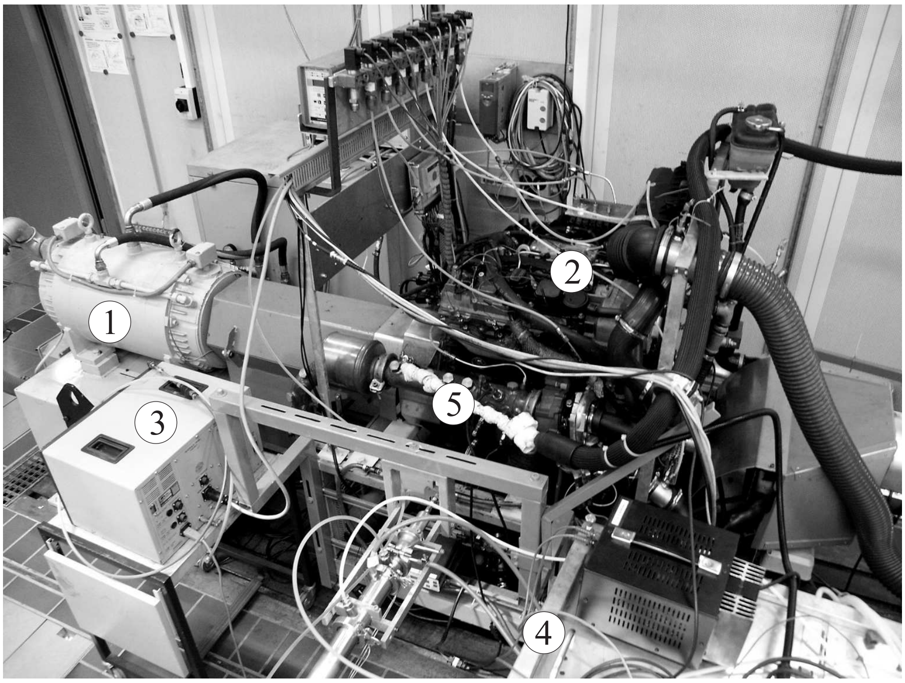

Figure 2.1: Picture of the testbench engine: 1) brake, 2) engine, 3) PM measurement for validation, 4) fast NO_x measurement device for validation, 5) solid-state NO_x and AFR sensors used in the feedback loop.

The testbench engine is a Daimler-Chrysler OM611, a 2.2 liter diesel engine with 4 cylinders, common-rail injection system, cooled EGR, and VGT turbocharger. The data of the engine is resumed in Tab. 2.1.

Cylinders	4
Valves per cylinder	4
Displaced volume [cm^3]	2151
Bore [mm]	88
Stroke [mm]	88.4
Compression ratio [-]	19
Nominal power [kW] / [rpm]	92 / 4200
Maximum torque [Nm] / [rpm]	300 / 1800-2600

Table 2.1: Technical data of the test-bench engine.

2.1 Bypass and Measurement Setup

The test-bench engine is equipped with a hardware module (ETAS, ETK7) for the communication with the standard ECU (Bosch, EDC 15), as shown in the sketch depicted in Fig. 2.2. With this module and an adequate software (ETAS, INCA) it is possible to read the actual values of every variable calculated and measured by the ECU, and modify every map and parameter contained into the code of the ECU. With a real-time processor board and its software (ETAS, ASCET) it is possible to deploy new control structures and to bypass some variables calculated or measured by the ECU. These software and hardware modules are all connected with a central unit (ETAS, ES1000).

The acquisition of other quantities that are not measured by the ECU is carried out with extra sensors mounted on the engine (Fig. 2.3). The acquisition system (dSpace) consists of a real-time processor board with additional input and output capability that can be programmed via Matlab/Simulink. The information collected by the sensors is converted into digital signals and acquired by the dSpace system via CAN-bus. The sampling time is limited by the CAN coupler (WAGO) to 2 ms.

Since the AFR and NO_x sensors are sensitive to the pressure, in order to guarantee the best measurement accuracy they must be installed in the low-pressure tract of the exhaust manifold, i.e. downstream of the turbine.

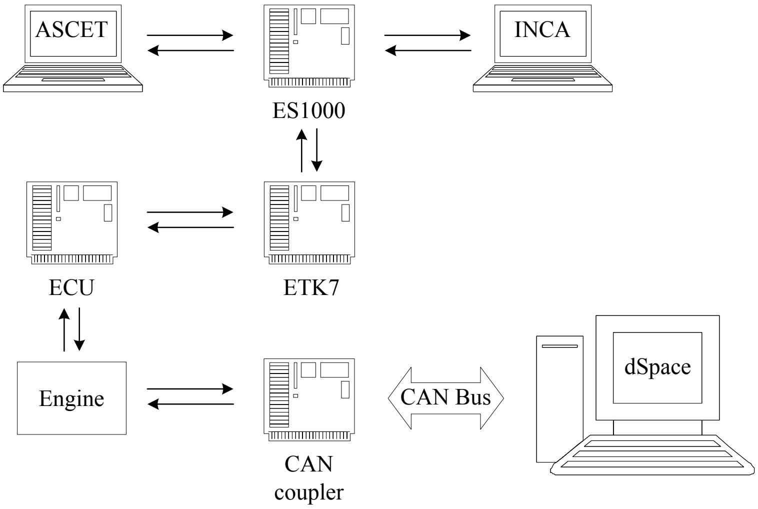
ASCET
ES1000
INCA
ECU
ETK7
Engine
CAN coupler
CAN Bus
dSpace

Figure 2.2: Sketch of the testbench setup.

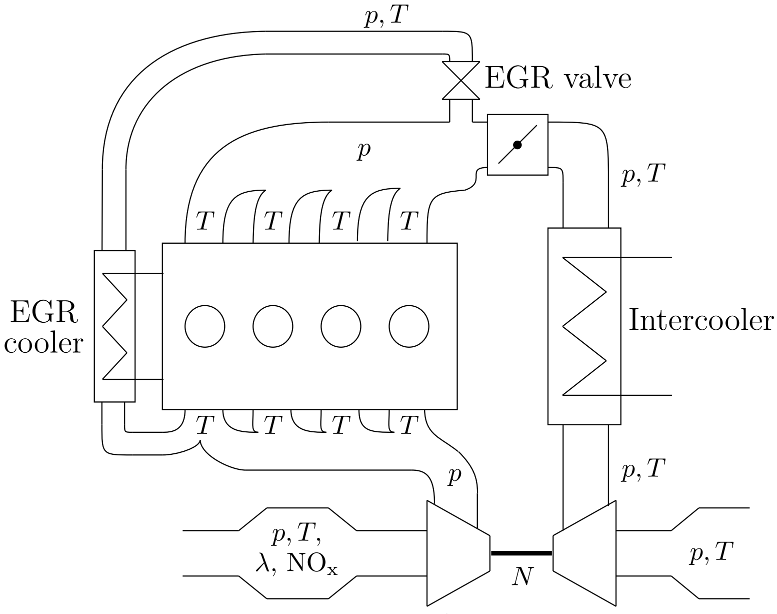
p, T
EGR valve
p
p, T
T
T
T
T
EGR cooler
Intercooler
T
T
T
T
p
p, T
p, T, λ, NOx
N
p, T
Turbine
Compressor

Figure 2.3: Sketch of the test-bench engine with the extra test points.

2.2 Dynamics of Sensors and Actuators

In order to support the new emissions control system, the test-bench engine has been modified. Therefore, a new electrical EGR valve with integrated position measurement, a wide-range AFR sensor, and a NO_x sensor have been installed.

Since it is very important to know the exact dynamical behavior of every component involved in the control loop for proposing an effective model-based controller, these elements are analyzed in detail in the next paragraphs.

2.2.1 EGR Valve

The pneumatic EGR valve, with which the engine was originally equipped, showed big nonlinearities between the command signal and the opening area that are difficult to model exactly [45]. In order to design an accurate engine model on which the entire control synthesis process is based, this valve has been substituted by an electrical one (Pierburg) with the possibility to measure its opening position. In this way, the instantaneous effective area of the EGR valve can be identified and determined unequivocally as a function of the measured opening position of the valve.

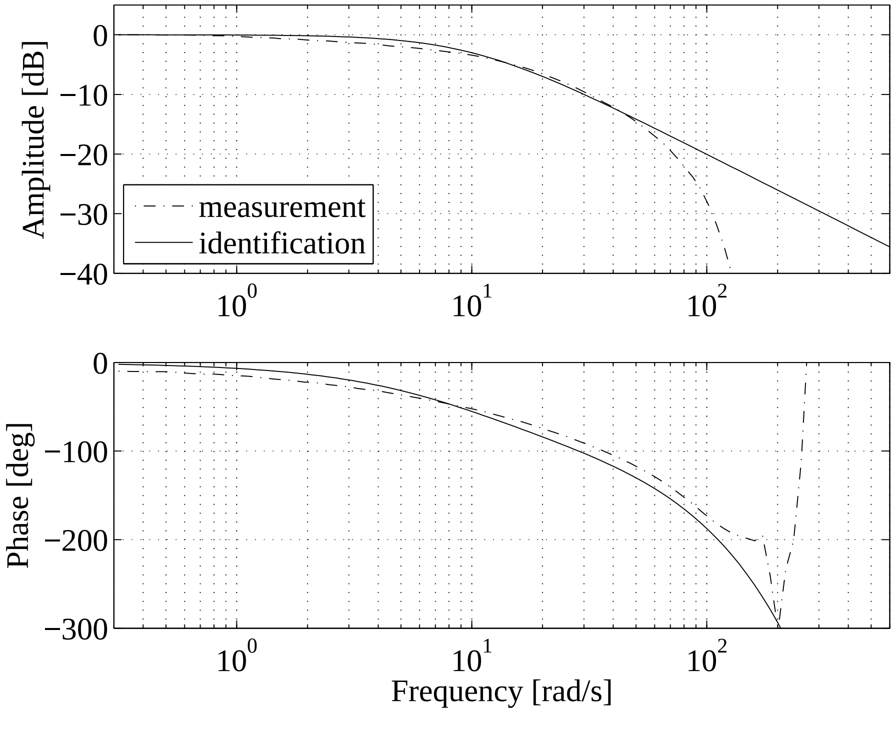

Figure 2.4: Bode diagram of the EGR valve actuator model.

The new EGR valve is driven by an electro-magnetic actuator, whose dynamics have been determined by means of frequency-response measurements. The transfer function between the command signal of the valve u_{egr} and its position y_{egr} is measured and approximated by a first-order low-pass filter, as in Eq. 2.1. A graphical comparison between the measured and the identified transfer function is depicted in Fig. 2.4.

$$G_{egr}(s) = \frac{1}{0.130 \cdot s + 1} \cdot e^{-0.020 \cdot s} \tag{2.1}$$

2.2.2 Air/Fuel-Ratio Sensor

The dynamics of the wide-range AFR sensor (Bosch LSU 4.9) are comparable to those of the first-order low-pass filter described by Eq. 2.2 and depicted in Fig. 2.5.

$$G_{\lambda}(s) = \frac{1}{0.05 \cdot s + 1} \cdot e^{-0.010 \cdot s} \tag{2.2}$$

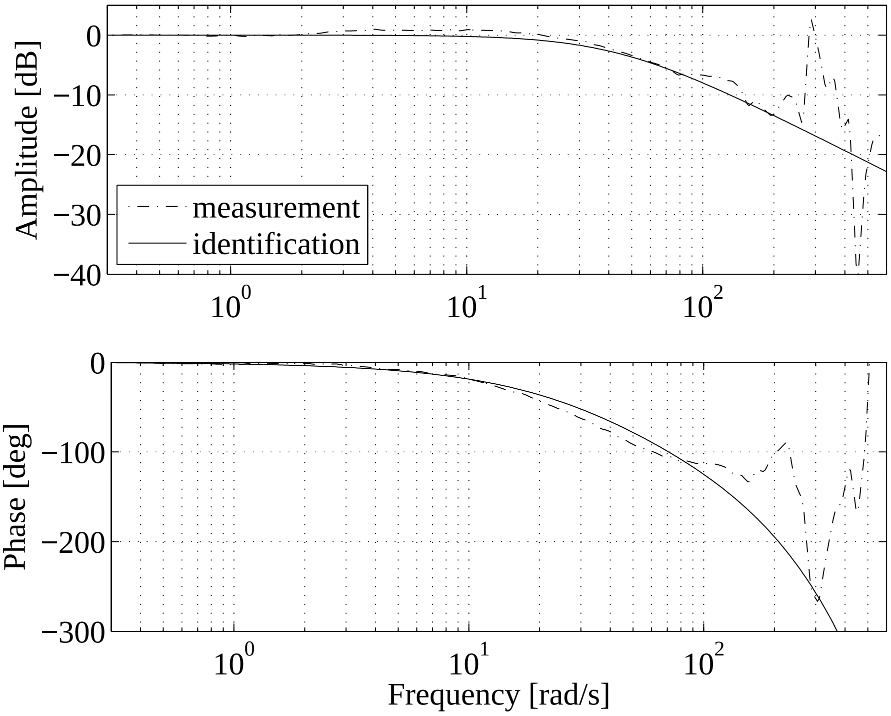

Figure 2.5: Bode diagram of the AFR sensor model.

2.2.3 NO_x Sensor

Usually, the measurement of the NO_x concentration in the exhaust gas is carried out with a chemiluminescence detector (CLD). Such a device is expensive and too large to fit in a car. Therefore, a smaller and cheaper device is used instead for the on-board measurement of the NO_x concentration (Siemens-VDO, measuring range between 0 and 1500 ppm). The sensing element consists of a multi-layered thick film Zirconia ceramic $Zr0_2$, and its working principle [36–38] is briefly explained in the next paragraphs.

Considering the chemical equilibrium

$$NO \rightleftharpoons \frac{1}{2}N_2 + \frac{1}{2}O_2 \, , \tag{2.3}$$

by removing the oxygen by an electromotive force, the chemical reaction moves to the right side of the equation. This means that the amount of NO decomposed is proportional to the amount of oxygen. Because of this principle, the oxygen concentration of the measuring gas has to be treated at a constant level prior the NO_x measurement and, therefore, two internal cavities are formed (Fig. 2.6).

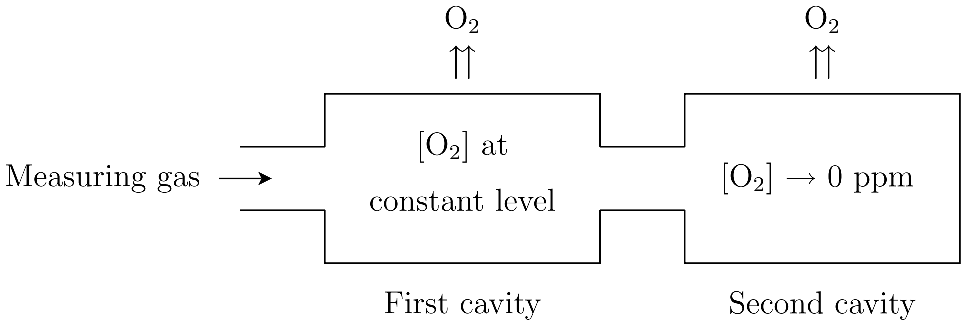

Figure 2.6: Measurement principle of the NO_x sensor.

The measuring concept consists of lowering the oxygen concentration of the measuring gas to a predetermined level in the first internal cavity, in which NO does not decompose, and of further lowering the oxygen concentration of the measuring gas to a predetermined level in the second internal cavity, in which NO decomposes. The oxygen generated due to the NO decomposition is detected by a measuring electrode as the sensor signal.

Furthermore, in order to minimize the dependency of the sensor performance on the temperature variations of the exhaust gases, a temperature control is applied to the sensor.

Since the average response time of this device is slow if compared to the transient operations of the engine during a driving cycle, it is necessary to identify a dynamical model that describes reliably the behavior of the $\mathrm{NO_x}$ sensor for a precise feedback control of these emissions.

The sensor dynamics can be approximated by a first-order low-pass filter with the time constant τ_{NOx} and the time delay $T_{d,NOx}$, as in Eq. 2.4.

$$G_{NOx}(s) = \frac{1}{\tau_{NOx}s + 1} \cdot e^{-sT_{d,NOx}} \tag{2.4}$$

Experiments have shown that the response time of the sensor varies as a function of the engine's operating conditions, and thus, a model with fixed parameters would not be enough accurate for describing its behavior. The two model parameters depend on the mass flow and on the temperature and pressure of the exhaust gas. Choosing the volume flow of the exhaust gas $\dot{V}_{eg}$ as the independent variable and assuming ideal gas properties, all the effects mentioned above are implicitly considered. Therefore, the two parameters of the sensor model are identified as a function of $\dot{V}_{eg}$ by comparing the $\mathrm{NO_x}$ concentration signal measured with the reference CLD device and filtered by the model $G_{NOx}(s)$, with the signal measured by the Siemens-VDO sensor.

The internal time delay of the sensor is almost constant and amounts to about 0.3 s, while its time constant varies as a function of $\dot{V}_{eg}$ between 0.9 and 1.5 s. Larger exhaust gas volume flows mean higher flow velocity and thus higher exchange rates in the sensor, which leads to a faster response. The relation that links the exhaust gas volume flow and the sensor time constant can be approximated linearly as in Eq. 2.5.

$$\tau_{NOx} = 1.53 - 8.06 \cdot \dot{V}_{eg} \tag{2.5}$$

A comparison between the model with only one set of fixed parameters and that with variable parameters is depicted in Fig. 2.7.

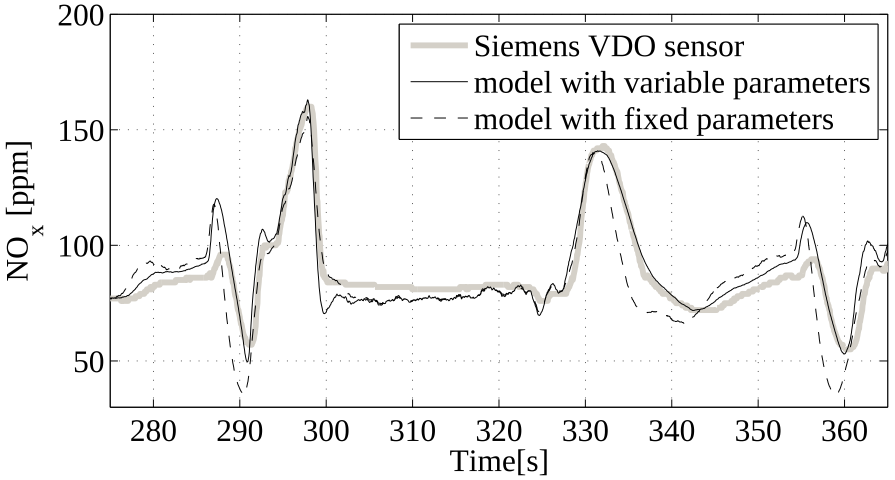

Figure 2.7: Model of the NO$_x$ sensor.

2.3 Exhaust Gas Measurement Devices

The test-bench engine is equipped with fast exhaust gas measurement devices that are used mainly for experimental validations. A dynamical model of these devices is necessary for reconstructing the measured signal at the place where the quantity of interest is effectively generated.

The concentration of NO, NO$_x$, CO and CO$_2$ can be measured with a response time below 100 ms, while the measurement of PM is slower (about 2 s). The measurement devices used during this work are briefly described further below.

2.3.1 Cambustion fNOx400: NO and NO$_x$

The measurement principle of the Cambustion fNOx400 is the chemiluminescence. With this principle, the light emitted from the reaction of NO with ozone is collected and measured by a photo-multiplier.

The compact design of this device, with thin heated sample capillaries and analyzers mounted close to the measurement probe, results in a response time below 10 ms for NO, including the gas transport delay and the internal time constant of the system.

However, the measurement of NO$_x$ requires an additional heater, which adds a transport time of about 50 ms.

2.3.2 AVL Micro Soot Sensor: PM

The measurement of the PM concentration is based on the photoacoustic principle [56]. The diluted exhaust gas is admitted in an optical measuring cell where the soot particles are heated cyclically by a modulated laser beam. Depending on the PM concentration, temperature fluctuations are generated in the cell that produce pressure waves that are detected by a microphone. The amplitude of the pressure wave is proportional to the soot concentration.

The exhaust gas has to be diluted before entering the measuring cell. The dilution system has a time constant of 250 ms and a transport delay of 1.5 s, while the sensing element itself has a time constant of 400 ms.

2.3.3 Horiba MEXA 1300 FRI: CO and CO_2

This device uses the nondispersive infrared analysis method for measuring the CO and CO_2 concentration. This principle exploits the fact that each molecule absorbs infrared rays of a specific wavelength range. Thereby, the absorption intensity is proportional to the concentration of this molecule in the gas.

Mainly due to the dehumidification of the exhaust gas before entering the measurement chamber, the time constant of this device amounts to 30 ms with a transport delay of 70 ms.

Chapter 3

Preliminary Study

In this chapter the plant is investigated that will be used for the design of the emissions controller. This preliminary study has the objective to define the adequate control signals and to provide the necessary information about the plant characteristics, in order to propose an effective scheme for solving the multivariable control problem.

3.1 Choice of the Control Signals

For control purposes, a model with equal numbers of inputs and outputs is preferred, where the outputs are defined as the relative AFR λ and the $\mathrm{NO_x}$ concentration.

Therefore, only two input signals are needed; besides the boost pressure that is regulated independently by the standard controller, the most suitable are the command signal of the EGR valve u_{egr} and the SOI, as depicted in Fig. 3.1.

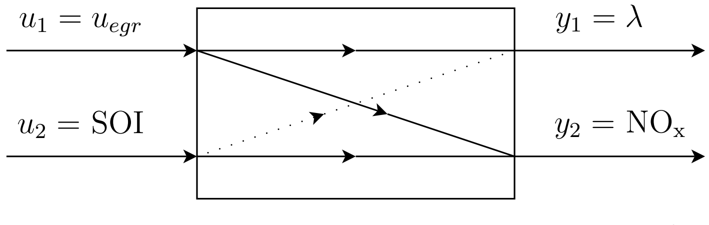

Figure 3.1: Multivariable triangular structure of the system

Actually, as suggested by the analysis of the emissions formation presented in Sec. 1.1, they are the parameters that most significantly and directly affect the formation of the $\mathrm{NO_x}$ and PM emissions. Moreover, this choice leads to a simplified MIMO structure, i.e., a triangular structure with only one cross-coupling between the two channels. In this way the AFR control loop is assumed to be completely independent from the $\mathrm{NO_x}$ loop (the dotted line in Fig. 3.1 indicates that the influence of the SOI on λ is small).

Furthermore, with this choice of control signals the system can be regulated with different bandwidths, namely 1) a larger bandwidth for the control of the AFR path, which is an important indicator for the formation of PM, and 2) a smaller bandwidth for the $\mathrm{NO_x}$ control, principally due to the slow response time of the the $\mathrm{NO_x}$ sensor.

This particular triangular structure has a relative gain array matrix equal to identity, and thus, with the help of a simple decoupler, the plant can be reduced to a diagonal system with two independent SISO loops.

3.2 Empirical Engine Model

In this preliminary study the operating point 2200 rpm and 4 bar brake mean effective pressure (BMEP) is considered as representative for a diesel passenger's car engine, since it is located about in the middle of the engine's operating range. An empirical model of the three relevant paths of the plant (see Fig. 3.1) has been measured in this operating point, by means of a static gain analysis and of frequency response measurements.

3.2.1 Analysis of the Static Gains

The analysis of the static gains of the plant is necessary to establish whether the assumption of a linear model is acceptable and in what range it is applicable.

The measurements consist of slow (quasi-static) variations of the input signals. The results of the static gain analysis are depicted in Figs. 3.2–3.4. The slope of the linear approximation represents the static gain of the path in that operating point.

Figures 3.2 and 3.3 show that the command signal of the EGR valve correlates linearly with the AFR but the NO_x concentration only in a limited range. This fact is mainly due to the nonlinear static behavior of the EGR valve. Figure 3.4 shows that the later the fuel is injected into the cylinder, the flatter the static gain curve of SOI to NO_x becomes.

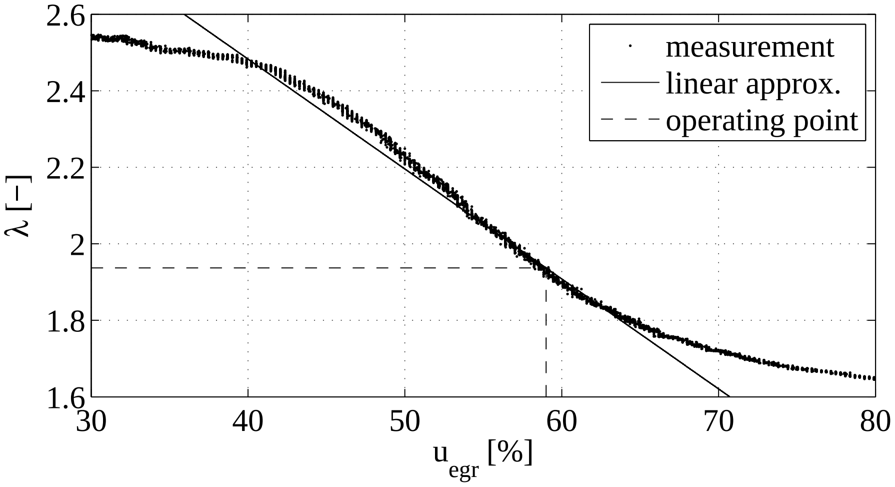

Figure 3.2: Static-gain curve of u_{egr} to λ.

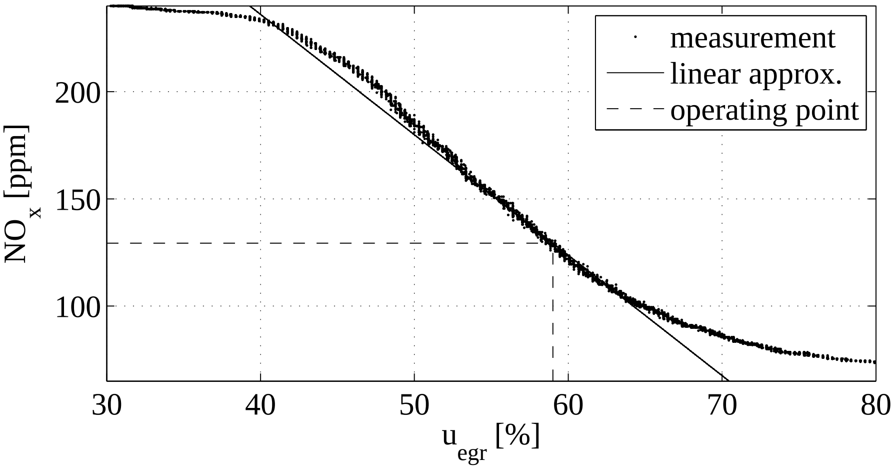

Figure 3.3: Static-gain curve of u_{egr} to NO_x.

As expected and as already mentioned in Sec. 3.1, the slope of the static gain curve of SOI to λ (Fig. 3.5) is relatively small and therefore, the dependency between these two quantities will not be considered in the

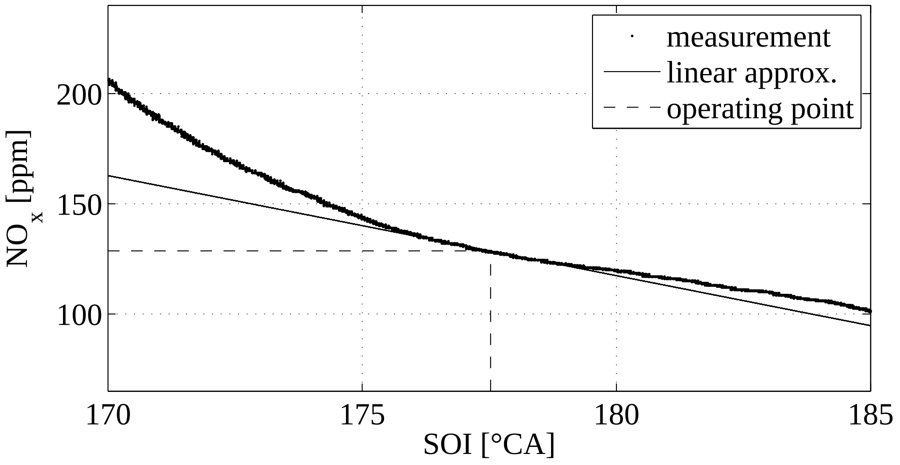

Figure 3.4: Static-gain curve of SOI to NO_x.

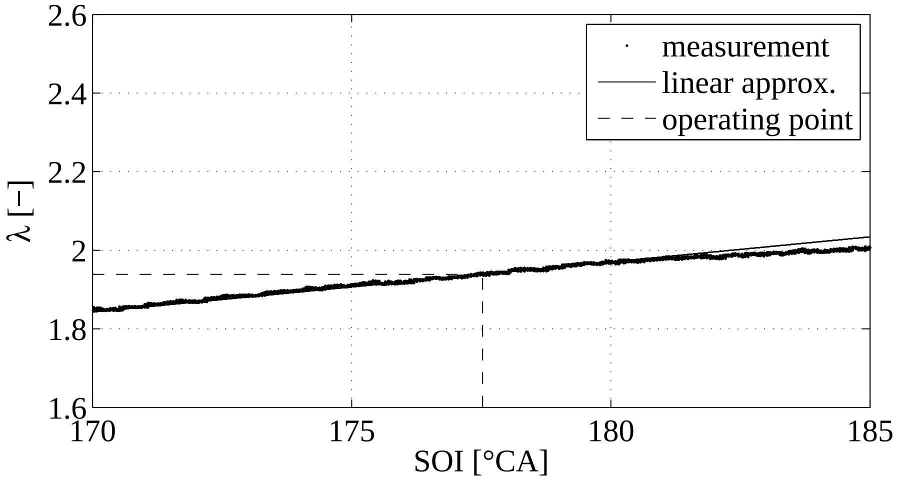

Figure 3.5: Static-gain curve of SOI to λ.

mathematical model of the plant. However this effect is not modeled, a short explanation of how this dependency arises is given.

During the measurements of the static gain curve it has been observed that moving SOI to later, and thus reducing the thermal efficiency of the combustion, leads to a higher exhaust gas temperature. At the same time, the combustion pressure is lower. These facts connect thus a variation of SOI to a change in the AFR. The complete process is explained below, under consideration that during the measurements of the static gain, both the opening position of the EGR valve and the boost pressure are held constant.

According to the ideal gas law applied to the exhaust manifold

$$\dot{m}_{egr} = \frac{p_{em}V}{RT_{em}}, \tag{3.1}$$

where V represents a volume and R is the gas constant, the increase of the exhaust gas temperature T_{em} and the decrease of the pressure p_{em} lead to a reduction of the EGR mass flow $\dot{m}_{egr}$. The temperature in the intake manifold decreases accordingly.

Due to the constant volumetric efficiency of the engine and to the higher density of the gas in the intake manifold, more gas mass $\dot{m}_{im}$ flows through the engine. Therefore, according to

$$\dot{m}_{im} = \dot{m}_a + \dot{m}_{egr}\,, \tag{3.2}$$

the increased amount of fresh air $\dot{m}_a$ entering the cylinders determines an increment of the AFR.

3.2.2 Frequency Response Measurements

The transfer functions of the three relevant paths are measured with a dynamic signal analyzer by exciting the input channels near the operating point in the almost-linear range with sinusoidal signals. The range of the interesting frequencies is discretized in a finite number of points and is scanned. The system response to each frequency is measured, determining thus the amplification and the phase of the system for that frequency.

The results of the measurements of the three paths are depicted in Figs. 3.6–3.8 in the form of Bode diagrams. It can be noticed that the dynamics of each of these paths can be approximated well by low-order elements. In the case of the path from u_{egr} to λ, a first-order low-pass filter with a time delay element is used for representing the dominant dynamics of the system, while the paths from u_{egr} and SOI to $\mathrm{NO_x}$ are better described by a third-order system with a time delay.

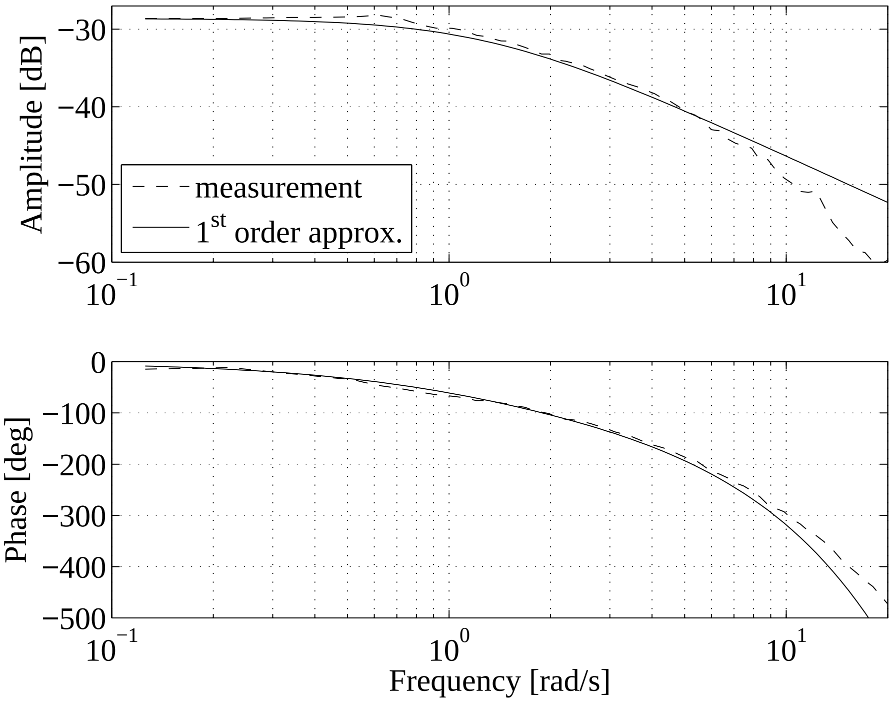

Figure 3.6: Bode plot of the path from u_{egr} to λ.

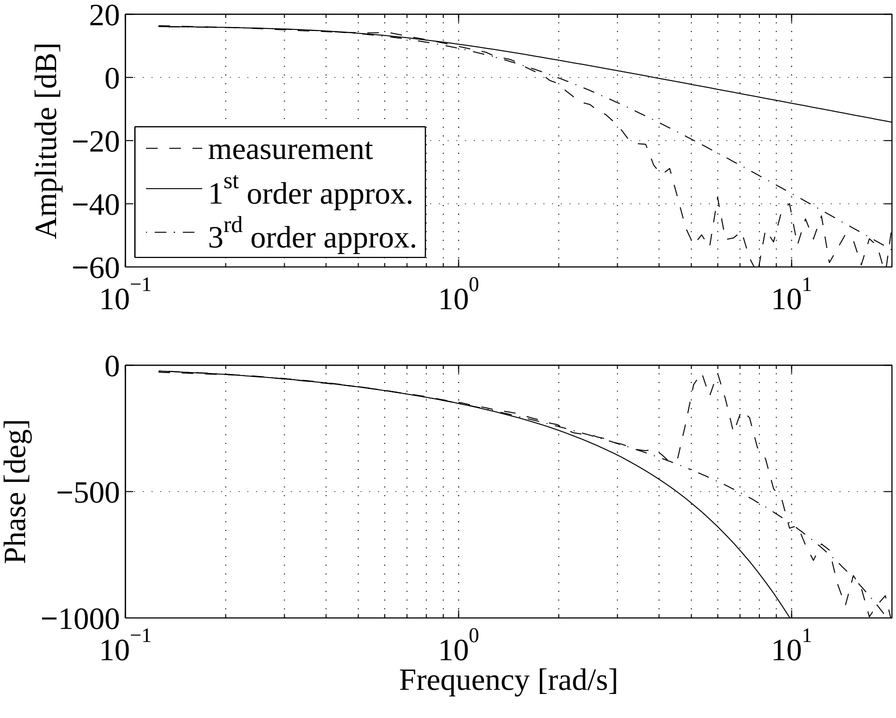

Figure 3.7: Bode plot of the path from u_{egr} to NO_x.

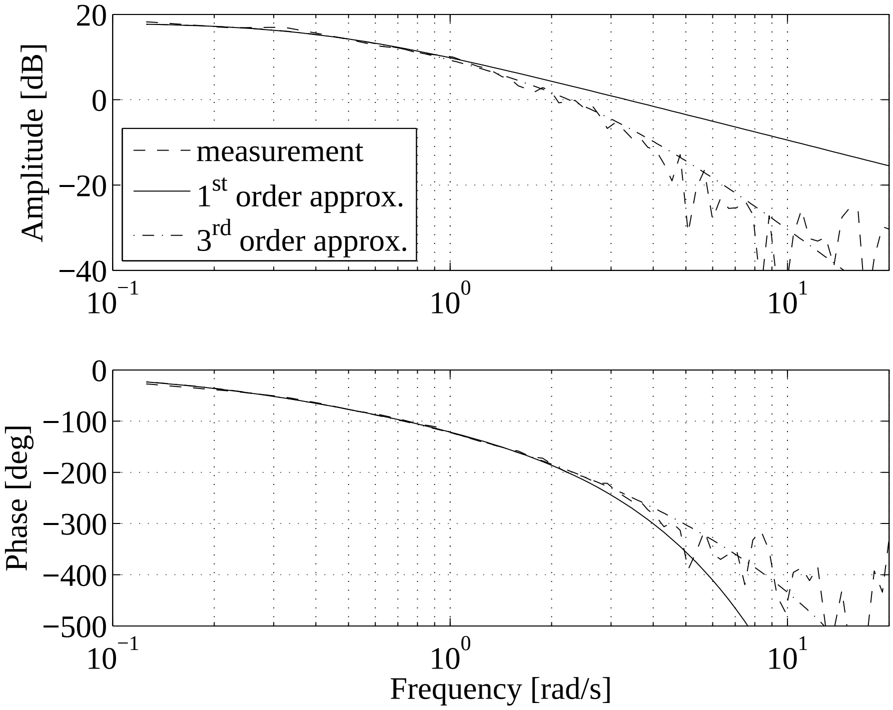

Figure 3.8: Bode plot of the path from SOI to NO_x.

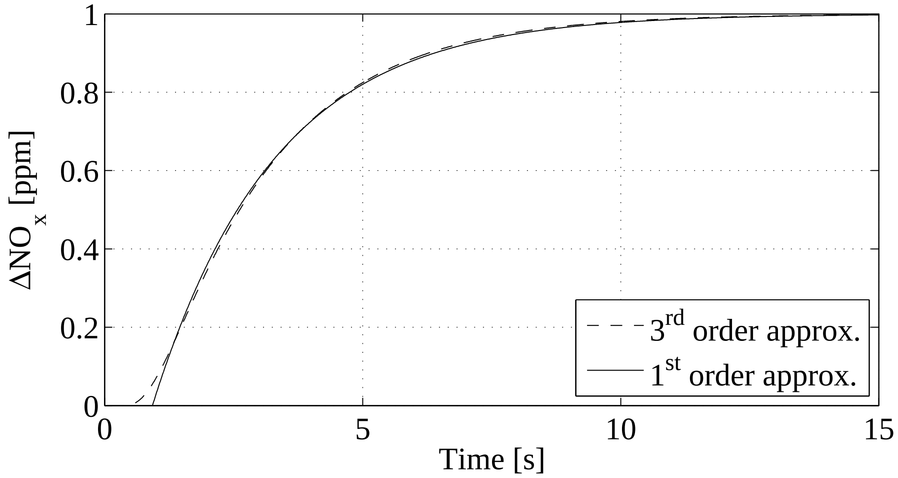

Figure 3.9: Unitary step response of the path from SOI to NO_x.

However, a plot of the step responses of the two approximations with different orders, as shown in Fig. 3.9, evidences that almost the same response is achieved with both the first-order and the third-order models. Only the path from SOI to NO_x is depicted, but this observation is valid for the path from u_{egr} to NO_x, as well. The low bandwidth of these two paths has to be attributed to the slow dynamics of the NO_x sensor.

The identification of the parameters of the simplified models of the three paths is carried out by means of a least-squares fitting in the complex plane, in order to get the best approximation for both the amplitude and the phase at the same time.

3.3 Plant Model

The experiment conducted in the previous section has been repeated in other operating points and a qualitatively similar behavior of the engine has been observed. It is thus possible to generalize the results obtained and to represent the plant model with a defined parametric structure in its entire operating range.

The multivariable engine plant can be characterized by the transfer matrix $P(s)$ as

$$P(s) = \begin{pmatrix} p_{11}(s) & 0 \\ p_{21}(s) & p_{22}(s) \end{pmatrix}, \tag{3.3}$$

where $p_{ij}(s)$ are the transfer functions of the paths from the j-th input to the i-th output for $i, j = 1, 2$ (cf. Fig. 3.1), consisting of a dynamic element $p_{0,ij}(s)$ and of a time delay $T_{d,ij}$, as

$$p_{ij}(s) = p_{0,ij}(s) \cdot e^{-sT_{d,ij}}. \tag{3.4}$$

As assumed in Sec. 3.1, the transfer function $p_{12}(s)$ from SOI to λ is equal to zero.

3.3.1 Plant Approximation

The 2×2 plant considered for the design of the controller is approximated with a simple structure that is able to maintain all of the fundamental characteristics of the more complex model and yet is appropriate for a parameter scheduling over the operating range of the engine to be considered. Therefore, the three paths are approximated using a first-order low-pass filter $p_{0,ij}(s)$ and one time delay element in each:

$$p_{ij}(s) = p_{0,ij}(s) \cdot e^{-sT_{d,ij}} = \frac{K_{ij}}{\tau_{ij}s + 1} \cdot e^{-sT_{d,ij}} , \tag{3.5}$$

where K_{ij}, τ_{ij}, and $T_{d,ij}$ are the static gain, the time constant, and the time delay of the plant, respectively. These parameters can be easily gain-scheduled as a function of the operating conditions of the engine.

3.3.2 Diagonalization of the Plant

After the simplification of the system by means of a low-order model, the plant is diagonalized before proceeding with the controller synthesis. In fact, the design of two independent SISO controllers, one for the AFR and one for the NO_x loop, is much easier and more intuitive than that of one single multivariable controller, in particular when the two control loops need to have different bandwidths.

The method proposed in [66] is applied to the engine plant for decoupling the NO_x channel from the AFR channel. A matrix $D(s)$ is sought such that the modified plant $G(s)$ is decoupled and thus diagonal, as

$$G(s) = P(s)D(s) = diag\{g_{11}(s), g_{22}(s)\} . \tag{3.6}$$

Expanding Eq. 3.6 as

$$\begin{pmatrix} p_{11}(s) & 0 \\ p_{21}(s) & p_{22}(s) \end{pmatrix} \cdot \begin{pmatrix} d_{11}(s) & d_{12}(s) \\ d_{21}(s) & d_{22}(s) \end{pmatrix} \overset{!}{=} \begin{pmatrix} g_{11}(s) & 0 \\ 0 & g_{22}(s) \end{pmatrix} , \tag{3.7}$$

the conditions that the matrix elements $d_{ij}(s)$ of the decoupler must satisfy are derived. Finally, the matrix $D(s)$ can be calculated as

$$D(s) = \begin{pmatrix} 1 & 0 \\ -\frac{p_{21}(s)}{p_{22}(s)} & 1 \end{pmatrix} \tag{3.8}$$

and the transfer function of the element $d_{21}(s)$ can be written explicitly as

$$d_{21}(s) = -\frac{K_{21}}{K_{22}} \cdot \frac{\tau_{22}s + 1}{\tau_{21}s + 1} \cdot e^{-s(T_{d,21} - T_{d,22})} . \tag{3.9}$$

Since for every operating point the condition $T_{d,21} > T_{d,22}$ is satisfied (in fact, the SOI is always applied after the intake valve closed), the causality of the decoupler matrix is guaranteed and since $\tau_{21} > \tau_{22}$, the decoupling term always has the characteristics of a lag element with the addition of a time delay. As the time constants τ_{21} and τ_{22} are mainly determined by the dynamics of the $\mathrm{NO_x}$ sensor, they are very similar in both channels. Therefore, the decoupling element behaves almost like a static gain with a pure delay element.

3.4 Solution to the Control Problem

The main information obtained in this chapter about the system to be controlled are the following: 1) The plant has a triangular structure, and thus, the multivariable control problem can be solved with the synthesis of two SISO controllers with the addition of a decoupling element; 2) the complex engine model can be simplified and approximated with low-order elements; and 3) the parameters of the simplified plant model can easily be gain-scheduled over the operating range of the engine. Using this information, a solution proposal for the control problem can be applied, as described in the next paragraphs.

As the measurement of an empirical model of the plant in every operating point (see Sec. 3.2) is very time consuming (and thus expensive), the reference model of the plant for the controller design is derived from a nonlinear and physics-based model of the engine. Actually, such a model contains the structure common to (almost) any modern diesel engine and thus, with only few measurements for calibrating its parameters, it can be easily transferred to other manufacturers. The nonlinear model must then be linearized around a defined grid of relevant operating points and approximated with low-order transfer functions, the parameters of which are stored in maps over the operating region of the engine.

Due to the particular triangular structure of the plant, the control problem can be divided into two parts that can be treated separately as SISO systems, namely the control of the AFR and that of the NO_x emissions. The AFR control loop is investigated first since, in absence of a connection between SOI and AFR, this loop can be considered completely independent from the NO_x channel. In order to quantify the tracking quality of the feedback controller designed with a simplified plant model, a robust controller-design method based on the full-order linear model of the plant is investigated and is used as reference. The experience accumulated with the AFR controller is then applied to the design of the NO_x control loop and the system is further extended with a decoupling element.

After demonstrating the validity and feasibility of the novel approach proposed for controlling the emissions of modern diesel engines, a control strategy is adopted that has the goal to minimize the fuel consumption.

Chapter 4

Nonlinear Engine Model

In order to automate the design process for the emissions controller, a model of the engine must be developed that describes the behavior of the engine in every point within its operating range. The physics-based nonlinear engine model consists of a mean-value model of the flows through the engine combined with a linear model for the prediction of the NO_x emissions.

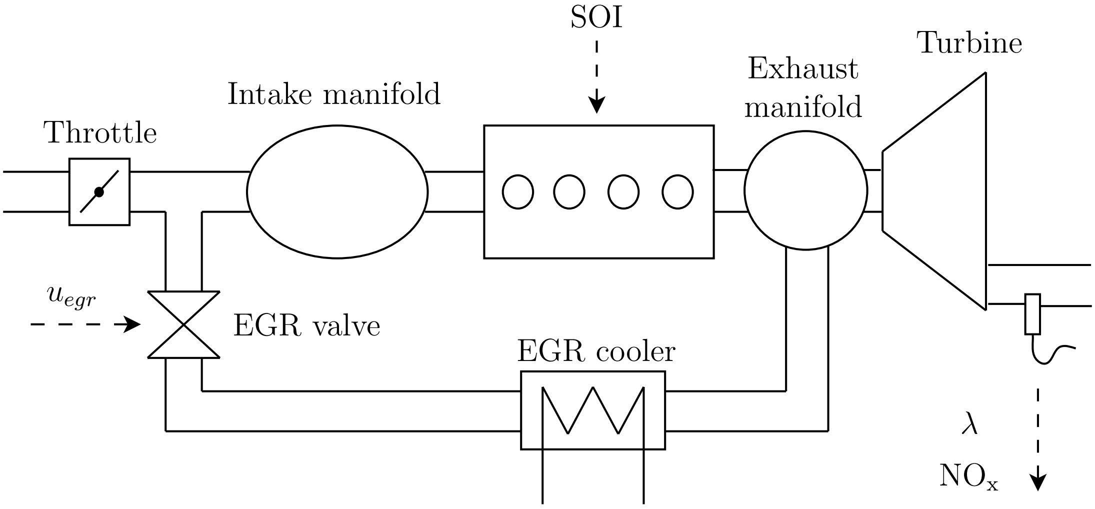
SOI
Turbine
Exhaust manifold
Intake manifold
Throttle
u_{egr}
EGR valve
EGR cooler
λ
NO_x

Figure 4.1: Simplified model of a compression ignited engine.

Due to the assumption that the boost pressure is regulated independently by the standard controller and since the sensors connected to the engine's ECU provide some of the necessary information (as for instance the boost pressure, the air temperature after the intercooler, the engine speed, the air mass flow, etc.), the model that describes the boost pressure dynamics, i.e., the air filter, the compressor, and the intercooler, can be omitted. Schematically, the components and boundaries of the reduced plant to be modeled are depicted in Fig. 4.1.

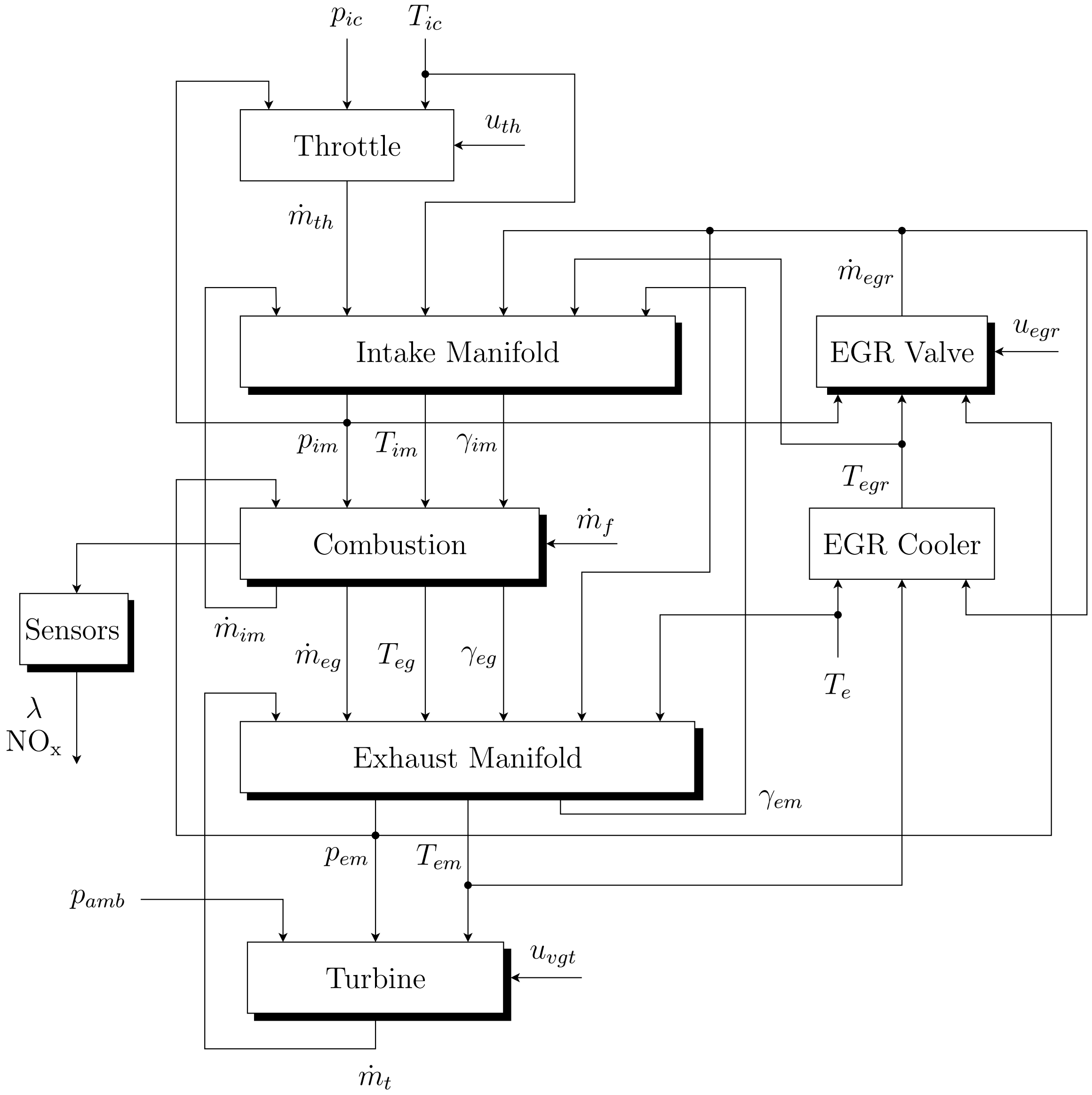
p_{ic}
T_{ic}
Throttle
u_{th}
$\dot{m}_{th}$
Intake Manifold
$\dot{m}_{egr}$
EGR Valve
u_{egr}
p_{im}
T_{im}
γ_{im}
T_{egr}
Combustion
$\dot{m}_f$
EGR Cooler
Sensors
$\dot{m}_{im}$
$\dot{m}_{eg}$
T_{eg}
γ_{eg}
T_e
λ
NO_x
Exhaust Manifold
γ_{em}
p_{em}
T_{em}
p_{amb}
Turbine
u_{vgt}
$\dot{m}_t$

Figure 4.2: Causality diagram of the simplified engine system.

The causality diagram depicted in Fig. 4.2 shows the interconnections between the subsystems of the partial engine model. Each subsystem is treated in detail in the next sections. The blocks with black shades contain dynamic terms, i.e. differential equations, while the other blocks contain algebraic calculations. In the case of the EGR valve, the turbine with variable geometry, and the AFR and NO_x sensors, the dynamics are referred to the actuators and sensors, respectively.

In this chapter, the nonlinear model of the engine flows including a static control-oriented NO_x model is presented, validated, and then linearized around a defined grid of operating points.

4.1 Mass Flow Through Orifices

A versatile method for modeling compressible fluids flowing through a restriction like the throttle, the EGR valve, and the turbine, is to assume an isothermal orifice. No losses during the fluid acceleration are assumed, i.e., all the potential energy is converted isentropically into kinetic energy, which is dissipated into thermal energy and thus no pressure recuperation takes place.

Using the thermodynamic relationships for isentropic expansion, the mass flow through an isothermal orifice can be calculated as

$$\dot{m} = cA\frac{p_{in}}{\sqrt{RT_{in}}}\Psi \,, \tag{4.1}$$

where p_{in} and T_{in} are the pressure and temperature upstream of the orifice, and c is the discharge coefficient. Defining Π as the ratio of the pressures downstream p_{out} and upstream p_{in} of the restriction, as

$$\Pi = \frac{p_{out}}{p_{in}} \,, \tag{4.2}$$

the flow function Ψ can be expressed as

$$\Psi = \begin{cases} \sqrt{\kappa\left[\frac{2}{\kappa+1}\right]^{\frac{\kappa+1}{\kappa-1}}} & \text{for} \quad p_{out} < p_{cr} \\ \Pi^{1/\kappa}\sqrt{\frac{2\kappa}{\kappa-1}\left[1-\Pi^{\frac{\kappa-1}{\kappa}}\right]} & \text{for} \quad p_{out} \geq p_{cr} \,, \end{cases} \tag{4.3}$$

where $\kappa = c_p/c_v$.

The critical pressure p_{cr}, which is achieved in the narrowest part of the device, determines when the flow reaches sonic conditions and is calculated as

$$p_{cr} = p_{in} \left[\frac{2}{\kappa + 1} \right]^{\frac{\kappa}{\kappa - 1}} . \tag{4.4}$$

According to [28], in order to prevent Ψ to have an infinite gradient at $\Pi = 1$, causing numerical problems during the simulation, the flow function is approximated as

$$\Psi = \begin{cases} 1/\sqrt{2} & \text{for} \quad p_{out} < \frac{1}{2} p_{in} \\ \\ \sqrt{2\Pi \left[1 - \Pi\right]} & \text{for} \quad p_{out} \geq \frac{1}{2} p_{in} \, . \end{cases} \tag{4.5}$$

4.1.1 Throttle

Diesel engines are generally operated with fully opened throttle. This device is actuated only during certain operating conditions with the scope to generate a pressure drop in the intake manifold, allowing thus higher EGR rates.

The mass flow through the throttle can be determined applying Eqs. 4.1 and 4.5, and inserting the respective parameters for the pressure p_{ic} and temperature T_{ic} after the intercooler, i.e. before the throttle, as

$$\dot{m}_{th} = c_{th} A_{th} \frac{p_{ic}}{\sqrt{R T_{ic}}} \Psi_{th} \, , \tag{4.6}$$

where $c_{th} = 1$ can be assumed. For the calculation of the flow function Ψ_{th} according to Eq. 4.5, the pressure ratio becomes $\Pi = p_{im}/p_{ic}$, with p_{im} defined as the intake manifold pressure.

The throttle area varies as a function of the scaled control variable $0 \leq u_{th} \leq 1$. Obviously, the throttle is never completely closed but has a bypass aperture φ_0. The effective opening angle φ of the throttle is determined as

$$\varphi = u_{th} \left(\frac{\pi}{2} - \varphi_0 \right) + \varphi_0 \tag{4.7}$$

and its area is calculated as

$$A_{th} = \frac{\pi d_{th}^2}{4} \left[1 - \frac{\cos\varphi}{\cos\varphi_0} \right] , \tag{4.8}$$

where d_{th} is the throttle diameter.

4.1.2 EGR Valve

The unknown parameter in the model for the calculation of the EGR mass flow $\dot{m}_{egr}$ is the valve area A_{egr}. Assuming a discharge coefficient equal to one, Eq. 4.1 becomes

$$\dot{m}_{egr} = A_{egr} \frac{p_{egr}}{\sqrt{RT_{egr}}} \Psi_{egr} . \tag{4.9}$$

Under the assumption that no pressure drop occurs over the EGR cooler, the pressure upstream of the valve p_{egr} can be set equal to the exhaust manifold pressure p_{em}, and thus the pressure ratio $\Pi = p_{im}/p_{em}$ can be applied to Eq. 4.5.

For the identification of the characteristic curve of the EGR-valve area as a function of its opening position y_{egr}, a measurement of the EGR rate is necessary. The direct measurement of the EGR rate with enough accuracy is not easy to achieve, since the EGR duct is very small and the soot contained in the recirculated gas fouls the measuring devices, making the measurement incorrect.

The EGR rate x_{egr} is defined as the amount of EGR mass flow divided by the total mass flowing through the intake manifold $\dot{m}_{im}$, which consists of the EGR mass flow and the fresh air mass $\dot{m}_a$ flowing through the throttle, as

$$x_{egr} = \frac{\dot{m}_{egr}}{\dot{m}_{im}} = \frac{\dot{m}_{egr}}{\dot{m}_{egr} + \dot{m}_a} . \tag{4.10}$$

The EGR mass flow is determined indirectly by means of static measurements of the CO_2 concentration in the intake and exhaust manifold (see [44], for instance) at different valve opening positions. Writing the balance in the intake manifold for the CO_2 mass flow under steady-state conditions

$$[CO_2]_{im}(\dot{m}_{egr} + \dot{m}_a) = [CO_2]_{em}\dot{m}_{egr} + [CO_2]_a\dot{m}_a \tag{4.11}$$

and neglecting the CO_2 concentration in the air $[CO_2]_a$, the EGR rate is determined by the following expression

$$\frac{[CO_2]_{im}}{[CO_2]_{em}} = \frac{\dot{m}_{egr}}{\dot{m}_{egr} + \dot{m}_a} = x_{egr} \, . \tag{4.12}$$

Therefore, the EGR mass flow can be calculated from the measured data as

$$\dot{m}_{egr} = \dot{m}_a \cdot \frac{x_{egr}}{1 - x_{egr}} \, . \tag{4.13}$$

Finally, by combining Eqs. 4.9 and 4.13, the characteristic curve of the EGR-valve area can be determined as depicted in Fig. 4.3.

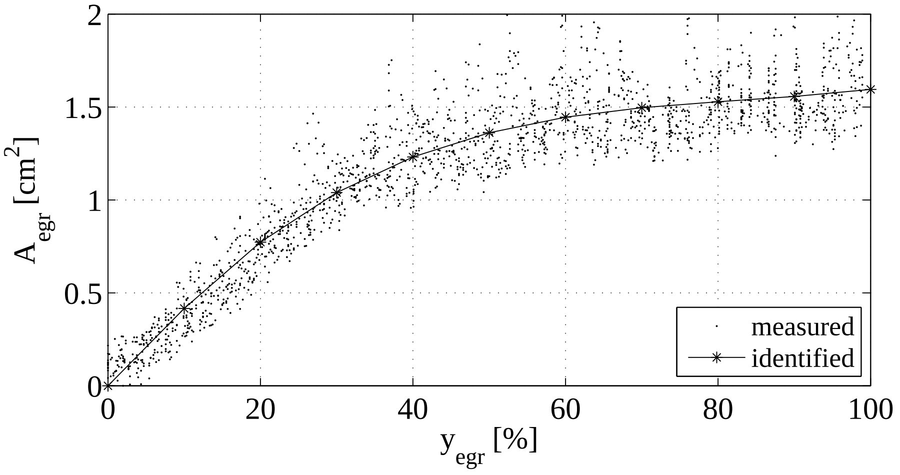

Figure 4.3: EGR-valve area as a function of its opening position.

The EGR valve is a critical element to be modeled, since its nonlinear characteristic curve strongly affects the static gain of the locally linearized plant and, therefore, the amplification of the resulting controller.

4.1.3 Turbine with Variable Geometry

The mass flowing through the VGT turbine can be calculated as suggested in [19], as

$$\dot{m}_t = \frac{p_{em}}{\sqrt{T_{em}}}\Phi_t\,. \tag{4.14}$$

The new variable Φ_t is defined as

$$\Phi_t = \frac{c \cdot A_t}{\sqrt{R}} \cdot \Psi_t \tag{4.15}$$

and depends on the two parameters c_t and k_t, as

$$\Phi_t = c_t\sqrt{1-\left(\frac{p_{amb}}{p_{em}}\right)^{k_t}}\,. \tag{4.16}$$

This structure represents a convenient method for determining the mass flow through a turbine. Thanks to measurements provided by the manufacturer, the two parameters can be identified easily and mapped for different positions of the turbine vanes. The new flow function Φ_t is depicted in Fig. 4.4 for five different vane positions as a function of the pressure ratio over the turbine $\Pi_t = p_{amb}/p_{em}$.

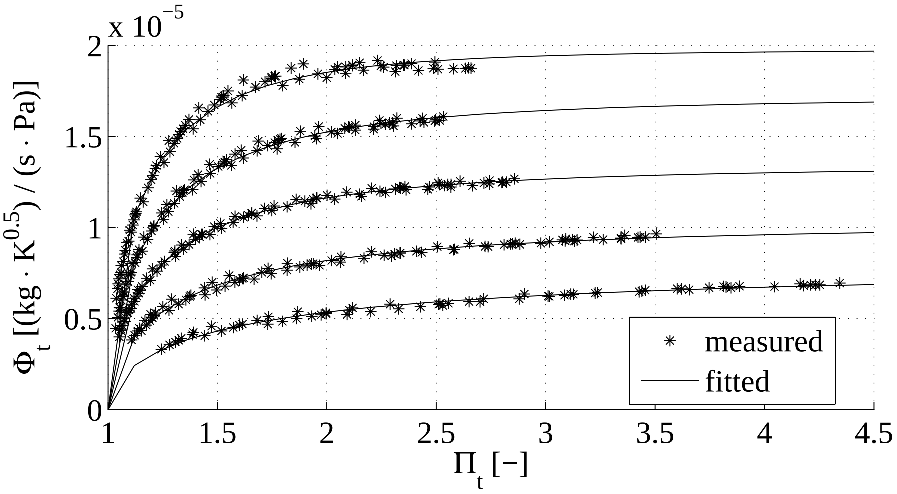

Figure 4.4: Turbine mass flow evaluated at different vane positions.

4.2 Air/Fuel Ratio

Diesel engines always work with an excess of air, i.e., with an AFR value of $\lambda > 1$. The steady-state value of the relative AFR of the fresh air/fuel mixture that enters the cylinder λ_{fc}, thus without taking into account the EGR and the remaining gas in the combustion chamber between one cycle and the next, is defined generally as

$$\lambda_{fc} = \frac{\dot{m}_a}{\dot{m}_f \sigma_0}\,, \tag{4.17}$$

where the stoichiometric factor σ_0 can be calculated from the chemical equation of the combustion reaction.

The combustion of hydrocarbon C_aH_b without oxygen excess, neglecting some secondary emissions, occurs according to the following chemical reaction [31]

$$C_aH_b + O_2 + \left(a + \frac{b}{4}\right)\left(O_2 + \frac{79}{21}N_2\right) \to aCO_2 + \frac{b}{2}H_2O + \frac{79}{21}\left(a + \frac{b}{4}\right)N_2\,. \tag{4.18}$$

For diesel fuel, that is assumed to consist of chains of $C_{14}H_{30}$ (thus with $a = 14$ and $b = 30$), the stoichiometric factor is

$$\sigma_0 = \frac{137(a + b/4)}{12a + b} = 14.88\,. \tag{4.19}$$

In order to compute the actual AFR of the exhaust gases during transient operations, both the internal and external EGR must be considered as well. Therefore, the amount of residual gas in the cylinder is estimated and a dynamical model for the gas mixing dynamics is proposed in the next subsections.

4.2.1 Residual Gas

The residual burnt gases that remain in the combustion chamber are due to the dead volume of the cylinder and can thus be roughly estimated by means of the compression ratio ϵ_c of the engine (for diesel engines $\epsilon_c \approx 20$).

The compression ratio is defined as

$$\epsilon_c = \frac{V_c + V_d}{V_c}\,, \tag{4.20}$$

where V_c is the compression volume and V_d the volume displaced by the engine. The residual gas fraction x_{rg} is proportional to V_c/V_d and amounts thus to approximatively 5%, as calculated in

$$x_{rg} = \frac{V_c}{V_d} = \frac{1}{\epsilon_c - 1} \approx 0.05\,. \tag{4.21}$$

According to [28], a better approximation can be obtained in relation to the engine speed N_e, as

$$x_{rg} = c_1 \cdot \frac{1}{N_e} + c_0\,, \tag{4.22}$$

where c_0 and c_1 are constants and x_{rg} varies between 4% and 8% in the considered operating range of the engine, i.e. from 1000 to 3200 rpm.

4.2.2 Gas Mixing Dynamics

As diesel engines operate with a substantial mass of recirculated exhaust gases that carry the AFR of past cycles and since the residual gases remaining in the cylinder have the AFR of the last cycle, these dynamics have to be considered for the calculation of the actual AFR at the exhaust valve. The model for the AFR dynamics developed below is an extension of that proposed in [28], to which the terms regarding the remaining burnt gases in the cylinder are added.

The nomenclature used is briefly explained before introducing the equations. The suffixes $(.)_{fc}$, $(.)_{rg}$, and $(.)_{egr}$ denote the fresh charge of air/fuel mixture, the residual gas (internal EGR), and the external EGR, respectively.

The relative AFR of the fresh charge has been already defined in Eq. 4.17, while that of the residual gas in the cylinder corresponds to the AFR of the last combustion cycle

$$\lambda_{rg} = \lambda(k-1)\,, \tag{4.23}$$

and that carried by the external EGR is the AFR of the t-th previous cycle, as

$$\lambda_{egr} = \lambda(k-t)\,. \tag{4.24}$$

Formulating a mass balance of the fresh charge and the burnt gases present in the cylinder after the intake valve closed, yields the following equation for the in-cylinder AFR $\lambda(k)$ at the cycle k

$$\lambda(k) = \frac{1}{\sigma_0} \cdot \frac{m_{fc} \cdot \frac{\lambda_{fc}\sigma_0}{1+\lambda_{fc}\sigma_0} + m_{rg} \cdot \frac{\lambda_{rg}\sigma_0}{1+\lambda_{rg}\sigma_0} + m_{egr} \cdot \frac{\lambda_{egr}\sigma_0}{1+\lambda_{egr}\sigma_0}}{m_{fc} \cdot \frac{1}{1+\lambda_{fc}\sigma_0} + m_{rg} \cdot \frac{1}{1+\lambda_{rg}\sigma_0} + m_{egr} \cdot \frac{1}{1+\lambda_{egr}\sigma_0}}\,. \tag{4.25}$$

Under the assumption that $\lambda_{(.)}\sigma_0 \gg 1$, the previous equation can be simplified as

$$\begin{aligned} \lambda(k) &\approx \frac{m_{fc} \cdot \lambda_{fc}\lambda_{rg}\lambda_{egr} + m_{rg} \cdot \lambda_{fc}\lambda_{rg}\lambda_{egr} + m_{egr} \cdot \lambda_{fc}\lambda_{rg}\lambda_{egr}}{m_{fc} \cdot \lambda_{rg}\lambda_{egr} + m_{rg} \cdot \lambda_{fc}\lambda_{egr} + m_{egr} \cdot \lambda_{fc}\lambda_{rg}} \\ &\approx (m_{fc} + m_{rg} + m_{egr}) \cdot \left(\frac{m_{fc}}{\lambda_{fc}} + \frac{m_{rg}}{\lambda_{rg}} + \frac{m_{egr}}{\lambda_{egr}} \right)^{-1}\,. \end{aligned} \tag{4.26}$$

This relation can also be written in the equivalent form

$$\frac{m_{fc} + m_{rg} + m_{egr}}{\lambda(k)} \approx \frac{m_{fc}}{\lambda_{fc}} + \frac{m_{rg}}{\lambda_{rg}} + \frac{m_{egr}}{\lambda_{egr}}\,. \tag{4.27}$$

4.2.3 Fresh Air Fraction

Since diesel engines always work with an excess of air, the exhaust gases always contain a determined amount of fresh air $\dot{m}_a$. The fresh air fraction γ can thus be defined as

$$\gamma = \frac{\dot{m}_a}{\dot{m}_{tot}}\,. \tag{4.28}$$

This quantity is indispensable for a precise calculation of some parameters that describe the properties of the exhaust gases, like for instance the specific heat at constant pressure c_p and at constant volume c_v. These two parameters can be expressed as a function of the air fraction γ_{im} in the intake and γ_{em} in the exhaust manifold (these state variables are introduced in the next section). In the case of the exhaust manifold, the specific heat $c_{.,em}$ is calculated as

$$c_{.,em} = \gamma_{em}(c_{.,a} - c_{.,eg}) + c_{.,eg} \, , \tag{4.29}$$

where $c_{.,eg}$ is the typical specific heat of the exhaust gases with $\lambda = 1$, and $c_{.,a}$ that of the fresh air, and in the case of the intake manifold, the specific heat $c_{.,im}$ can be expressed as

$$c_{.,im} = \gamma_{im}(c_{.,a} - c_{.,em}) + c_{.,em} \, . \tag{4.30}$$

4.3 Receivers

A receiver is a fixed volume V for which the thermodynamic states are assumed to be the same over the entire volume (lumped parameter system). As defined in [28], the main assumptions for modeling such an element are the following: 1) There are no substantial changes in the kinetic and potential energy of the flow; 2) the fluid is modeled as a perfect gas; and 3) the output parameters of the flow are the same as those in the receiver.

The dynamic equations that describe the states (pressure p, temperature T, and fresh air fraction γ) of such a system, considering the assumptions mentioned above, can be derived from the mass and the energy conservation laws, as

$$\begin{aligned}
\frac{dp}{dt} &= \frac{R}{c_v V}[c_{p,in} T_{in} \dot{m}_{in} - c_p T \dot{m}_{out} - \dot{Q}_{out}] \\
\frac{dT}{dt} &= \frac{T}{p}\left[\frac{dp}{dt} - \frac{RT}{V}(\dot{m}_{in} - \dot{m}_{out})\right] \\
\frac{d\gamma}{dt} &= \frac{RT}{pV}\left[\dot{m}_{in}\gamma_{in} - \dot{m}_{out}\gamma\right] - \frac{\gamma}{T}\left[\frac{dp}{dt} - \frac{p}{T}\frac{dT}{dt}\right] ,
\end{aligned} \tag{4.31}$$

where $(.)_{in}$ and $(.)_{out}$ represent quantities flowing into and out from the receiver, and R is the specific gas constant of air and of the exhaust gases. Such a receiver element can be used as the basis to model both the intake and the exhaust manifolds, as described in the next subsections.

4.3.1 Intake Manifold

The intake manifold is assumed to be an adiabatic system, i.e. no heat is exchanged through its walls. Substituting the inflow with the mass streaming from the throttle $\dot{m}_{th}$ and from the EGR valve $\dot{m}_{egr}$, and setting the outflow equal to the mass $\dot{m}_{im}$ flowing from the intake manifold into the engine, Eq. 4.31 becomes

$$\begin{aligned}
\frac{dp_{im}}{dt} &= \frac{R}{c_{v,im}V_{im}}[c_{p,a}T_{ic}\dot{m}_{th} + c_{p,em}T_{egr}\dot{m}_{egr} - c_{p,im}T_{im}\dot{m}_{im}] \\
\frac{dT_{im}}{dt} &= \frac{T_{im}}{p_{im}}\left[\frac{dp_{im}}{dt} - \frac{RT_{im}}{V_{im}}(\dot{m}_{th} + \dot{m}_{egr} - \dot{m}_{im})\right] \\
\frac{d\gamma_{im}}{dt} &= \frac{RT_{im}}{p_{im}V_{im}}[\dot{m}_{th} + \dot{m}_{egr}\gamma_{eg} - \dot{m}_{im}\gamma_{im}] - \frac{\gamma_{im}}{T_{im}}\left[\frac{dp_{im}}{dt} - \frac{p_{im}}{T_{im}}\frac{dT_{im}}{dt}\right] .
\end{aligned} \tag{4.32}$$

4.3.2 Exhaust Manifold

The heat exchange in the exhaust manifold cannot be neglected due to the large temperature difference between exhaust gases, engine, and ambient. A detailed calculation of the heat flux $\dot{Q}_{em}$ is presented in Sec. 4.4.2.

Substituting the inflow with the exhaust gas mass $\dot{m}_{eg}$ streaming out from the engine, and setting the outflow equal to the mass flowing into the EGR duct $\dot{m}_{egr}$ and that flowing through the turbine $\dot{m}_t$, Eq. 4.31 becomes

$$\begin{aligned}
\frac{dp_{em}}{dt} &= \frac{\kappa_{em}R}{V_{em}}\left[T_{eg}\dot{m}_{eg} - T_{em}(\dot{m}_t + \dot{m}_{egr}) - \frac{\dot{Q}_{em}}{c_{p,em}}\right] \\
\frac{dT_{em}}{dt} &= \frac{T_{em}}{p_{em}}\left[\frac{dp_{em}}{dt} - \frac{RT_{em}}{V_{em}}(\dot{m}_{eg} - \dot{m}_t - \dot{m}_{egr})\right] \\
\frac{d\gamma_{em}}{dt} &= \frac{RT_{em}}{p_{em}V_{em}}[\dot{m}_{eg}\gamma_{eg} - \dot{m}_{egr}\gamma_{em} - \dot{m}_t\gamma_{em}] - \frac{\gamma_{em}}{T_{em}}\left[\frac{dp_{em}}{dt} - \frac{p_{em}}{T_{em}}\frac{dT_{em}}{dt}\right] ,
\end{aligned} \tag{4.33}$$

with $\kappa_{em} = c_{p,em}/c_{v,em}$ and the fresh air fraction of the exhaust gas γ_{eg} defined with the help of Eq. 4.17, as

$$\gamma_{eg} = \frac{\dot{m}_a}{\dot{m}_a + \dot{m}_f} = \frac{\lambda_{fc} - 1}{\lambda_{fc}\sigma_0 + 1} \,. \tag{4.34}$$

4.4 Heat Exchange Processes

In this section the thermodynamic models of the heat exchange processes in the EGR cooler and in the exhaust manifold are presented. The mathematical relations and analogies used for the calculation of the heat transfer coefficients are taken from [32].

4.4.1 EGR Cooler

The EGR cooler can be modeled as a heat exchanger with a constant wall temperature T_w, as suggested in [17].

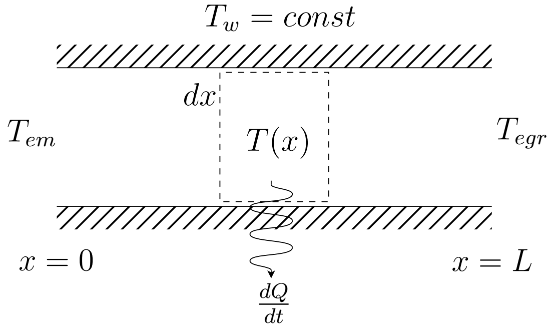

Figure 4.5: Heat balance on a control volume.

Considering a small control volume as depicted in Fig. 4.5 and assuming the heat transfer coefficient h and the specific heat c_p to be independent of the temperature T and of the position x, the heat flowing into the wall can be expressed as

$$-\frac{dQ}{dt} = \pi d \cdot dx \cdot h[T(x) - T_w] \,, \tag{4.35}$$

whereas the change of internal energy of the EGR mass flow is

$$\frac{dQ}{dt} = dT \cdot \dot{m}_{egr} \cdot c_p \,. \tag{4.36}$$

Combining Eqs. 4.35 and 4.36, yields the differential equation for the gas temperature

$$-\frac{dT}{dx} = \frac{\pi d h}{\dot{m}_{egr} c_p}(T(x) - T_w)\,. \tag{4.37}$$

The solution of this equation at $x = L$ corresponds to the temperature at the output of the EGR cooler T_{egr}, as

$$T(L) = T_{egr} = T_w + (T_{em} - T_w) e^{-\frac{\pi d h}{\dot{m}_{egr} c_p} L}\,. \tag{4.38}$$

Defining the cooler efficiency ε_{egr} as a function of the EGR mass flow, as

$$\varepsilon_{egr} = 1 - e^{-\frac{\pi d L \cdot h_{egr}}{c_p \cdot \dot{m}_{egr}}} \tag{4.39}$$

and approximating the wall temperature of the cooler with that of the cooling water of the engine T_e, Eq. 4.38 becomes

$$T_{egr} = T_{em} - \varepsilon_{egr}(T_{em} - T_e)\,. \tag{4.40}$$

The heat transfer coefficient h_{egr} for the internal convection between the fluid and the walls of the heat exchanger has to be identified, while the other geometric parameters can easily be estimated or measured.

The heat transfer coefficient can be determined with the help of the definition of the Nusselt number Nu

$$Nu = \frac{h_{egr} L}{k}\,, \tag{4.41}$$

where k is the thermal conductivity of the exhaust gas. By means of empirical analogies, the Nusselt number can also be calculated as a function of the Reynolds number and of the Prandtl number. Since for gases the Prandtl number is almost constant, the analogy can be written as

$$Nu = c_0 \cdot Re^{c_1}\,, \tag{4.42}$$

where c_i are empirical constants.

In the case of a circular pipe, the Reynolds number is defined as

$$Re = \frac{\rho_{egr} v_\infty d_{egr}}{\mu_{egr}} = \frac{\dot{m}_{egr} d_{egr}}{\mu_{egr} A_{egr}} = \frac{4\dot{m}_{egr}}{\pi d_{egr} \mu_{egr}} , \tag{4.43}$$

where μ is the dynamic viscosity, ρ the density, and v_∞ the velocity of the exhaust gases. Combining Eqs. 4.42 and 4.43, the relation for the heat transfer coefficient can be finally expressed as

$$h_{egr} = \frac{k_{egr}}{L_{egr}} Nu = \frac{k_{egr} c_0}{L_{egr}} \left(\frac{4\dot{m}_{egr}}{\pi d_{egr} \mu_{egr}} \right)^{c_1} = \alpha \cdot \dot{m}_{egr}{}^{\beta} . \tag{4.44}$$

A comparison between the measured and the calculated cooler efficiency is shown in Fig. 4.6.

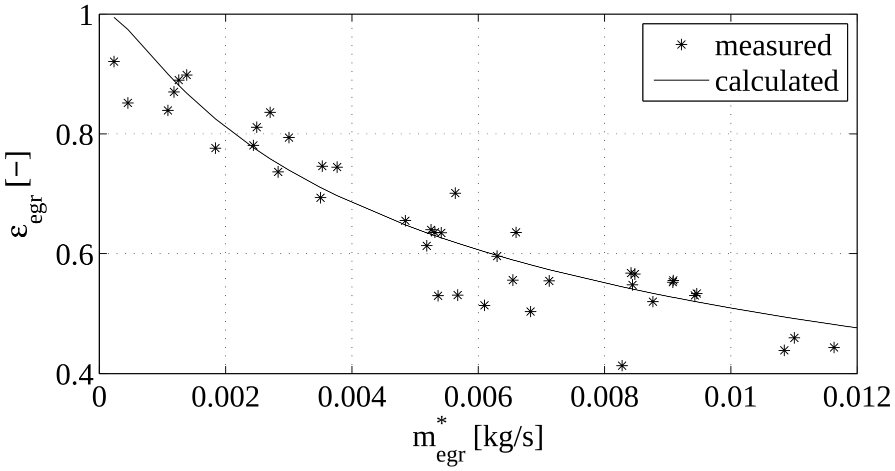

Figure 4.6: Efficiency of the EGR cooler.

4.4.2 Heat Exchange in the Exhaust Manifold

The heat exchange between the exhaust gases and the exhaust manifold in the tract between the cylinder output and the turbine input are attributed to many factors. The most important are the heat conduction along the exhaust pipe, the free convection to the ambient, and the energy dissipation due to radiation (see Fig. 4.7).

The form of the exhaust manifold is approximated by a thermodynamically well known geometry, i.e., a circular pipe with outside diameter d_{out},

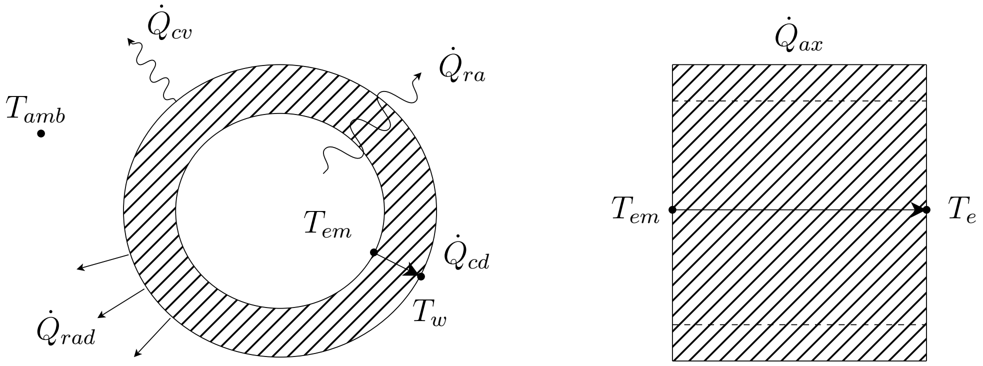

Figure 4.7: Radial and axial heat transfer model of the exhaust pipe.

inside diameter d_{in}, and length L. It is further assumed that the inside wall of the pipe has the same temperature as the exhaust gases (no internal convection is considered). This thermal system is modeled statically only.

The total heat exchange in the exhaust manifold $\dot{Q}_{em}$ is

$$\dot{Q}_{em} = \dot{Q}_{ax} + \dot{Q}_{ra}\,, \tag{4.45}$$

where $\dot{Q}_{ax}$ is the heat flowing in the axial direction, to the engine, and $\dot{Q}_{ra}$ that flowing in the radial direction, to the ambient.

In general, a heat flux $\dot{Q}$ from a source with the temperature T_1 to a sink with the temperature T_2 through a surface A can be expressed as

$$\dot{Q} = Ah(T_1 - T_2)\,. \tag{4.46}$$

Moreover, a new term is introduced that will be used in the next subsections, namely the heat transfer resistance r, defined as

$$r = \frac{1}{h}\,. \tag{4.47}$$

Axial Heat Exchange

The heat in axial direction flows from the wall of the exhaust manifold to the engine block. Assuming that the pipe wall has the same bulk temperature as the exhaust manifold, the heat source has the temperature T_{em} and the sink has the engine temperature T_e. Thus, the axial heat flux can be expressed as

$$\dot{Q}_{ax} = A_{sec} h_{ax} (T_{em} - T_e) \, . \tag{4.48}$$

The cross-section area A_{sec} through which heat is exchanged in axial direction corresponds to n_{cyl}-times the area of a hole circle ($n_{cyl} = 4$ in the case of a four-cylinders engine). The thermal resistance consists thus of the conductive resistance $r_{ax} = 1/h_{ax}$ only (Fig. 4.8).

The heat transfer coefficient in the case of conduction can be found in the literature for many simple geometries. In this case, the coefficient can be calculated as

$$h_{ax} = \frac{k}{L/n_{cyl}} \, , \tag{4.49}$$

where L/n_{cyl} is the length of the exhaust pipe equally subdivided between the number of cylinders.

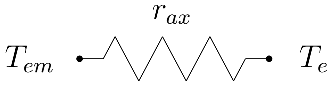

Figure 4.8: Axial heat resistance model of the exhaust pipe.

Radial Heat Exchange

The total thermal resistance is calculated from the circuit consisting of serial and parallel elements, as shown in Fig. 4.9.

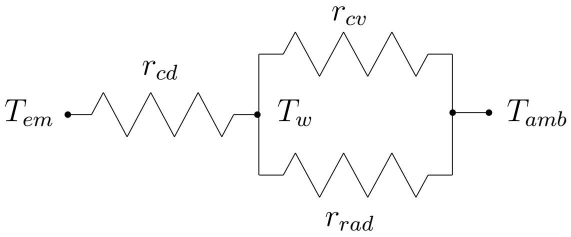

Figure 4.9: Radial heat resistance model of the exhaust pipe.

Neglecting the internal convection, the overall thermal resistance in the radial direction becomes

$$r_{ra} = r_{cd} + \left(\frac{1}{r_{cv}} + \frac{1}{r_{rad}} \right)^{-1} \, . \tag{4.50}$$

The equivalent representation of Eq. 4.50 in form of heat transfer coefficients is given by

$$\frac{1}{h_{ra}} = \frac{1}{h_{cd}} + \frac{1}{h_{cv} + h_{rad}} . \tag{4.51}$$

The heat flow can be finally calculated as

$$\dot{Q}_{ra} = A_{sh} h_{ra} (T_{em} - T_{amb}) , \tag{4.52}$$

where A_{sh} is the shell area of the cylinder.

Heat Transfer Coefficients

In the following paragraphs, the heat transfer coefficients are calculated for the different processes.

Radial conduction: As described in the literature, the heat transfer coefficient can be expressed as

$$h_{cd} = \frac{k_{em}}{\frac{d_{out}}{2} \ln\left(\frac{d_{out}}{d_{in}}\right)} . \tag{4.53}$$

Free convection: An empirical correlation based on the Rayleigh number can be found in the literature for a long isothermal cylinder. The Rayleigh number Ra is defined as the product of the Grashof number Gr and the Prandtl number Pr, as

$$Ra = Gr \cdot Pr = \frac{g\beta(T - T_\infty)d^3}{\nu^2} \cdot \frac{\nu}{\alpha} , \tag{4.54}$$

where α is the thermal diffusivity of the medium (in this case of air), ν its kinematic viscosity, g the gravity acceleration, and β is the reciprocal of the mean temperature between source and sink:

$$\beta = \frac{2}{T + T_\infty} . \tag{4.55}$$

In the case of the exhaust manifold $T = T_{em}$, $T_\infty = T_{amb}$ and $d = d_{out}$.

The heat transfer coefficient can be calculated from the definition of the Nusselt number, as

$$h_{cv} = Nu \cdot \frac{k_a}{d_{out}}\,, \tag{4.56}$$

where the Nusselt number is determined by the empirical formula

$$Nu = \left\{ 0.6 + \frac{0.387 Ra^{1/6}}{\left[1 + (0.559/Pr)^{9/16}\right]^{8/27}} \right\}^2 . \tag{4.57}$$

Radiation: The radiation energy is described by the following law

$$\dot{Q}_{rad} = A_{sh}\theta\zeta(T - T_\infty)^4\,, \tag{4.58}$$

where $\zeta = 5.6704 \cdot 10^{-8}$ is the Stefan-Boltzmann constant. The emissivity θ provides a measure of how efficiently a surface emits energy relative to a black body. In the case of the exhaust manifold, a value of $\theta = 0.6$ has been chosen. According to [17], developing the power in bracket of Eq. 4.58 and substituting $T = T_{em}$ and $T_\infty = T_{amb}$, leads to the following equation

$$\dot{Q}_{rad} = A_{sh}\theta\zeta(T_{em}^2 + T_{amb}^2)(T_{em} + T_{amb})(T_{em} - T_{amb})\,. \tag{4.59}$$

The heat transfer coefficient can be thus expressed as

$$h_{rad} = \theta\zeta(T_{em}^2 + T_{amb}^2)(T_{em} + T_{amb})\,. \tag{4.60}$$

4.5 Engine Processes

The processes that are directly related to the combustion or to the rotatory motion of the engine are modeled in this section. The discrete engine process is approximated as a continuous pump that introduces a mixture of fresh air, recirculated exhaust gases, and fuel in the combustion chamber, generating a determined amount of torque and then expelling the gas mixture with an increased temperature.

4.5.1 Volumetric Efficiency

The mass of the gas mixture flowing into the engine can be calculated as

$$\dot{m}_{im} = \rho_{im} \frac{V_d N_e}{120} \cdot c_T \cdot \eta_{vol}(N_e, p_{im}, T_{im}) \,, \tag{4.61}$$

where η_{vol} is the volumetric efficiency, c_T a correction factor, and the density ρ_{im} of the mixture of fresh air and exhaust gases in the intake manifold is defined as

$$\rho_{im} = \frac{p_{im}}{R_{im} T_{im}} \,. \tag{4.62}$$

Since diesel engines can operate with a large amount of EGR, a correction factor c_T is introduced that takes into account variations of the intake manifold temperature. This factor compensates for the expansion of the gas with respect to the reference temperature T_{ref} at which the map of the volumetric efficiency has been measured. As demonstrated experimentally (see Fig. 4.10), c_T varies linearly with the temperature difference in the intake manifold

$$c_T = a_1 \cdot (T_{im} - T_{ref}) + a_2 \,. \tag{4.63}$$

The parameters a_i are identified by comparing the measured intake manifold mass flow to that calculated from Eq. 4.61.

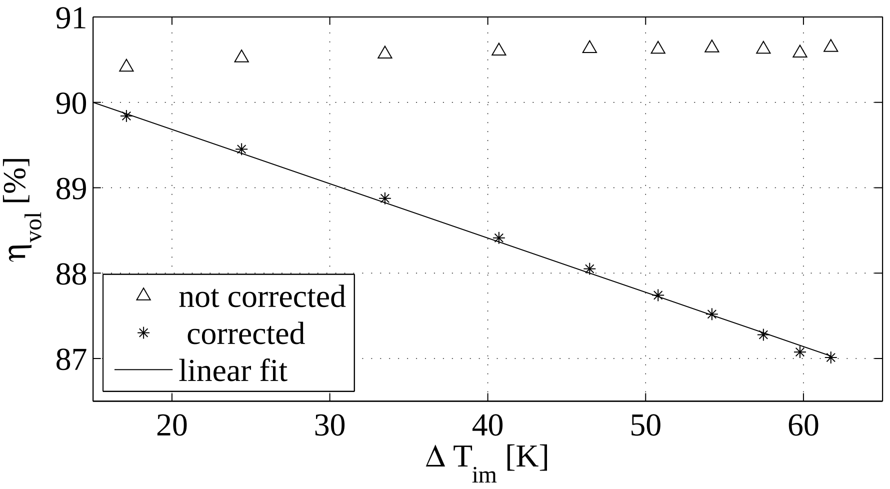

Figure 4.10: Volumetric efficiency as a function of the intake temperature variation in one sample operating point.

For the identification of η_{vol}, steady-state measurements of the engine are done in the operating range between 1000 and 3200 rpm and 0 and 10 bar BMEP. The data is saved in a 2D map as shown in Fig. 4.11.

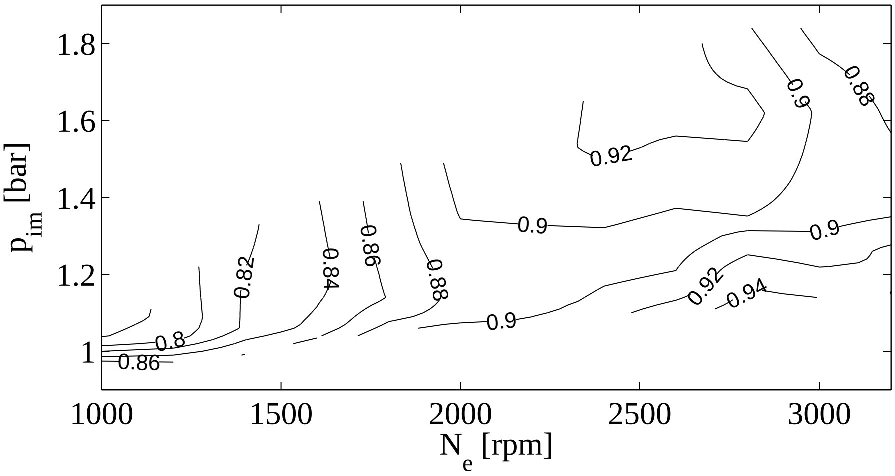

Figure 4.11: 2D map of the volumetric efficiency η_{vol}.

4.5.2 Torque Generation

The brake mean effective pressure p_{me} of an engine is defined as

$$p_{me} = \frac{M_e 4\pi}{V_d} \,, \tag{4.64}$$

where M_e is the engine torque and V_d the displaced volume. By transforming the fuel enthalpy H_f into a pressure acting on the piston, the fuel mean effective pressure p_{mf} can be defined as

$$p_{mf} = \frac{H_f m_f}{V_d} \,. \tag{4.65}$$

A theory that relates p_{me} and p_{mf} has been proposed in [26], which is known as “Willans approximation”

$$p_{me} = \eta_{thermo} \cdot p_{mf} - p_{me,0} \,, \tag{4.66}$$

where $p_{me,0}$ represents the engine losses and can be modeled as a function of the friction losses $p_{me,0f}$ and of the gas-exchange losses $p_{me,0g}$ as

$$p_{me,0} = p_{me,0f} + p_{me,0g} \,. \tag{4.67}$$

The first term depends on four unknown parameters k_i as

$$p_{me,0f} = k_1 \left(k_2 + k_3 \cdot S^2 \omega_e^2\right) \Pi_{e,max} \sqrt{\frac{k_4}{B}} \,, \tag{4.68}$$

with the engine speed $\omega_e = N_e \cdot \pi/30$ in [rad/s], while the second term represents the pressure drop over the engine

$$p_{me,0g} = p_{em} - p_{im} \,. \tag{4.69}$$

The internal thermodynamic efficiency η_{thermo} has a parabolic form (see Fig. 4.12) and can be modeled as a function of the three unknown parameters ϑ_i as

$$\eta_{thermo} = \vartheta_1 \cdot \omega_e^2 + \vartheta_2 \cdot \omega_e + \vartheta_3 \,. \tag{4.70}$$

Experimental results confirm the validity of the Willans approximation over a wide range of operating points (see Figs. 4.13 and 4.14). It can be noticed that the losses that the engine has to counteract amount to about 1.5 bar, which corresponds to 25 Nm for the engine considered.

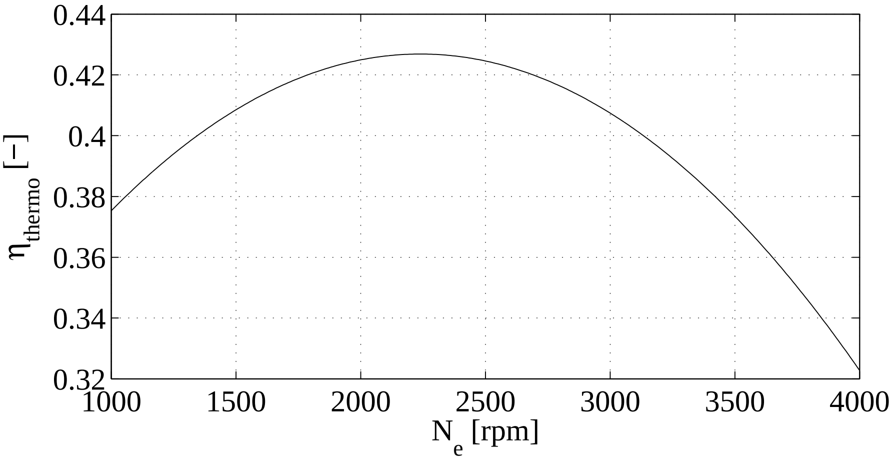

Figure 4.12: Thermodynamic efficiency of the engine.

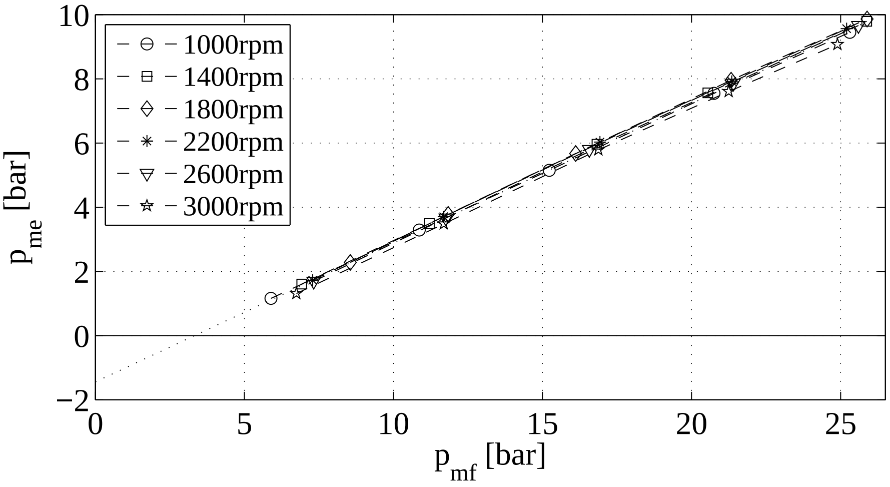

Figure 4.13: Willans approximation.

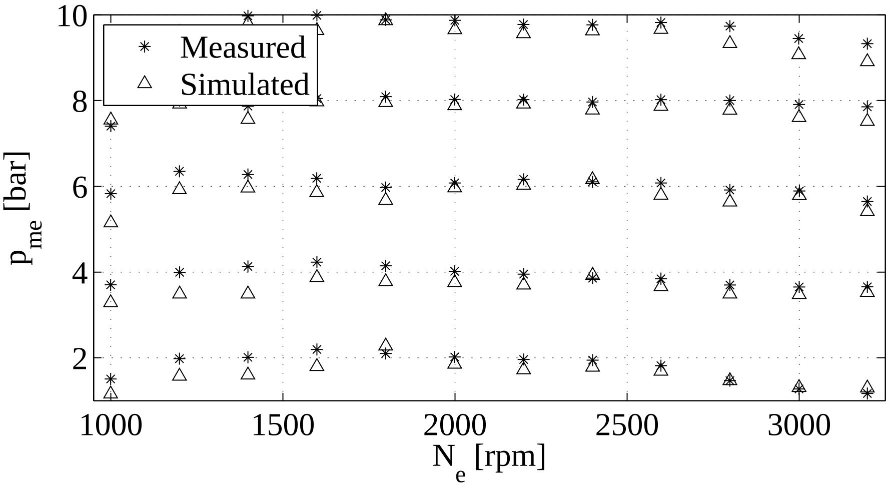

Figure 4.14: Identification of the brake mean effective pressure.

4.5.3 Temperature of the Exhaust Gases

The exhaust gases temperature mainly depends upon the engine load p_{me}. However, since the EGR can lower the combustion temperature considerably, this effect must be considered in the model. Therefore, the exhaust gas temperature is approximated as a function of the unknown parameters a_i as

$$T_{eg} = a_1 \cdot p_{me}^2 + a_2 \cdot p_{me} + a_3 \cdot \dot{m}_{egr} + a_4 \,. \tag{4.71}$$

A comparison between the measured and the identified data is depicted in Fig. 4.15.

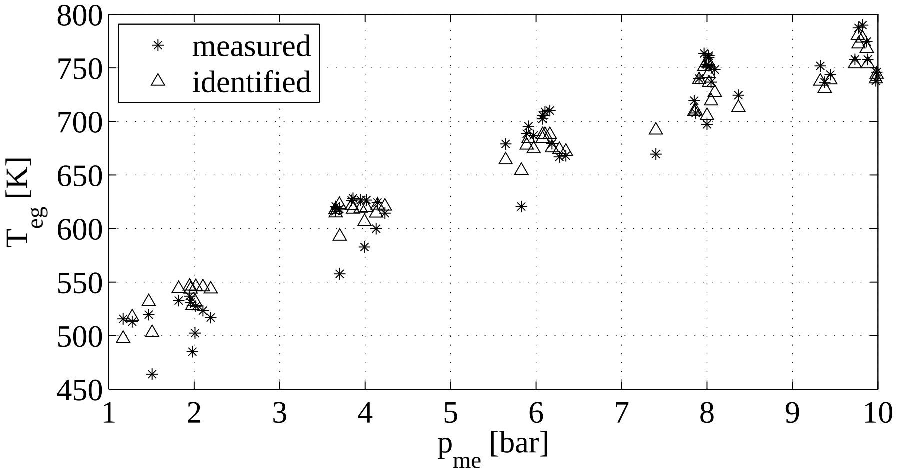

Figure 4.15: Identification of the exhaust gas temperature.

4.6 Modeling Time Delays

An important part of the system that has to be modeled exactly are the time delays. The total amount of time delay between the command signals of the actuators and the signals measured by the sensors are modeled as transport time, which is a function of the flow velocities, and as dead time of the sensors and actuators.

In order to determine the time delay, the control signals of the injection duration t_{inj} and of the EGR valve u_{egr} are excited and the time delay between the start of the excitation and the response measured by the AFR sensor has been measured (Fig. 4.16). The AFR sensor is used since it offers a fast reaction time and its dynamical behavior is well known.

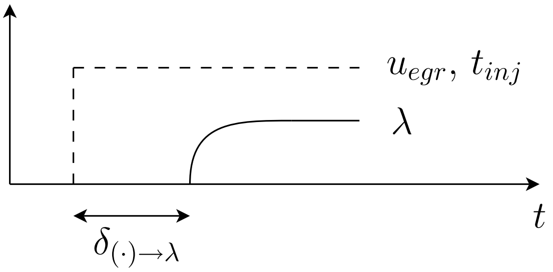

Figure 4.16: Measurement principle of the time delays.

By subdividing the total time delay measured as in Eq. 4.72, it becomes possible to determine all of the components δ_i.

$$\begin{aligned} \delta_{inj \to \lambda} &= \delta_{inj} + \delta_{em} + \delta_\lambda \\ \delta_{egr \to \lambda} &= \delta_{egr} + \delta_{im} + \delta_{ieg} + \delta_{em} + \delta_\lambda \end{aligned} \tag{4.72}$$

The sensor and actuator delays have been identified in Sec. 2.2 as $\delta_\lambda = 10$ ms and $\delta_{egr} = 20$ ms.

In the case of a step in the injection timing, there is always an uncertainty of up to the duration of one segment δ_{seg} since the start of the step signal is not synchronized with the injection system of the engine. Therefore $\delta_{inj} = [0 \ldots \delta_{seg}]$ can amount to up to 30 ms at low engine speeds. With this measurement, the unknown delay δ_{em} between the cylinder output and the AFR sensor can be estimated. Moreover, with the measurement of a step in the EGR-valve command signal, the unknown delay of the intake manifold δ_{im} can be calculated as well.

In the next paragraphs, the modeling of the variable time delays is explained in detail.

4.6.1 Delays Due to the Combustion Process

The segment time, i.e., the time that each cylinder of the four-strokes ($n_s = 4$) and four-cylinders ($n_{cyl} = 4$) engine needs for completing one combustion cycle is

$$\delta_{seg} = \frac{n_s/2 \cdot 60}{n_{cyl} \cdot N_e} = \frac{30}{N_e}\,. \tag{4.73}$$

The induction-to-exhaust delay is modeled according to [28] and amounts to about $\delta_{ieg} = 3\delta_{seg}$.

4.6.2 Delay in the Intake Manifold

From the continuity equation and the ideal gas law, the velocity v of a fluid in a pipe with section area A is given by

$$v = \frac{\dot{m}}{\rho A} = \frac{\dot{m} R T}{p A} , \tag{4.74}$$

Therefore the transport time of the gas in the intake manifold, after actuating the EGR valve, is approximated by the ratio of the manifold length L_{im} over the flow velocity

$$\delta_{im} = \frac{L_{im}}{v_{im}} = L_{im} \cdot \frac{\rho_{im} A_{im}}{\dot{m}_a} = L_{im} \cdot \frac{p_{im} A_{im}}{R T_{im} \dot{m}_a} . \tag{4.75}$$

The delay modeled is compared to that calculated from measurements as in Fig. 4.17.

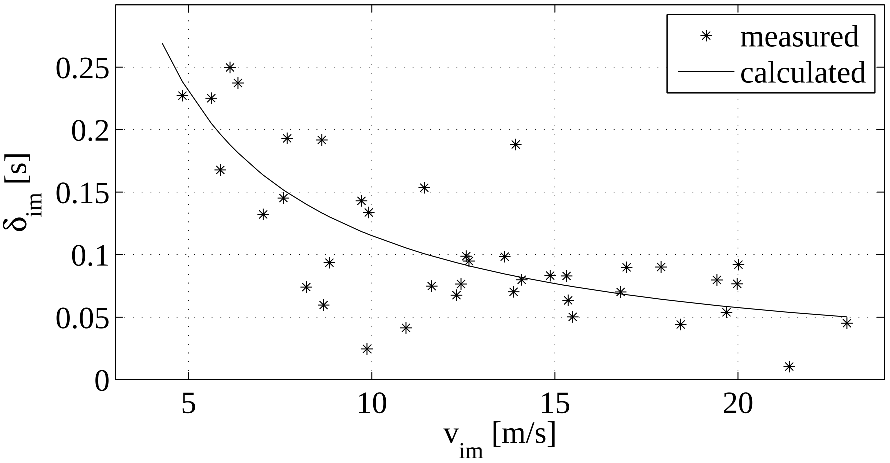

Figure 4.17: Transport delay in the intake manifold.

4.6.3 Delay in the Exhaust Manifold

The transport delay in the exhaust manifold from the cylinder output to the AFR and NO_x sensors can be modeled on the lines of Sec. 4.6.2 as a linear function of the ratio of the manifold length L_{em} over the flow velocity, as

$$\delta_{em} = \frac{L_{em}}{v_{em}} + \delta_{em,0} = L_{em} \cdot \frac{p_{amb} A_{em}}{R T_t \dot{m}_t} + \delta_{em,0} \,, \tag{4.76}$$

where the mass flow through the turbine $\dot{m}_t$ is calculated according to Eq. 4.14 and the cross section area A_{em} is the area of the exhaust pipe downstream the turbine. A correction factor $\delta_{em,0}$ has been introduced for better fitting the measurements.

A comparison between the delay modeled and that calculated from measurements is depicted in Fig. 4.18.

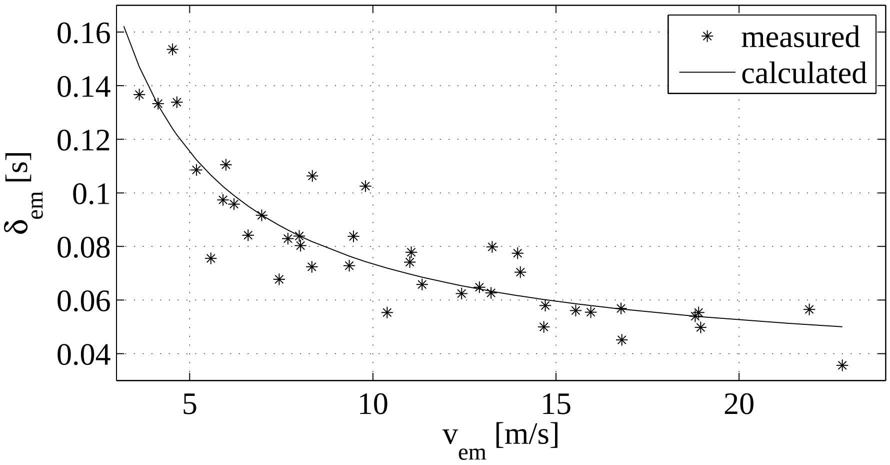

Figure 4.18: Transport delay into the exhaust manifold.

4.7 NO$_x$ Model

The static, linear, and control-oriented NO$_x$ model proposed in [54] is integrated into the mean-value model of the engine flows. This model is derived from a complex crank-angle based model and consists of maps of the static gains of the engine parameters relevant to the NO$_x$ production, as for instance the boost pressure, the injection duration, and the rail pressure. This model is thus able to predict variations of the NO$_x$ concentration from the nominal operating conditions by means of a linear extrapolation.

The interface between the mean-value model of the engine flows and the $\mathrm{NO_x}$ model is represented by the air mass flow $\dot{m}_a$ and the intake manifold pressure p_{im}, as depicted in Fig. 4.19. Aside from the SOI that is used as a control signal by the emissions controller, the other engine parameters do not vary from their nominal values and, thus, they do not contribute to change the $\mathrm{NO_x}$ concentration.

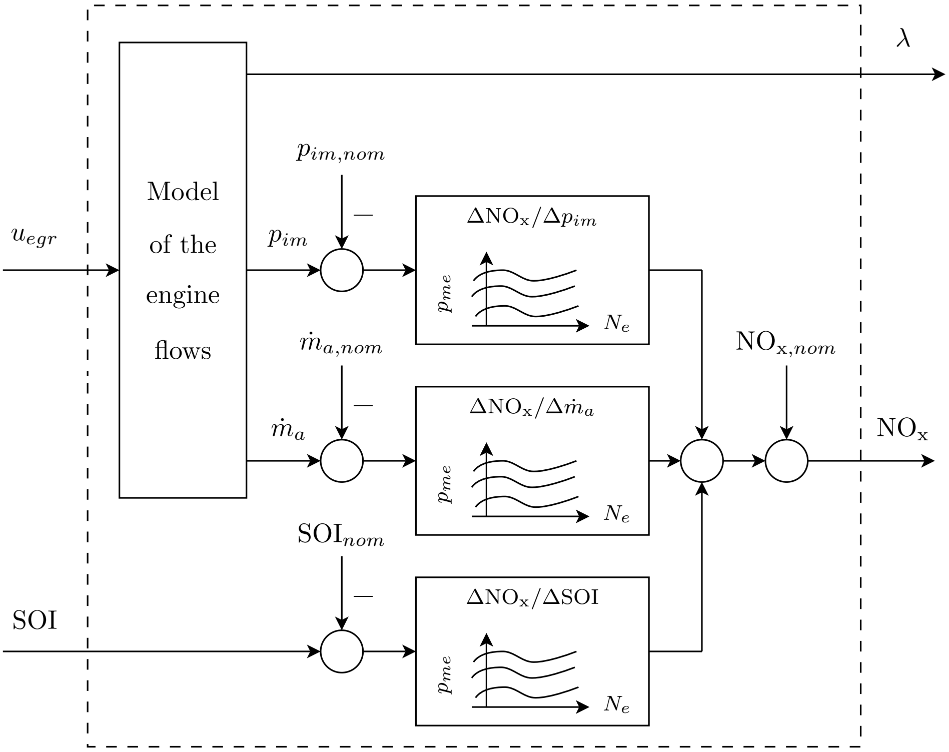
λ
Model of the engine flows
u_{egr}
$p_{im,nom}$
p_{im}
$-$
$\Delta\mathrm{NO_x}/\Delta p_{im}$
p_{me}
N_e
$\dot{m}_{a,nom}$
$\dot{m}_a$
$-$
$\Delta\mathrm{NO_x}/\Delta\dot{m}_a$
p_{me}
N_e
$\mathrm{NO}_{\mathrm{x},nom}$
$\mathrm{NO_x}$
SOI_{nom}
SOI
$-$
$\Delta\mathrm{NO_x}/\Delta\mathrm{SOI}$
p_{me}
N_e

Figure 4.19: Integration of the linear $\mathrm{NO_x}$ model in the engine model.

4.8 Validation of the Nonlinear Model

The nonlinear engine model is simulated during the European driving cycle MEVG-95 in order to prove the quality of its dynamical behavior. The courses of the simulated AFR and $\mathrm{NO_x}$ signals are compared to those measured on the test-bench engine as in Figs. 4.20 and 4.21.

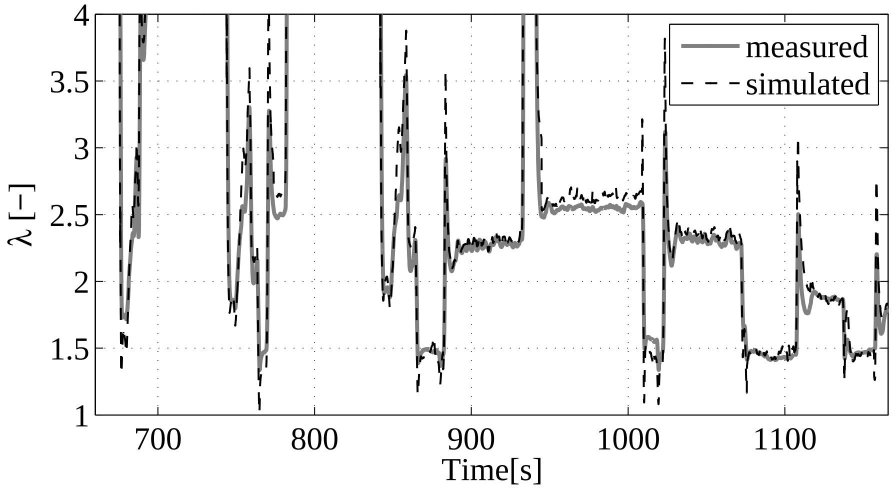

Figure 4.20: Simulated relative AFR during the MVEG-95.

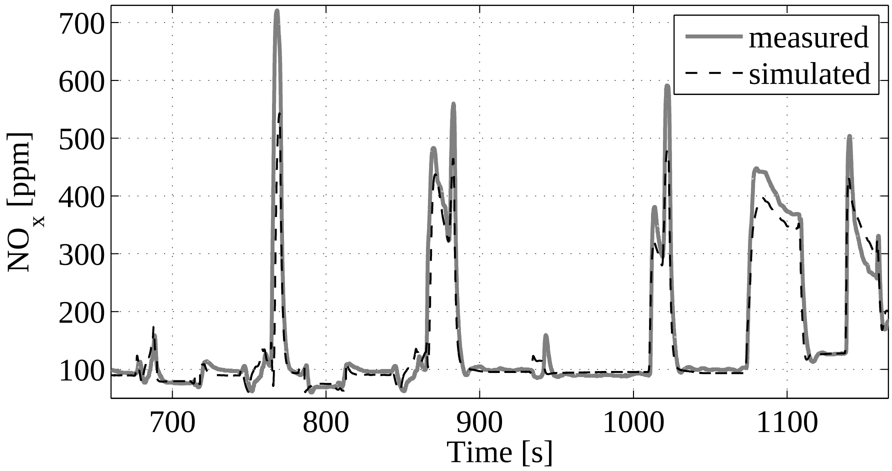

Figure 4.21: Simulated NO$_x$ concentration during the MVEG-95.

4.9 Linearization of the Engine Model

A linear model of the plant is indispensable for defining explicitly the parameters necessary for the design of the LPV-controller in the relevant operating points.

For establishing these relevant operating points, a quasi-static simulation (QSS) analysis [29] of the vehicle considered has been conducted for two driving cycles, namely the American FTP-75 and the European MEVG-95. The results showed that most of the time the engine is driven at less than 3200 rpm and at a BMEP of less than 10 bar. Therefore, only this range was considered for the investigations and was subdivided into a grid, as shown in Fig. 4.22 (idle has been set at 1000 rpm for convenience). Its mesh size has a width of 200 rpm and a height of 2 bar BMEP.

The engine model is thus linearized automatically in every point of this grid, from the two inputs u_{egr} and SOI to the two outputs λ and $\mathrm{NO_x}$ concentration.

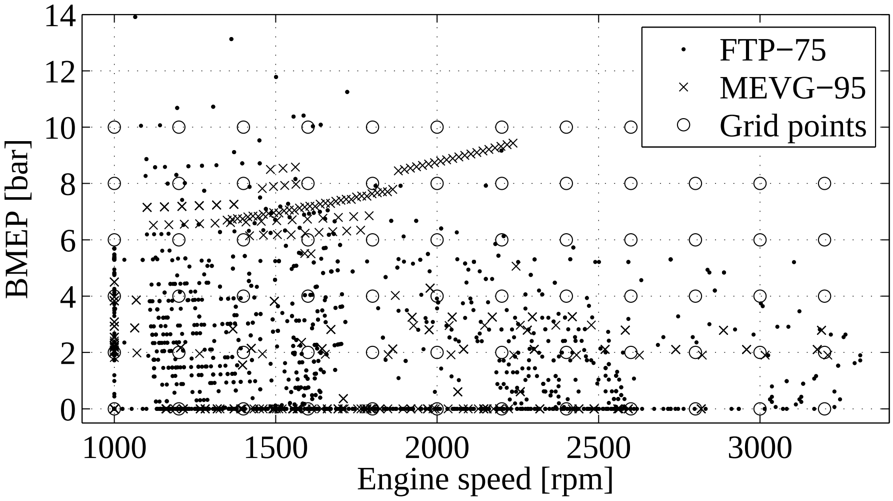

Figure 4.22: Results of the QSS simulations and grid of operating points chosen for the investigations.

4.9.1 Theory

A general nonlinear plant can be represented by the following equations

$$\begin{aligned} \dot{x}(t) &= f(x(t), u(t)) \\ y(t) &= g(x(t), u(t)) \end{aligned} \tag{4.77}$$

The linear state-space representation of the time invariant plant

$$\begin{aligned} \dot{x}(t) &= A \cdot x(t) + B \cdot u(t) \\ y(t) &= C \cdot x(t) + D \cdot u(t) \end{aligned} \tag{4.78}$$

implies the calculation of the Jacobian matrix, i.e., all the firts-order partial derivatives of the vector-valued functions $f(x, u)$ and $g(x, u)$. The system matrices for a plant with m inputs, p outputs, and n states can thus be expressed as follows

$$\begin{aligned} A &= \begin{bmatrix} \frac{\partial f_1}{\partial x_1} & \cdots & \frac{\partial f_1}{\partial x_n} \\ \vdots & \ddots & \vdots \\ \frac{\partial f_n}{\partial x_1} & \cdots & \frac{\partial f_n}{\partial x_n} \end{bmatrix}, \quad & B &= \begin{bmatrix} \frac{\partial f_1}{\partial u_1} & \cdots & \frac{\partial f_1}{\partial u_m} \\ \vdots & \ddots & \vdots \\ \frac{\partial f_n}{\partial u_1} & \cdots & \frac{\partial f_n}{\partial u_m} \end{bmatrix} \\ C &= \begin{bmatrix} \frac{\partial g_1}{\partial x_1} & \cdots & \frac{\partial g_1}{\partial x_n} \\ \vdots & \ddots & \vdots \\ \frac{\partial g_p}{\partial x_1} & \cdots & \frac{\partial g_p}{\partial x_n} \end{bmatrix}, \quad & D &= \begin{bmatrix} \frac{\partial g_1}{\partial u_1} & \cdots & \frac{\partial g_1}{\partial u_m} \\ \vdots & \ddots & \vdots \\ \frac{\partial g_p}{\partial u_1} & \cdots & \frac{\partial g_p}{\partial u_m} \end{bmatrix} \end{aligned} \tag{4.79}$$

4.9.2 Realization

Because of the complexity of the engine model, the most efficient way to carry out the linearization is to use powerful commercial tools that are available on the market. The tool used for the design, the simulation, and the investigation of the model is Matlab/Simulink, which contains a function called `linmod`. This function calculates analytically the Jacobian matrices of each block and put then them together to build the linear matrices of the complete system. In this way, high flexibility in the design is guaranteed due to the modularity of the system, and the prerequisites for the automatic controller-design procedure are satisfied.

The nonlinear model is linearized around each operating point defined as in Fig. 4.22. The steady-state operating point can be defined by a set of constant input values u_0 and by the inintial level of the integrators x_0. Only these two variables are required as input to the function `linmod`.

The vector u_0 is determined by the steady-state measurements of the test-bench engine in the respective operating point, while x_0 results from the model simulation. For this scope, the system is simulated with the constant input vector u_0 until the model has reached its equilibrium state, where the level of each integrator is stored.

The resulting linear system is of high order, mainly due to the approximation of the time delays (the order for the approximation with Padé elements has been chosen proportional to the duration of the delay). However, excluding the time delays, the order of the rational plant is only ten.

Chapter 5

SISO Air/Fuel-Ratio Controller

Due to the particular triangular structure of the plant, the emissions control problem is divided into two parts that can be treated as two independent SISO systems, namely the control of the AFR and that of the NO_x emissions, with the addition of a decoupling element for the two channels. The feasibility of a SISO AFR control loop is thus investigated in this chapter.

In order to be applied on a standard-production ECU, the proposed control system has to meet the following requirements: 1) The tracking quality of the AFR setpoint during a driving cycle has to be at least as good as that attained by using the conventionally controlled engine; 2) the application has to be simple, in order to avoid any fine-tuning of the controller on the test bench, and considering that the memory and the computing power of an ECU are limited; and 3) a high level of automatization in the entire design process of the controller has to be achieved in the design and parametrization of the controller.

Since the engine behaves differently at different operating point within its operating range, a controller is needed that is capable of perceiving these changes and of tracking the desired AFR setpoint reliably under varying operating conditions. In order to demonstrate that the behavior of the engine can be well approximated by a first-order element and a time delay (as assumed in Sec. 3.3.1), two approaches are investigated for the design of a gain-scheduled AFR controller. First, an internal model controller (IMC) is developed with a simplified model of the plant. This method was adopted in [67], for instance, where the air path of a diesel engine is approximated locally by a linear model whose structure is the same over the entire range of operating points. The resulting controller depends on the scheduled parameters of the plant. The IMC structure has the advantage that is easy to handle and can compensate for the time delays in the control loop. Second, an H_∞ controller is designed and parametrized starting from the full-order linear model of the plant. With this approach, locally linear controllers can be designed starting from a linear model, as proposed in [22]. A structurally suitable representation for the transfer functions of the controller has to be found so that its parameters can be mapped over scheduling variables [51].

In addition to the feedback structures, two feedforward controllers are investigated for improving the tracking quality of the system.

5.1 Analysis of the Plant

As assumed in Sec. 3.3.1, the plant considered in this chapter (from the EGR-valve control signal to the AFR sensor) for the design of the IMC controller is approximated as

$$p_{11}(s) = \frac{\hat{K}_{11}}{\hat{\tau}_{11} s + 1} \cdot e^{-s\hat{T}_{d,11}} \,. \tag{5.1}$$

The three parameters static gain $\hat{K}_{11}$, time constant $\hat{\tau}_{11}$, and time delay $\hat{T}_{d,11}$ are calculated during the linearization of the nonlinear model and then stored in look-up tables with the independent variables N_e and BMEP p_{me}. They are estimates of the real plant's parameters K_{11}, τ_{11}, and $T_{d,11}$.

The three parameters of the plant are depicted in Figs. 5.1–5.3. As expected, the higher the engine speed and load, the smaller the response time and delay of the plant.

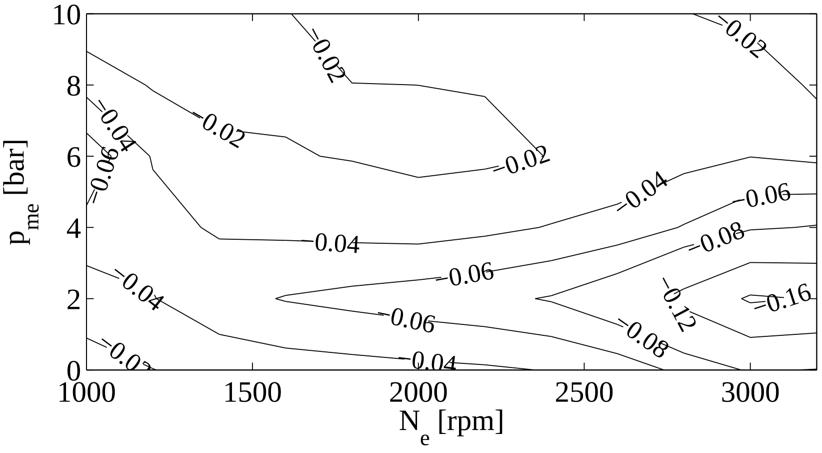

Figure 5.1: Map of $\hat{K}_{11}$ in [-/%].

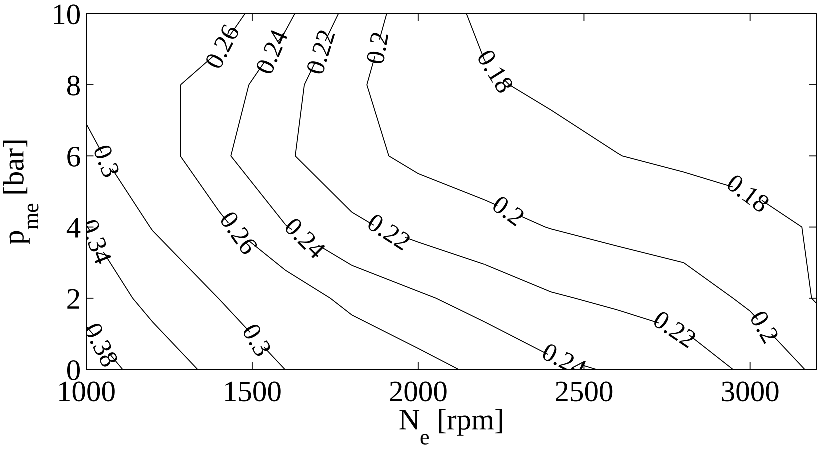

Figure 5.2: Map of $\hat{\tau}_{11}$ in [s].

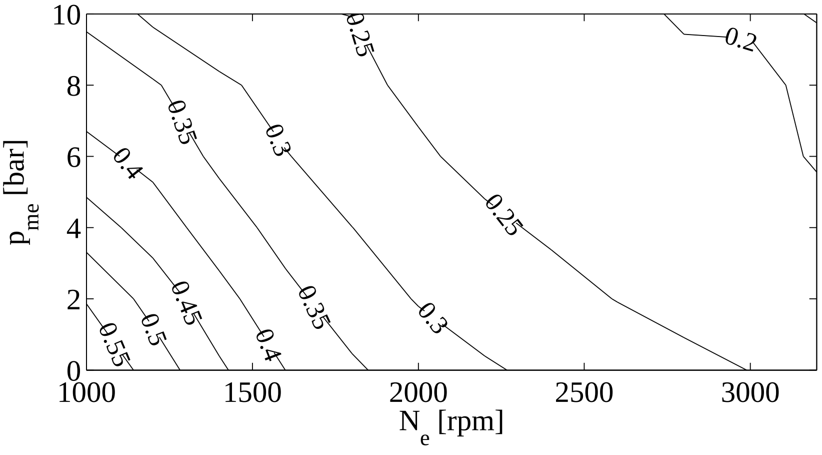

Figure 5.3: Map of $\hat{T}_{d,11}$ in [s].

5.2 Internal Model Controller

The IMC system considered here is based on the classical Smith predictor structure [58]. For its design, the plant $P(s)$ is approximated by the LPV model described by Eq. 5.1.

The controller is designed by forcing the target complementary sensitivity $T(s)$ to have low-pass filter characteristics [41], as expressed in

$$T(s) = \frac{1}{\xi s + 1} \cdot e^{-s\hat{T}_d}, \tag{5.2}$$

where ξ is the tuning parameter dependent on the operating point. Using the definition of the complementary sensitivity

$$T(s) = \frac{P(s)C(s)}{1 + P(s)C(s)}, \tag{5.3}$$

the controller transfer function $C(s)$ can be calculated as

$$C(s) = \frac{T(s)}{P(s)[1 - T(s)]} = \frac{\frac{\hat{\tau}s+1}{\hat{K}} \frac{1}{\xi s}}{1 + \frac{1}{\xi s}\left(1 - e^{-s\hat{T}_d}\right)}. \tag{5.4}$$

The resulting control system depicted in Fig. 5.4 thus depends explicitly on the plant parameters that are scheduled in maps during the linearization process and on a tuning factor ξ that has not been determined as yet. In order to integrate the calculation of this factor in the automated controller-design process, the control system is synthesized with constant robustness.

The nominal robustness of a control system is determined from its open-loop gain $L(s)$, which is expressed, in the case of perfect model matching, as

$$L(s) = P(s)C(s) = \frac{e^{-sT_d}}{\xi s + 1 - e^{-sT_d}}. \tag{5.5}$$

Choosing $\xi = T_d/\sigma$ and setting $\sigma = 1$, the open-loop gain becomes a function of sT_d only, and the form of $L(s)$ is the same for every T_d, and thus, for every operating point. In this way, the controller bandwidth is automatically adapted to the plant characteristics in the various operating points.

However, the bandwidth of the control system can be further adjusted by varying the parameter σ, for instance for fine-tuning the engine on the test bench in order to compensate for model uncertainties.

The phase margin achieved with the IMC structure and the plant considered here amounts to about $\varphi = 60°$. Simulations and test-bench experiments showed that this value guarantees sufficient robustness against modeling errors while limiting the overshooting of the system's step response at every operating point.

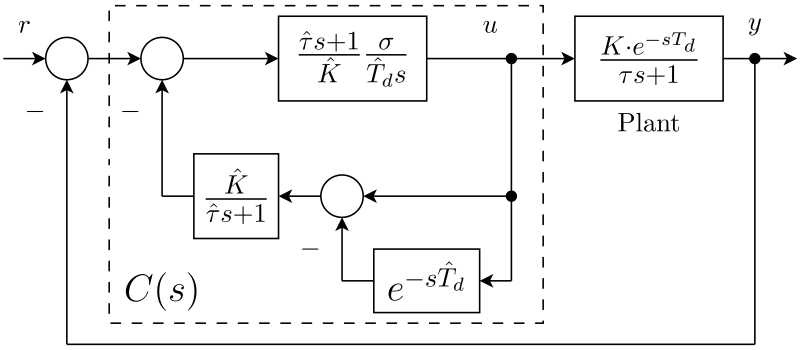
r
$-$
$-$
$\frac{\hat{\tau}s+1}{\hat{K}}\frac{\sigma}{\hat{T}_d s}$
u
$\frac{K\cdot e^{-sT_d}}{\tau s+1}$
Plant
y
$\frac{\hat{K}}{\hat{\tau}s+1}$
$-$
$e^{-s\hat{T}_d}$
$C(s)$

Figure 5.4: Structure of the internal model controller.

5.3 H_∞-Method

The H_∞ method as introduced by [15] is a model-based method for designing robust linear controllers starting from linear plant models. The full-order linearized model of the path $p_{11}(s)$ is used.

The complete theory behind the H_∞ control design is rather complex. Since this work is focused on the *application* of the design method and since software functions that solve the H_∞ design algorithm are available on the market, only the information necessary for the application of the design procedure is introduced. Further details on the H_∞ control problem and on its solutions for systems including time delays can be found in [14, 16, 39, 50], for instance.

In this thesis, the $S/KS/T$ weighting scheme (Fig. 5.5) is used in order to achieve the desired shape of the singular values of the sensitivity $S_e(s)$, the complementary sensitivity $T_e(s)$, and the series compensator $R(s) =$

$C(s)S_e(s)$ over the entire frequency spectrum.

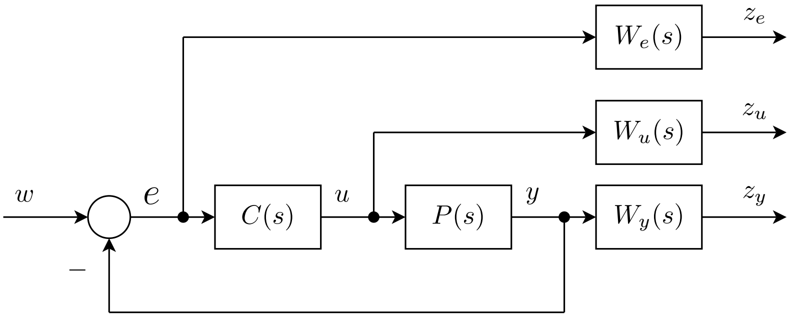

Figure 5.5: Standard $S/KS/T$ weighting scheme.

The ∞-norm of the transfer function T_{zw} of the extended plant from the input w to the output z_i as in Eq. 5.6 has to be minimized.

$$\|T_{zw}\|_\infty = \left\| \begin{bmatrix} W_e S_e \\ W_u C S_e \\ W_y T_e \end{bmatrix} \right\|_\infty \leq \gamma \tag{5.6}$$

Typically, the value $\gamma = 1$ is chosen, which means that the maximum singular value of the weighted terms will be limited by the inverse of the weighting functions $W_i(s)$ for the entire spectrum of frequencies.

The weighting functions used in this work are chosen as in Eqs. 5.7–5.9, where the parameters A_i and B_i are the asymptotes of the singular values of $W_i^{-1}(s)$ for $s \to \infty$ and $s \to 0$, respectively, while ω_{bi} define their bandwidths.

$$W_e(s) = \frac{s/A_e + \omega_{be}}{s + \omega_{be} \cdot B_e} \tag{5.7}$$

$$W_y(s) = \frac{s + \omega_{by}/B_y}{A_y \cdot s + \omega_{by}} \tag{5.8}$$

$$W_u(s) = \frac{s + \omega_{bu}/B_u}{A_u \cdot s + \omega_{bu}} \tag{5.9}$$

The singular values of the weighting functions in one representative operating point are depicted in Fig. 5.6. The bottom plot clearly shows that with the specifications for W_u, the controller gain is forced to decrease at high frequencies. This yields the desired smooth control signal.

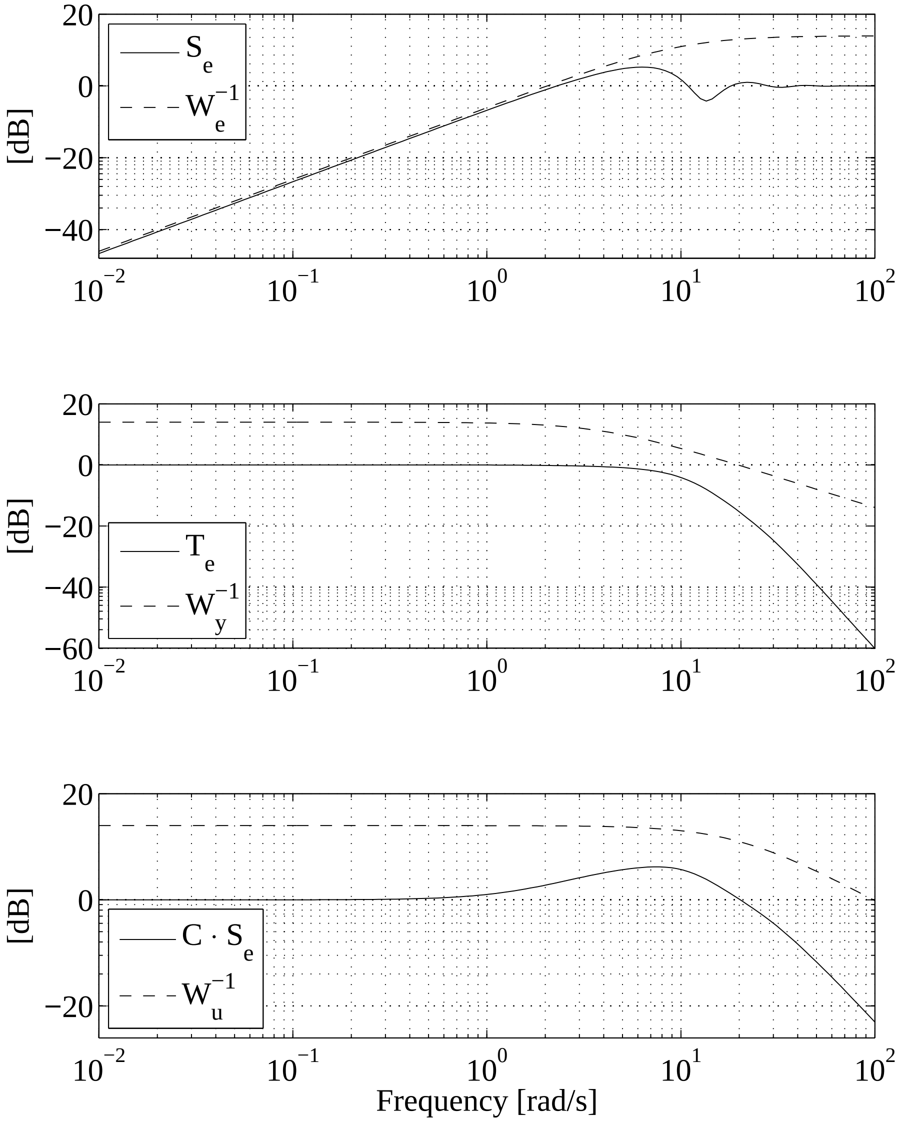

Figure 5.6: Singular values of the weighting functions for the $S/KS/T$ scheme in one representative operating point.

5.3.1 Automatic Design of the Controller

The controller design process has been automated by holding all the parameters A_i, B_i, and ω_{bi} constant, except the parameter ω_{be}. A similar automation criterion as in the case of the IMC controller is applied, namely ω_{be} is optimized by forcing the phase margin φ of the control system to be constant over the entire range of operating points.

An analysis of the resulting map for ω_{be} (Fig. 5.7) showed that this parameter depends on the plant's time delay T_d as in Eq. 5.10, which agrees with that demonstrated in [22].

$$\omega_{be}(T_d) = c_1 \cdot \frac{1}{T_d} + c_0 \, . \tag{5.10}$$

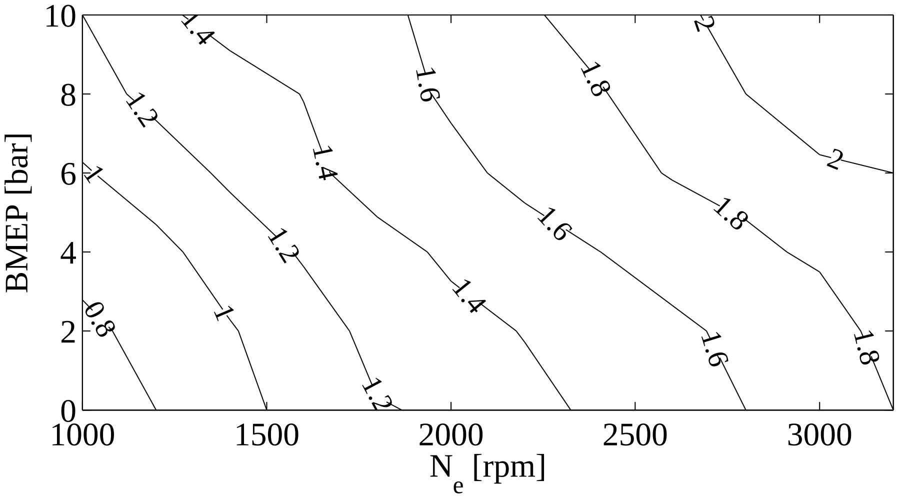

Figure 5.7: Map of ω_{be} in the engine operating range in [rad/s].

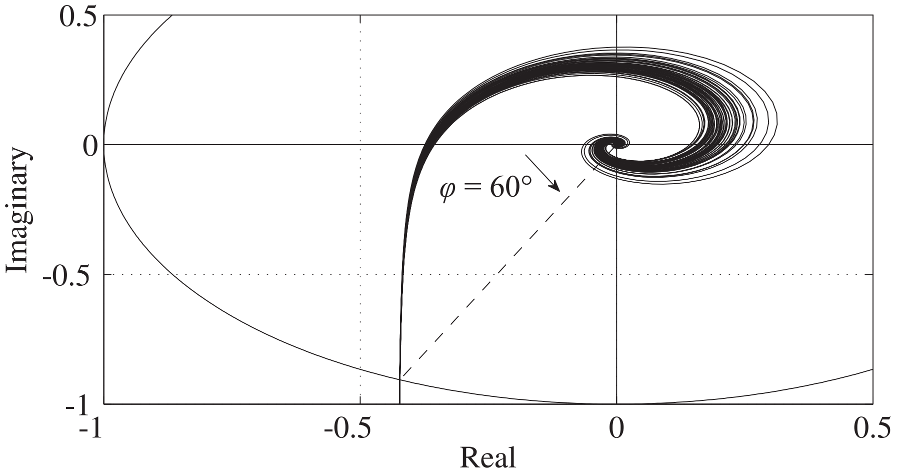

Figure 5.8: Nyquist plot of the $L(s)$ in all the operating points.

A value of $\varphi = 60°$ was chosen (Fig. 5.8), which is the same phase margin as that obtained with the IMC structure. The parameters of Eq. 5.10, $c_0 = 0.31$ and $c_1 = 0.54$, are determined experimentally and are strictly related to the local linear model used for the design of the controller. A general expression for φ as a function of those parameters thus cannot be written, but ω_{be} has to be calculated by the optimization process, in order to avoid numerical problems.

5.3.2 Parametrization of the Controller

The key idea for the parametrization of the H_∞ controller is to find a structure common to the entire family of controllers that are designed automatically for the various operating points and to vary its parameters as a function of the engine's operating conditions. Since the form of the Bode diagrams is similar in every operating point (one sample point is shown in Fig. 5.9), the resulting local H_∞ controllers can be approximated each by a system with a fixed structure and varying parameters.

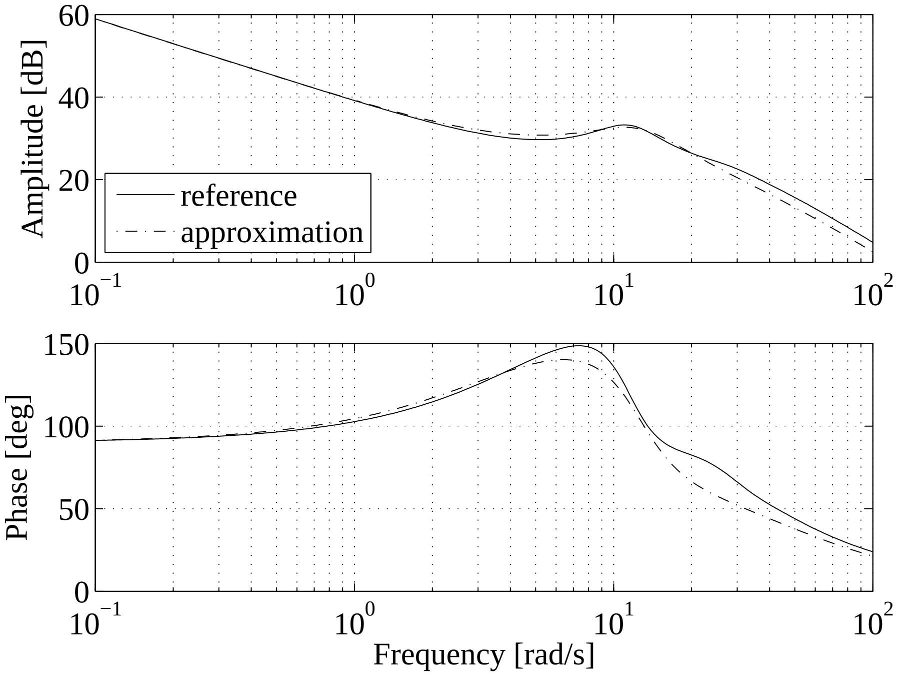

Figure 5.9: Bode diagram of the reference and of the approximated H_∞ controllers in one sample operating point.

In this work, the structure consists of a serial connection of simple elements, namely a PI element to which a differentiating term, to which a resonance element and a first-order low-pass filter are added (Fig. 5.10), for a total of six parameters. With this fixed structure, the parameters of each element can be identified via a least squares fit of the Bode diagrams and stored in maps with the gain-scheduling variables N_e and BMEP.

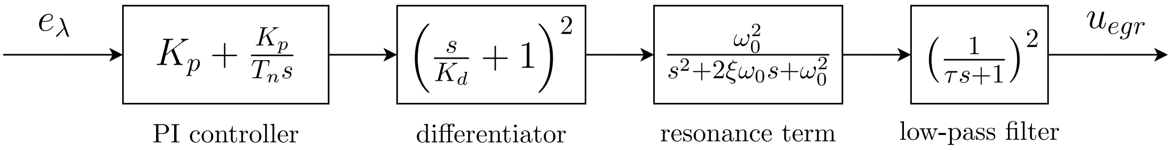
e_λ
$K_p + \frac{K_p}{T_n s}$
$\left(\frac{s}{K_d}+1\right)^2$
$\frac{\omega_0^2}{s^2+2\xi\omega_0 s+\omega_0^2}$
$\left(\frac{1}{\tau s+1}\right)^2$
u_{egr}
PI controller
differentiator
resonance term
low-pass filter

Figure 5.10: Approximation of the transfer function of the H_∞ controller.

5.4 Comparison of the Feedback Controllers

A qualitative comparison of the Nyquist plot of the control system achieved with the IMC and with the H_∞ controllers is depicted in Fig. 5.11 for a sample operating point. The two design methods applied to the respective plant models, although very different, produced very similar results. This fact is encouraging since the controller obtained with a simple plant model together with a simple design method has almost the same characteristics as that obtained with a much more complex plant and design method.

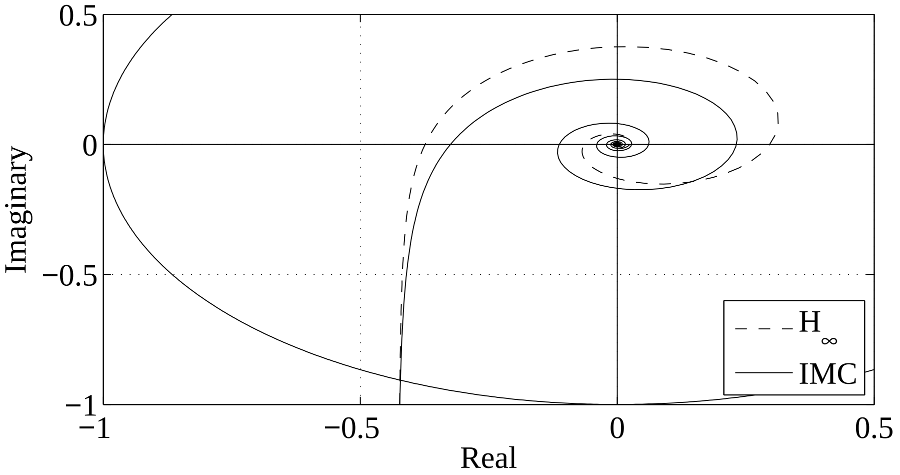

Figure 5.11: Nyquist plot of $L(s)$ in one operating point.

Although both design methods produce locally stable and robust control systems, it is important to say that, in general, the stability and the robustness of a gain-scheduled feedback controller are not guaranteed a priori [57]. These properties have to be verified extensively by testing.

5.5 Static Feedforward Controllers

A change of the engine's operating conditions can be interpreted as a disturbance to the control system in equilibrium. Since the fuel path is much faster than the air path, during sudden accelerations, in a first instant the AFR decreases very quickly before reaching its steady-state value, and during this time an unacceptable amount of PM is produced. Thus, a feedforward controller is needed for achieving good responses during fast transient operations.

Two static feedforward elements are proposed and analyzed in this section. The first element is based on the static inversion of the nonlinear engine model that estimates the EGR-valve command signal as a function of the desired AFR and of other engine parameters. The second element consists of a linear disturbance compensator that calculates only variations in the control signal for the EGR valve.

The compensation of the negative overshooting of the AFR during sudden acceleration is of course not complete, because it is limited by the EGR-valve actuator itself.

5.5.1 Nonlinear Feedforward Controller

The static inversion of the nonlinear engine model presented in Chap. 4 leads to the causality diagram of the feedforward structure depicted in Fig. 5.12.

The desired setpoint for the in-cylinder AFR value $\lambda_{cyl,set}$ is the input to the nonlinear feedforward controller and the absolute control signal of the EGR valve is the output. Moreover, the model depends on other quantities; some of them are measured by the ECU, namely N_e, $\dot{m}_f$, and T_{ic}, while the signals T_{im}, p_{im}, p_{em}, and T_{egr} are to be estimated.

Due to the fact that modern diesel engines contain a physical feedback loop, namely the exhaust gas recirculation, the direct dependencies of the feedforward controller on quantities measured within this loop are to be limited for preventing the feedforward controller from destabilizing the feedback loop. In order to reduce these dependencies, the remaining signals are read from static maps that have been measured previously.

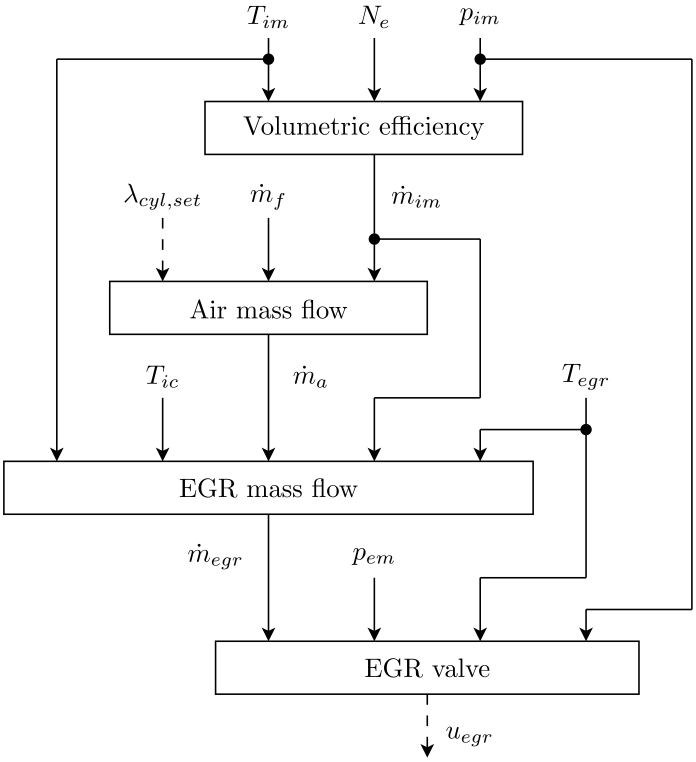
T_{im}
N_e
p_{im}
Volumetric efficiency
$\lambda_{cyl,set}$
$\dot{m}_f$
$\dot{m}_{im}$
Air mass flow
T_{ic}
$\dot{m}_a$
T_{egr}
EGR mass flow
$\dot{m}_{egr}$
p_{em}
EGR valve
u_{egr}

Figure 5.12: Causality diagram of the nonlinear feedforward controller.

Only the static realization of the controller is reported since a dynamic inversion of the plant, which was also tested, led to a more complex system but did not improve the control quality. The equations contained in the blocks depicted in Fig. 5.12 are described in detail below.

The block “volumetric efficiency” contains Eq. 4.61.

For the sake of representation (in order to avoid to report a very long mathematical expression) a simplified version of Eq. 4.27 is used for determining the amount of fresh air in the block “air mass flow”. However, for the realization of the nonlinear feedforward controller, the exact version of Eq. 4.27 was used.

Under the assumption that the AFR does not deviate too much from the stoichiometric value $\lambda \approx 1$ (which is unfortunately mostly not true in diesel engines), the following simplification

$$\frac{1}{\lambda} \approx 1 - (\lambda - 1) = 2 - \lambda \tag{5.11}$$

can be applied to Eq. 4.27, that becomes

$$\lambda(k) \approx \frac{(\dot{m}_a + \dot{m}_f)\lambda_{fc} + \dot{m}_{rg}\lambda_{rg} + \dot{m}_{egr}\lambda_{egr}}{\dot{m}_a + \dot{m}_f + \dot{m}_{rg} + \dot{m}_{egr}} \,. \tag{5.12}$$

Expressing the EGR mass flow in steady-state conditions as

$$\dot{m}_{egr} = \dot{m}_{im} - \dot{m}_a \tag{5.13}$$

and combining Eq. 5.12 and Eq. 5.13, the required amount of fresh air can be calculated as

$$\dot{m}_a = \frac{1}{2} \cdot \left[\lambda_{cyl,set}(k-t) \cdot \dot{m}_f \sigma_0 - \dot{m}_f - 1\right] \cdot \sqrt{\chi} \,, \tag{5.14}$$

with

$$\begin{aligned}\chi = \dot{m}_f \sigma_0 \cdot \Bigg\{ & 4\lambda_{cyl,set}(k) \cdot [\dot{m}_{im} + \dot{m}_{rg} + \dot{m}_f] \\ & -2\lambda_{cyl,set}(k-1) \cdot [2\dot{m}_{im} + 2\dot{m}_{rg} + \dot{m}_f] \\ & +\lambda^2_{cyl,set}(k-t) \cdot \dot{m}_f \sigma_0 + \frac{\dot{m}_f}{\sigma_0} \Bigg\} \,. \end{aligned} \tag{5.15}$$

Similarly, in the block “EGR mass flow”, the necessary amount of recirculated exhaust gases for achieving the desired AFR is calculated from the steady-state expression of Eq. 4.32 for p_{im}, namely

$$\dot{m}_{egr} = \frac{1}{c_p T_{egr}} \left[c_p T_{im} \dot{m}_{im} - c_p T_{ic} \dot{m}_a\right] \,. \tag{5.16}$$

The block “EGR valve” inverts the model of the EGR valve, i.e., it calculates the valve control signal necessary for obtaining a determined EGR mass flow. First, the required opening area is calculated from Eq. 4.9, as

$$A_{egr} = \dot{m}_{egr} \frac{\sqrt{R T_{egr}}}{p_{em}} \cdot \left(2\,\frac{p_{im}}{p_{em}} \left[1 - \frac{p_{im}}{p_{em}}\right] \right)^{-1/2} \,, \tag{5.17}$$

second, the EGR valve position, and thus the control signal u_{egr}, is determined by inverting the characteristic function depicted in Fig. 4.3.

5.5.2 Disturbance Compensator

A sudden acceleration, i.e., a fast rising of the injected fuel quantity, can be considered as a measured disturbance. With the measured air mass flow $\dot{m}_{hfm}$, a simplified estimation (only static) of the AFR in the cylinder $\lambda_{cyl,est}$ can be calculated as

$$\lambda_{cyl,est} = \frac{\dot{m}_{hfm}}{\dot{m}_f \sigma_0} \,. \tag{5.18}$$

The correction signal $\Delta u_{egr,dc}$ for the compensation of the disturbance is thus calculated as

$$\Delta u_{egr,dc} = \frac{\lambda_{cyl,set} - \lambda_{cyl,est}}{\hat{K}_{11}} \,. \tag{5.19}$$

5.5.3 Simulation with the Feedforward Controllers

The two feedforward controllers are investigated (arbitrarily) in combination with the IMC structure. The results of the simulations are shown in Fig. 5.13.

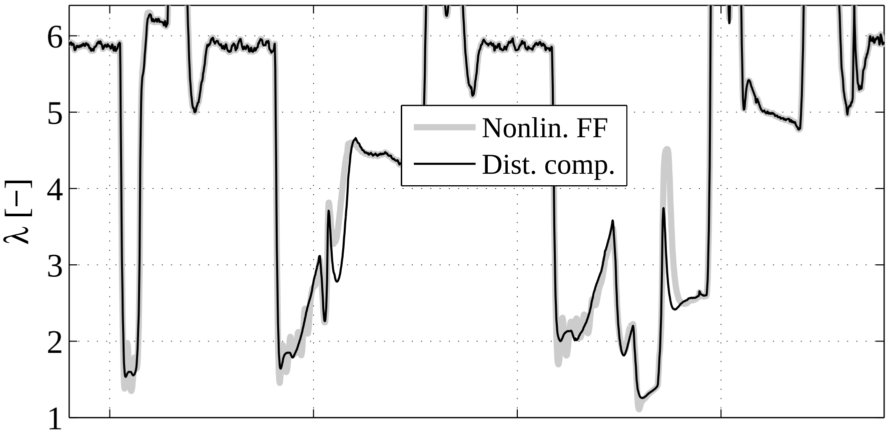

Figure 5.13: Simulation of the IMC controller with the nonlinear feedforward controller and the disturbance compensator.

As expected, the nonlinear feedforward element interferes with the feedback loop, causing undesired system oscillations that occur at low AFR values in particular, where an accurate control is most important.

The disturbance compensator, with its simple structure, is more reliable and provides better results than the more complex nonlinear feedforward controller. Therefore, this element is adopted during the experiments on the test-bench engine in both the IMC and the H_∞ control loops.

5.6 Experimental Results

The environment considered for the test of the AFR controllers presented in this section is the European driving cycle MEVG-95. The configuration of the system for both controllers designed with the two methods is depicted in Fig. 5.14.

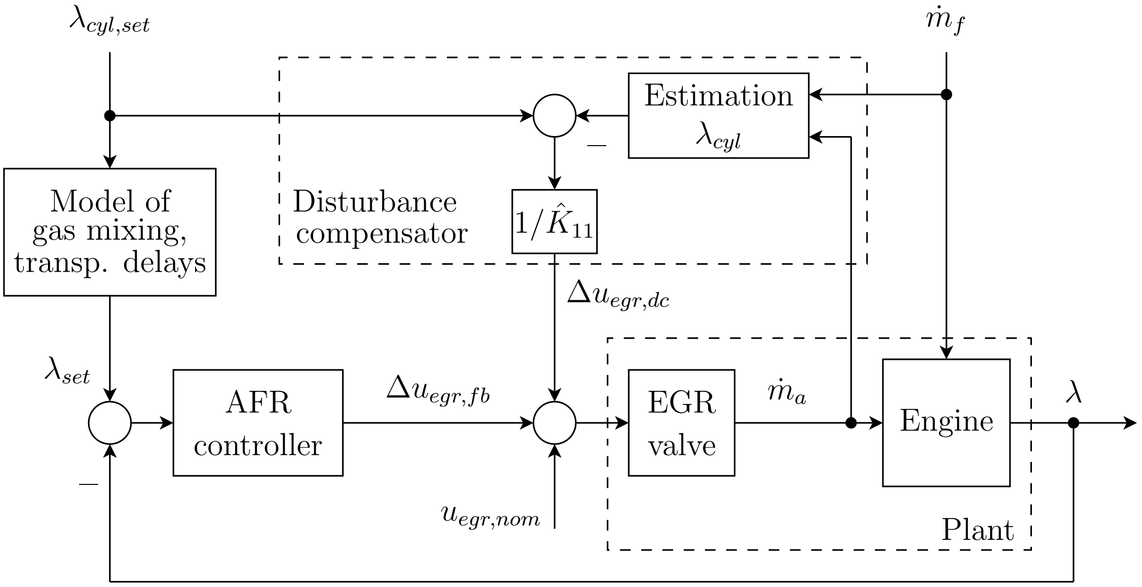
$\lambda_{cyl,set}$
$\dot{m}_f$
Estimation λ_{cyl}
$-$
Model of gas mixing, transp. delays
Disturbance compensator
$1/\hat{K}_{11}$
$\Delta u_{egr,dc}$
λ_{set}
AFR controller
$\Delta u_{egr,fb}$
EGR valve
$\dot{m}_a$
Engine
λ
$-$
$u_{egr,nom}$
Plant

Figure 5.14: Configuration of the feedback control system with disturbance compensation.

In order to prevent the feedback controller from counteracting the feedforward element, the setpoint $\lambda_{cyl,set}$ for the feedback loop is synchronized with the signal measured by the AFR sensor. For this scope, the setpoint is filtered by the dynamics of the AFR sensor and shifted by the transport delay from the cylinder output to the sensor. This configuration is particularly well suited during fast accelerations, when the lack of fresh air caused by the slower turbocharger dynamics with respect to those of the fuel path has to be compensated. In this case a higher AFR is forced by closing the EGR valve, thus reducing the amount of PM generated.

The AFR setpoints are read from a static map with the independent variables N_e and BMEP. The values contained in this map are derived from steady-state measurements of the standard engine.

The tracking performance of the two AFR controllers is compared on the test bench to that of the conventional EGR controller (which is open-loop for the AFR), as shown in Fig. 5.15. A wide range of AFRs is covered by the engine during the cycle, from an AFR value of about 1.2 up to 11. Considering transients, the emphasis is placed on the fast accelerations rather than decelerations, because the largest amount of PM is generated at low AFR values.

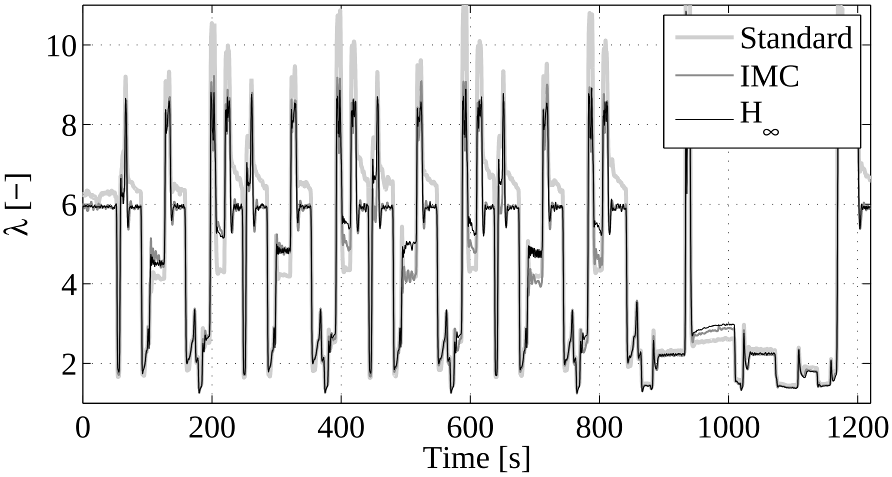

Figure 5.15: Comparison of the controllers during setpoint tracking.

For a better illustration of the results, a zoom in the urban part of the MEVG-95 is reported and commented below. The engine speed and the load profiles of that part of the driving cycle are depicted in Fig. 5.16.

Figure 5.17 shows the tracking of the AFR setpoint with the different controller configurations. It can be observed that the tracking performance of the two AFR controllers is almost equivalent and at least match that of the standard EGR controller, in spite of the large time delays in the new feedback loops.

For the IMC structure, the value $\sigma = 1$ is used for almost the entire operating range, except at low loads, where large AFR values are mea-

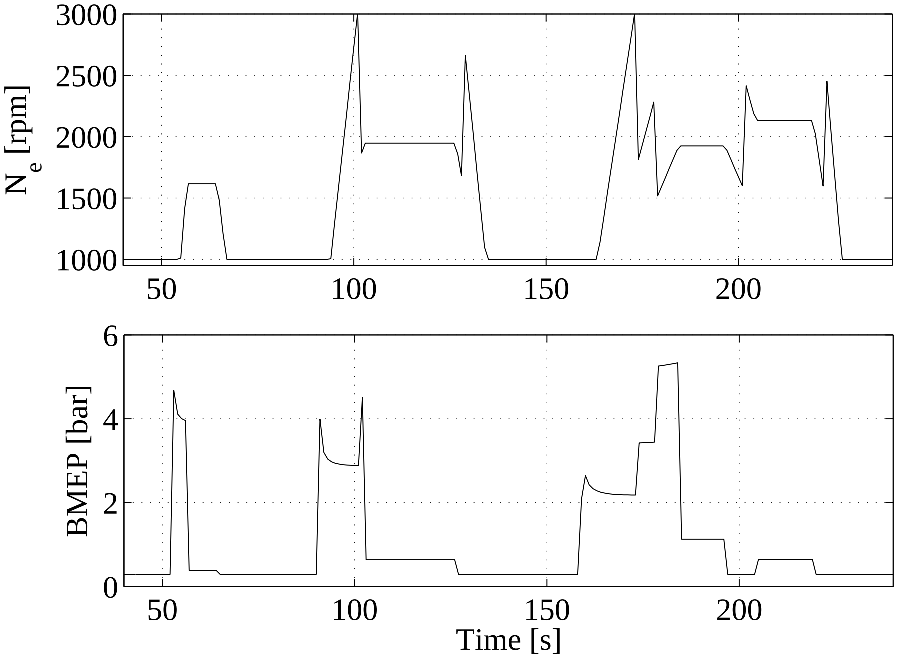

Figure 5.16: Urban part of the MEVG-95 driving cycle.

sured. In those operating points a smaller value of σ is chosen in order to reduce the bandwidth of the controller and thus to avoid the amplification of measurement noise.

Some differences in the AFR curves depicted in Fig. 5.17 are visible between the standard and the AFR-controlled engine. The main factor for these discrepancies is that the interpolation of the setpoints for the AFR controller is not made with the same grid points as it is made for the desired air mass in the ECU of the standard engine. Therefore, especially at low engine loads where the gradient in the map of the AFR setpoints is relatively large, a lower accuracy of the linear interpolation can result. Another reason for these differences is that the feedback of the standard EGR controller is based only on data measured before combustion takes place, and thus, drifts of the HFM sensor or an incorrect injection of the fuel mass are not measurable and cannot be compensated by the standard EGR controller.

Of course, the EGR actuator has a limited action only. Therefore, infeasible setpoints can occur, for instance, in the case of too large a drift of the HFM sensor or of the injectors.

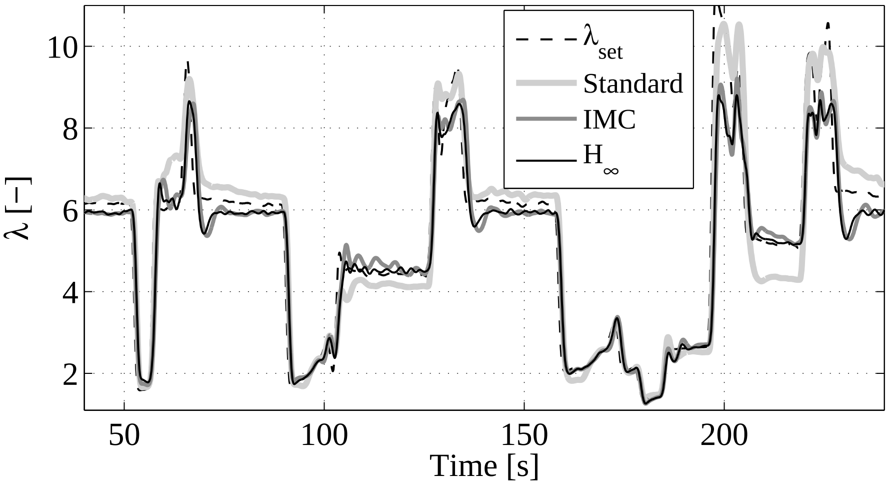

Figure 5.17: Comparison of the controllers during setpoint tracking (zoom on the urban part of the MEVG-95).

Chapter 6

MIMO Emissions Controller

In this chapter a multivariable emissions feedback controller is proposed for the NO_x emissions and for the AFR. The control inputs are the command signal of the EGR valve u_{egr} and the start of injection SOI.

Since the results obtained with the AFR controller proposed in Chap. 5 demonstrated that the approach based on a simplified model of the plant and on a simple control structure works well, this approach is extended to the multivariable case.

The multivariable controller consists thus of two independent IMC control-loops (that are based on the simplified plants p_{11} and p_{22}, respectively) designed according to the procedure described in Sec. 5.2, and connected by the decoupling term defined by Eqs. 3.8 and 3.9. The parameters of this controller are generated automatically in order to reduce the efforts of calibrating the control system in the entire operating range of the engine. The complete structure of the control system, including the disturbance compensator for the AFR control loop (see Sec. 5.5.2) and the static feedforward for the NO_x control loop, based on the nominal values calculated by the ECU, is depicted in Fig. 6.1.

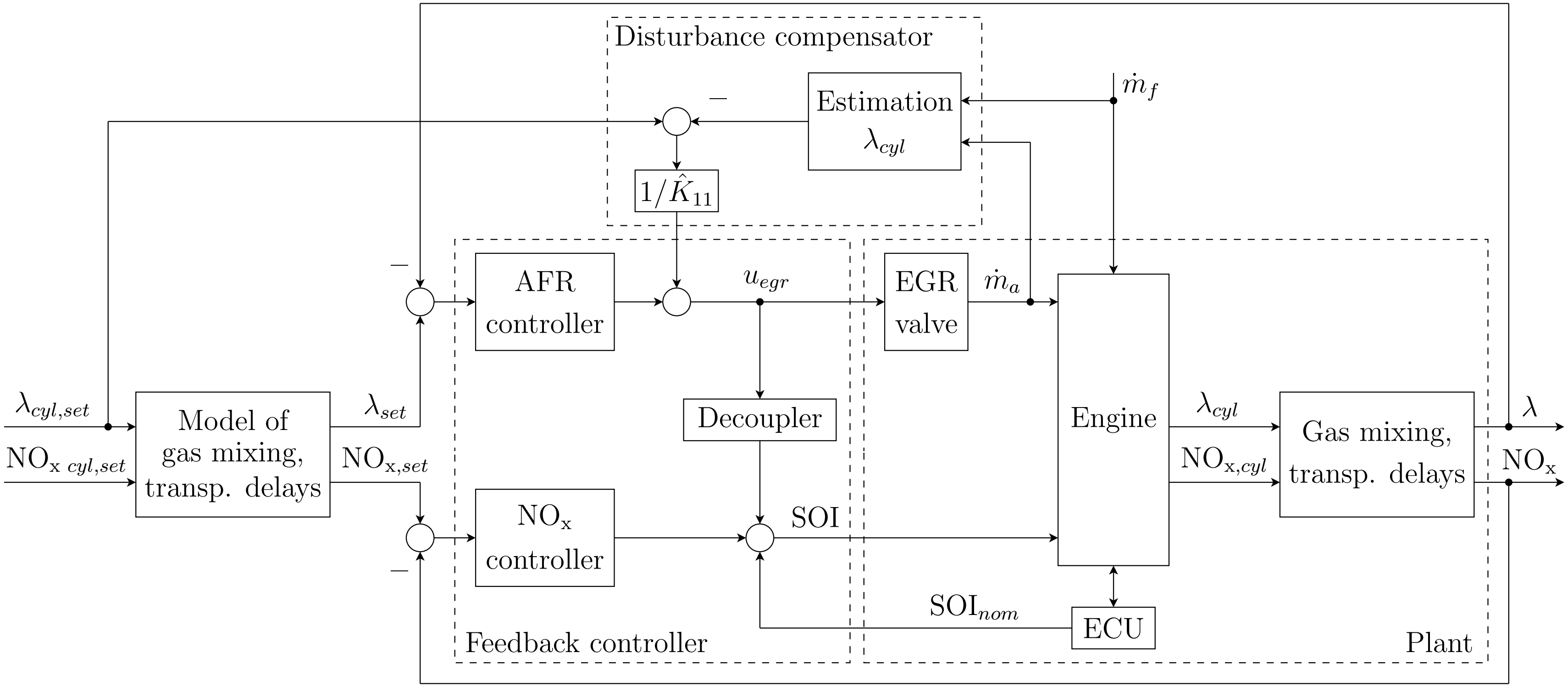
Disturbance compensator
Estimation
λ_{cyl}
$\dot{m}_f$
$-$
$1/\hat{K}_{11}$
$-$
AFR
controller
u_{egr}
EGR
valve
$\dot{m}_a$
Engine
$\lambda_{cyl,set}$
$\mathrm{NO_x}\ _{cyl,set}$
Model of
gas mixing,
transp. delays
λ_{set}
$\mathrm{NO}_{\mathrm{x},set}$
Decoupler
λ_{cyl}
$\mathrm{NO}_{\mathrm{x},cyl}$
Gas mixing,
transp. delays
λ
$\mathrm{NO_x}$
$\mathrm{NO_x}$
controller
SOI
$-$
SOI_{nom}
ECU
Feedback controller
Plant

Figure 6.1: Complete structure of the emissions controller.

6.1 Analysis of the Plant

The structure of the multivariable IMC controller is defined by the choice of the approximation model of the plant. As in the case of the AFR controller, the linearized engine model is used as a reference for approximating each of the three paths with a first-order low-pass element with a time delay term as in Eq. 3.5. The identification of the plant parameters is carried out by comparing the step response of the reference and target systems. The parameters are then stored in static maps with the independent variables BMEP p_{me} and engine speed N_e.

The parameters of the path $p_{11}(s)$ have been depicted in Figs. 5.1–5.3. Those of the remaining two paths, namely $p_{21}(s)$ and $p_{22}(s)$, are shown in Figs. 6.2–6.4 and Figs. 6.5–6.7, respectively.

It can be observed that the time constants and the delays of the paths $p_{21}(s)$ and $p_{22}(s)$ are very large. This is mainly due to the slow response time of the NO_x sensor.

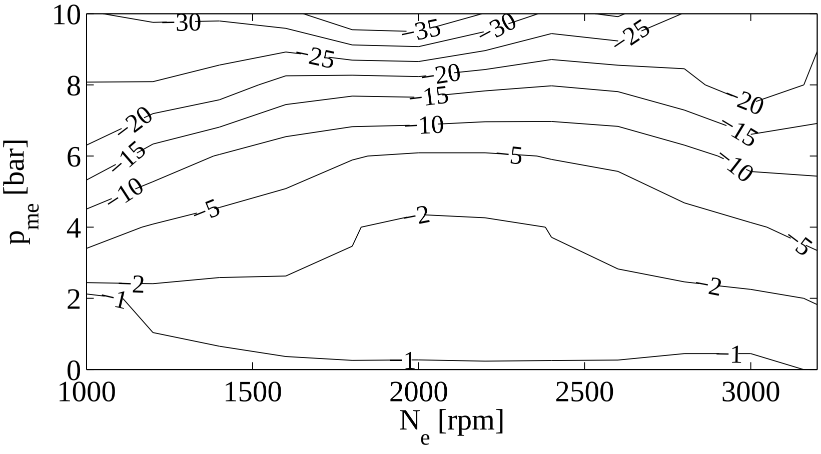

Figure 6.2: Map of $\hat{K}_{21}$ in [ppm/%].

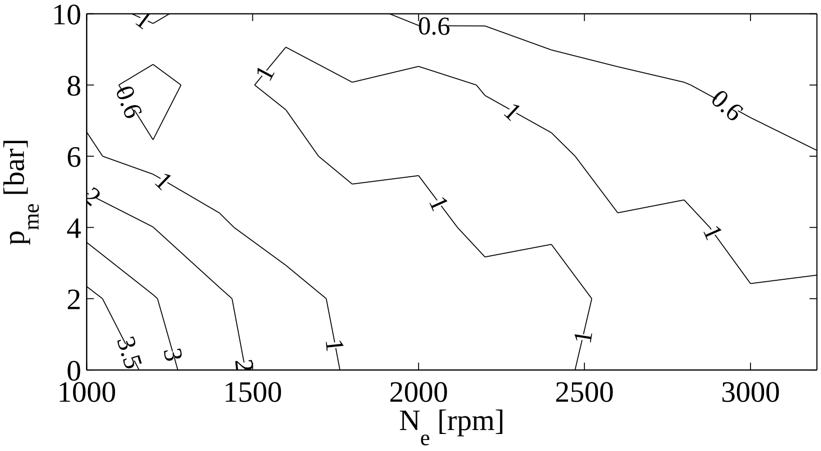

Figure 6.3: Map of $\hat{\tau}_{21}$ in [s].

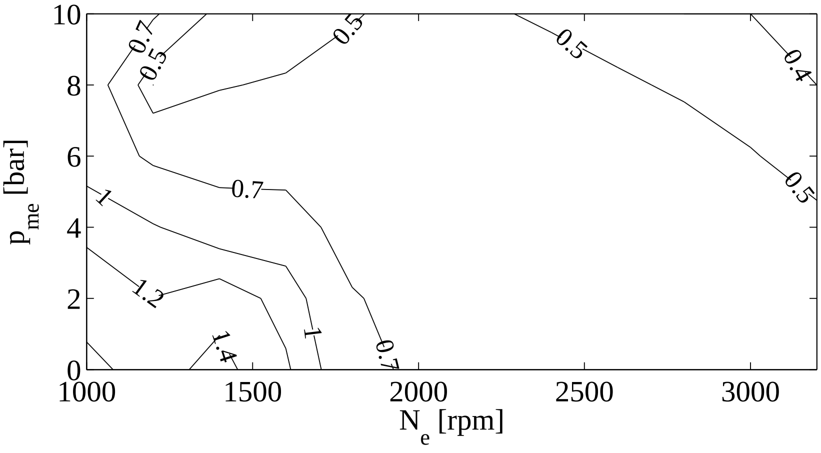

Figure 6.4: Map of $\hat{T}_{d,21}$ in [s].

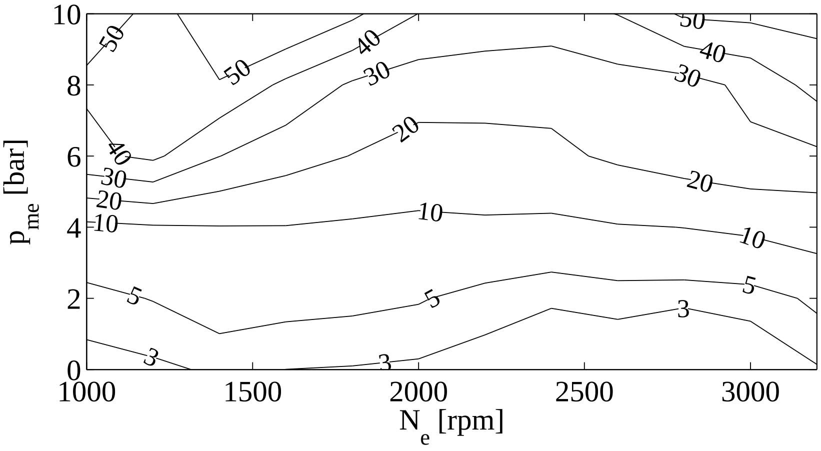

Figure 6.5: Map of $\hat{K}_{22}$ in [ppm/°CA].

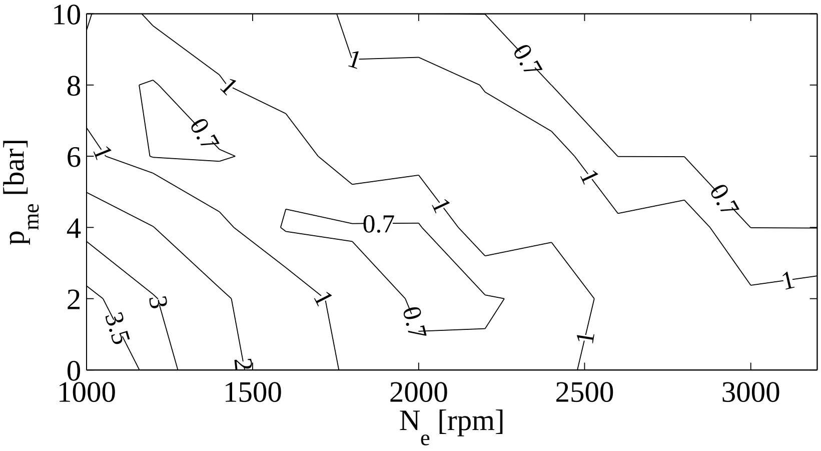

Figure 6.6: Map of $\hat{\tau}_{22}$ in [s].

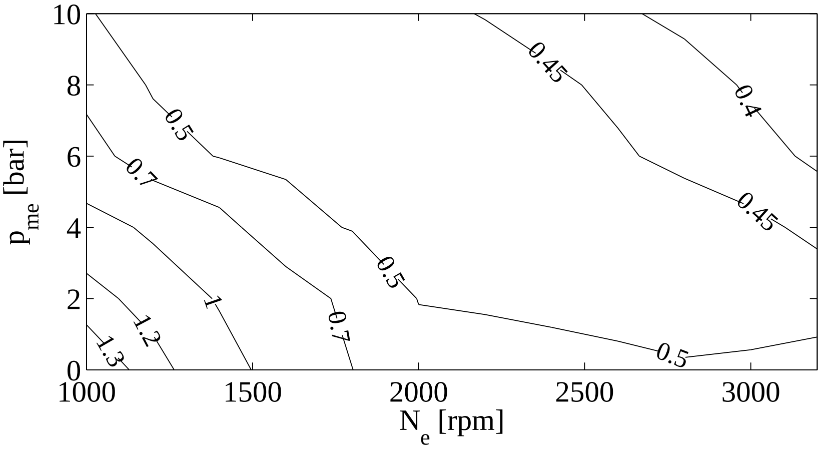

Figure 6.7: Map of $\hat{T}_{d,22}$ in [s].

6.2 Robustness Analysis

The two independent SISO control loops for the AFR and for the NO_x channels, if considered separately, each possess a phase margin of about $\varphi = 60°$ (see Fig. 5.11 in the case of the AFR system). However, by connecting the two control loops with the decoupling element, the robustness of the resulting multivariable control system is not guaranteed and, therefore, must be verified.

The robustness of a control system, consisting of a controller $C(s)$ and of a plant $P(s)$, can be quantified using its minimum return difference μ, defined as

$$\mu = \min_{\omega}\{\sigma_{min}\{F(j\omega)\}\}\,, \tag{6.1}$$

where σ_{min} is the minimum singular value and $F(s)$ is the return difference of the system

$$F(s) = I + L(s) = I + C(s)P(s)\,. \tag{6.2}$$

Comparing the singular values of $F(s)$ depicted in Fig. 6.8 for the SISO and MIMO cases, it can be observed that the robustness of the MIMO system is not compromised. A value of $\mu \geq -3$ dB is guaranteed.

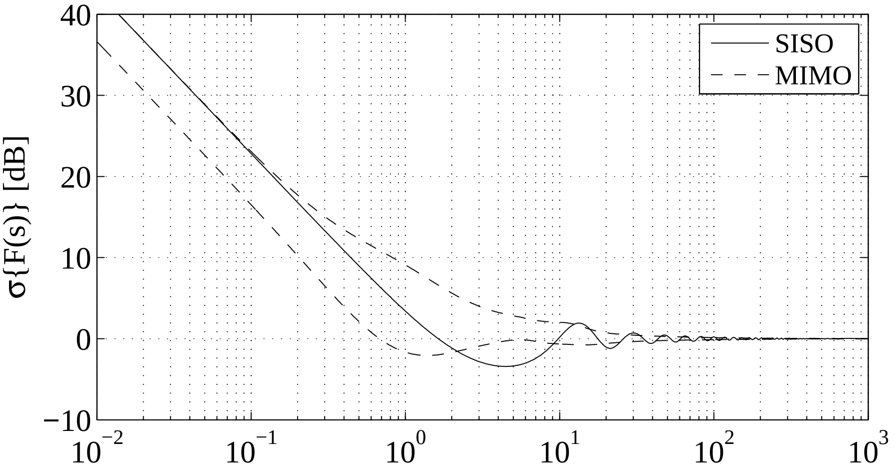

Figure 6.8: Singular values of the return difference $F(s)$ of the control system in one representative operating point.

6.3 Experimental Results

In this section different tests are carried out in order to demonstrate the validity and the feasibility of the proposed control structure, namely: 1) The effectiveness of the multivariable controller, in particular its decoupling capability, and the disturbance compensator are tested during a step between two operating points; 2) the tracking performance and the stability of the gain-scheduled controller are investigated during the MEVG-95 driving cycle; and 3) the ability of the emissions controller is investigated to keep a desired NO_x-PM point even in the case of drift of some sensors.

During the experiments described above, the setpoints for the AFR and for the NO_x emissions are read from static maps which are derived from steady-state measurements of the standard engine.

6.3.1 Step Between Two Operating Points

The test consists of a load step between 4.2 and 6.5 bar BMEP at a constant engine speed (2200 rpm), i.e., a typical acceleration. This test is chosen as representative, since it is in the middle of the range of operating points of interest.

In order to quantify the benefits of using a disturbance compensator and a decoupler for the two channels of the feedback controller, various configurations of the multivariable IMC controller are investigated. These configurations are: a) with a decoupler but without a disturbance compensator; b) without a decoupler but with a disturbance compensator; and c) with both a decoupler and a disturbance compensator. The results obtained with the standard controller (which is open-loop for the emissions) are shown for reference.

The results of these tests are depicted in Figs. 6.9 and 6.10, where the NO_x concentration is measured with a fast gas analyzer (Cambustion fNOx400, response time approximately 50 ms) only for validating the performance of the controller, rather than with the slow NO_x sensor used in the control loop, while the AFR is measured with a wide-range oxygen sensor.

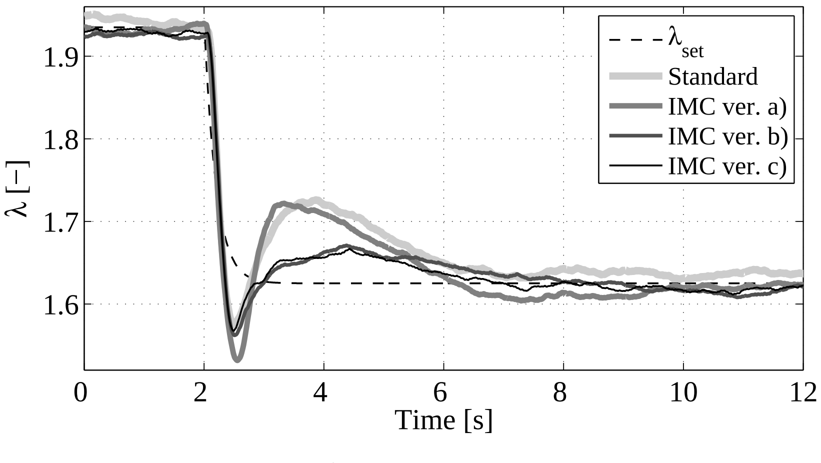

Figure 6.9: Trajectory of λ during a step in the engine load.

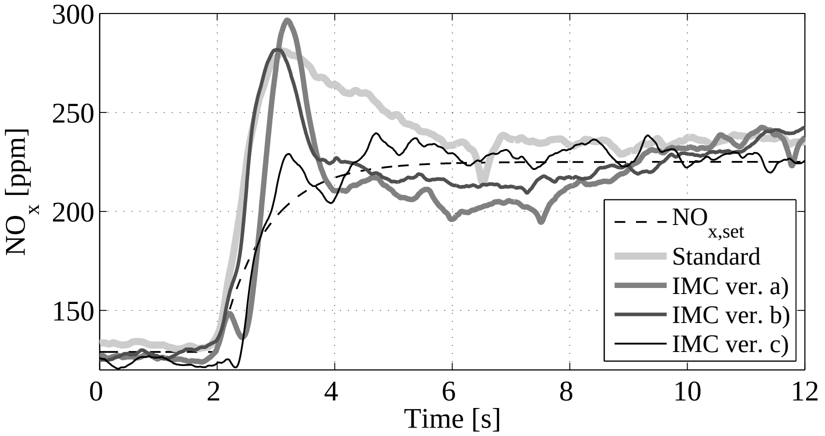

Figure 6.10: Trajectory of NO_x during a step in the engine load.

As expected, the results show that for achieving the best tracking performance during transient operations it is necessary to use both the decoupler and the disturbance compensator. The latter plays an important role for tracking the AFR during fast accelerations, avoiding excessively small values of the AFR and thus high PM peaks. At the same time, the decoupler prevents the formation of NO_x spikes caused by the temporary low EGR rates (the EGR control signal is depicted in Fig. 6.11) by retarding the injection timing (Fig. 6.12). In fact, with the adoption of the decoupler matrix D, the "disturbance" caused on the NO_x channel by the commanded AFR step is predicted and preventively compensated by the SOI control loop. However, in this figure it can be observed that the good decoupling realized with the IMC version c) is achieved by varying extremely the SOI, which would be hardly acceptable in a standard-production engine since the driveability would be affected negatively (see Fig. 6.13). Therefore, a compromise has to be found between the quality of the transient of the torque and that of the decoupling of the NO_x channel. With the control approach proposed here, any solution within the range comprised between version b) and version c) can be achieved.

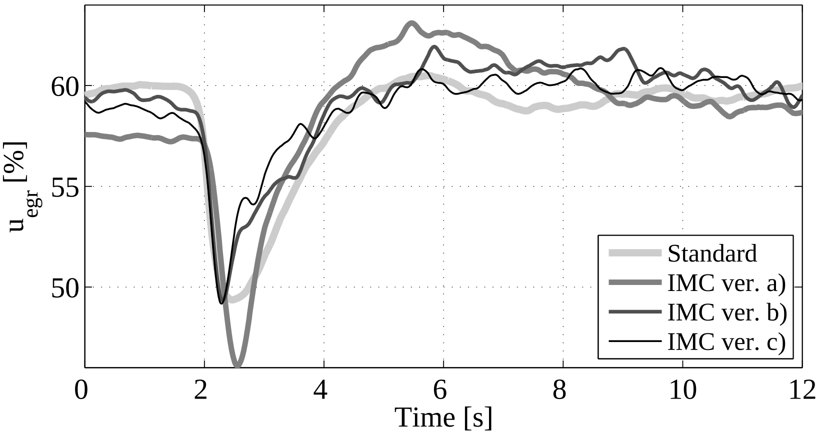

Figure 6.11: Trajectory of u_{egr} during a step in the engine load.

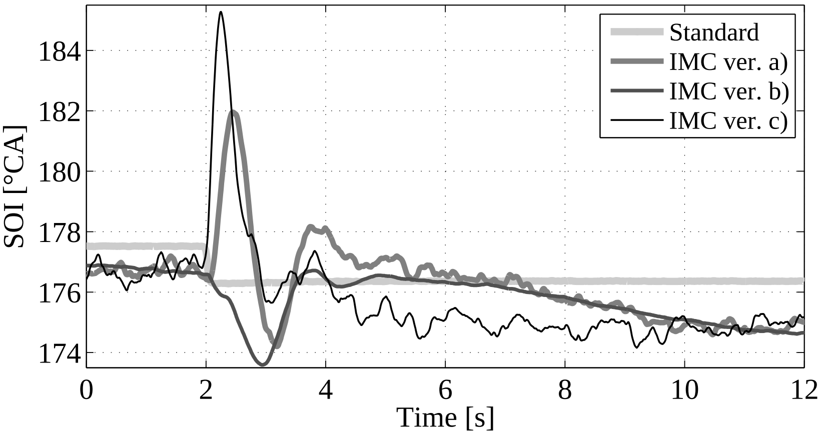

Figure 6.12: Trajectory of SOI during a step in the engine load.

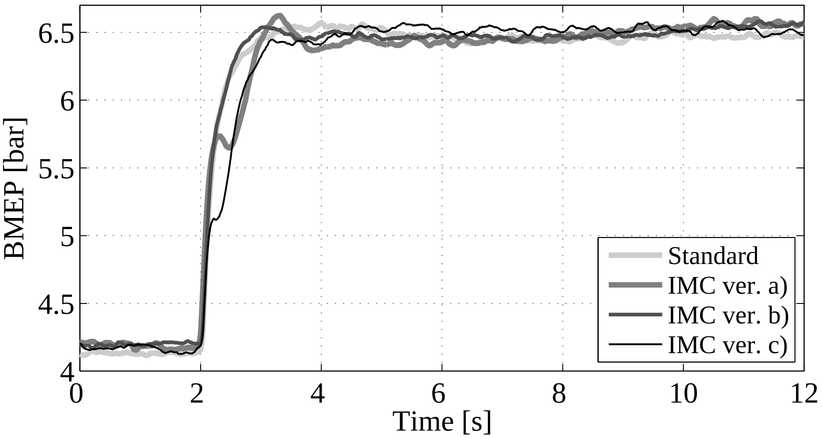

Figure 6.13: Trajectory of BMEP during a step in the engine load.

In Fig. 6.9, the overshooting of the AFR between 3 and 6 s correlates well with the dynamics of the boost pressure shown in Fig. 6.14. This fact suggests that the cross-coupling between the VGT and the emissions formation should be considered in the multivariable emissions controller for future improvements of the tracking performance. However, considering this coupling would not reduce the spikes of lower AFR values responsible for most of the PM production.

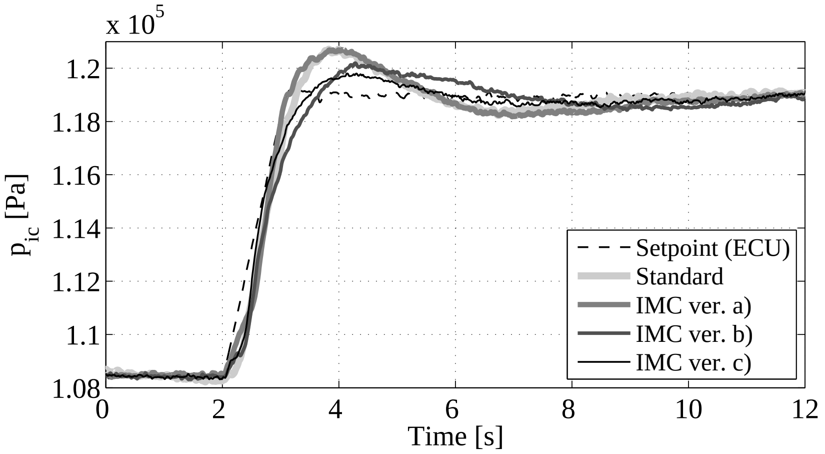

Figure 6.14: Trajectory of p_{ic} during a step in the engine load.

6.3.2 Setpoint Tracking during a Driving Cycle

The objective of this test is to demonstrate the validity of the proposed control structure, as well as the stability of the scheduled system under real operating conditions. Moreover, the capability of tracking the AFR and NO_x setpoints is examined.

This test is carried out under nominal operating conditions, and the IMC controller version c) is adopted. The instantaneous setpoints for the AFR and for the NO_x are read from static maps which are derived from steady-state measurements of the conventionally driven engine. A comparison between the standard and the emissions-controlled engine during a part of the European driving cycle is depicted in Figs. 6.15 and 6.16.

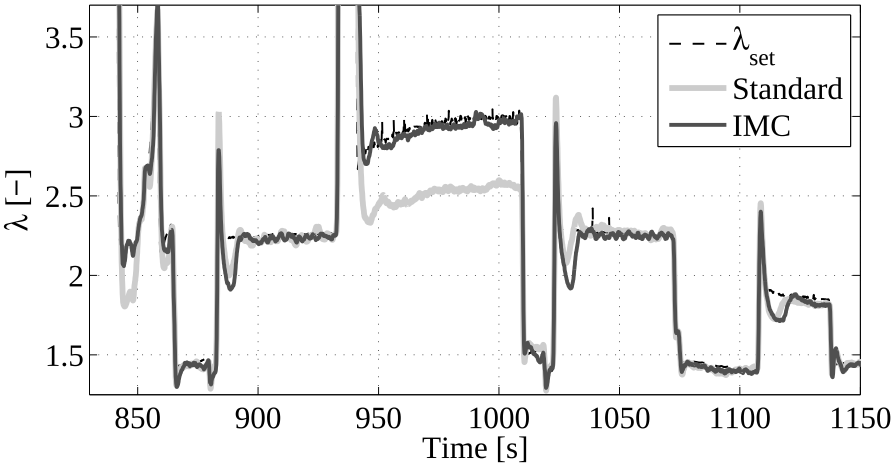

Figure 6.15: Comparison of the λ setpoint tracking of the controllers.

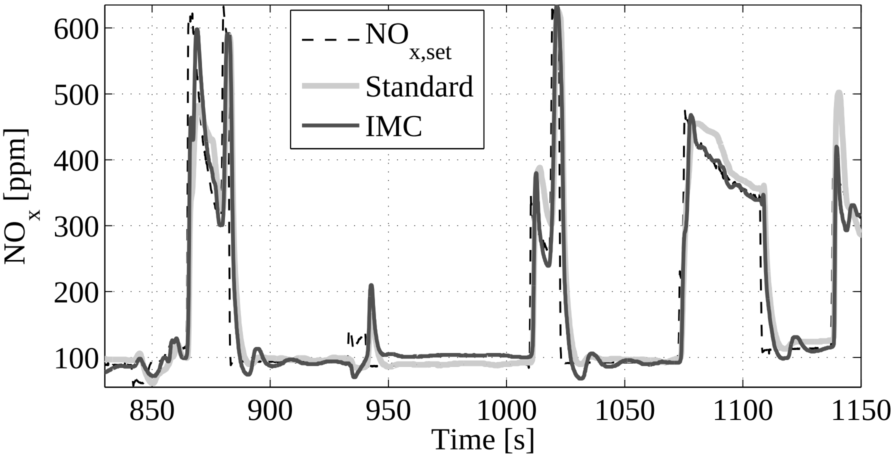

Figure 6.16: Comparison of the NO_x setpoint tracking of the controllers.

The results of this experiment, aside from the validity and the stability of the algorithm, evidence its limitations as well. For instance, taking a look at the two figures between 950 and 1000 s, due to the low accuracy of the setpoint interpolation, the AFR is set too high and thus low EGR rates occur. Since the action of the emissions controller has been limited on the SOI signal by $\pm 5°$ CA from the original setpoint supplied by the ECU, it is not possible, with the SOI control signal only, to fully compensate for the NO_x error during this time interval and, therefore, the setpoint cannot be held. This restriction on the SOI has been adopted in order to limit torque and acoustic noise variations from the nominal conditions.

6.3.3 Range of Uncertainty and Sensor Drifts

The results reported in this section have the goal to demonstrate the capability of the emissions-controlled engine to operate in a small range of uncertainty from a distinct NO_x-PM design point during a defined driving cycle, under nominal operating conditions as well as in the case of sensor drifts.

In this work, the NO_x and the AFR sensors are assumed ideal even if, in reality, they are affected by measuring tolerance and drift. However, the adoption of these new sensors offers some advantages with respect to the standard engine configuration: 1) A higher accuracy is achieved by measuring the NO_x concentration directly, instead of estimating it from the air mass measured at the engine inlet. In fact, an error of 1% in the air-mass measurement can lead to an error of up to 8% in the NO_x concentration; and 2) assuming that the HFM and the AFR sensor have the same measuring tolerance, the adoption of an AFR sensor, in addition, provides information about the injected fuel quantity.

The most important sensors and actuators, whose incorrect functioning would have a negative influence on the emissions formation, are the HFM, the boost-pressure sensor, and the fuel injectors. Therefore, the driving cycle MEVG-95 has been repeated on the engine test bench under different conditions, with and without emissions controller, and artificial drifts in the HFM (±10%) and in the boost-pressure sensor (±5%) have been introduced. The results are shown in Fig. 6.17. The consequences of a drift in the injected fuel quantity is discussed briefly after the exposition of the experimental results.

During this sequence of ten experiments, the NO_x-PM point defined as “reference” has been achieved with the conventionally driven engine without any sensor or actuator drift.

As expected, the standard engine is not able to keep the desired NO_x and PM emissions while, in the same situation, the emissions-controlled engine is kept at the desired point, with the exception of one case (drift in the boost pressure) that is slightly misaligned. This can happen when the actuators saturate due to infeasible setpoints caused by too large a drift.

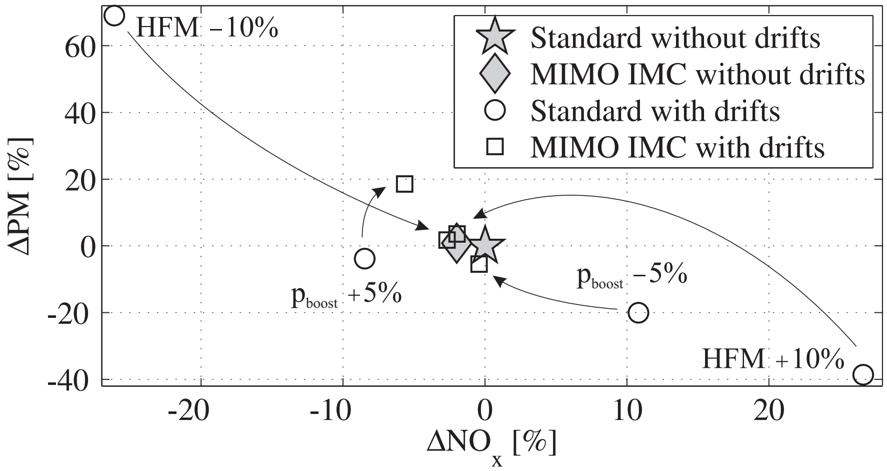

Figure 6.17: Variations from the designed NO_x-PM point in the case of drifts in the HFM and in the boost-pressure sensor.

In the case of a drift of the fuel injectors it cannot be guaranteed that the NO_x-PM point is maintained at the desired value by the emissions controller alone. Actually, the injected fuel mass, which is directly proportional to the BMEP, is one of the independent variables that define the operating point of the engine in the ECU. The other is the engine speed. If an incorrect fuel quantity is injected, the driver notices it and compensates this error with the accelerator. In this way, the ECU generates internally a value for the fuel mass that does not match the quantity effectively injected, causing the ECU to read from all the look-up tables (that are concerned by the fuel mass) quantities that do not correspond to the actual operating point, including the emissions setpoints.

With the adoption of an optional module able to detect faults in the fuel injection system as described in [55], for instance, it would be possible to keep the NO_x-PM point at the desired value even in the case of injectors drift. In fact, with such a diagnostic tool the injected fuel quantity used as an input signal for the ECU maps could be corrected accordingly, canceling the error.

Chapter 7

Setpoints Optimization

The compromises necessary for production engines to always keep the NO_x and PM emissions within the legislated limits (see Fig. 1.2) causes a new engine to be designed with a safety margin from the emissions legislation "box" of up to 30%. With this margin, the calibration engineers take into account all of the possible deteriorations that can occur during the entire lifetime of the engine. In this way, they ensure that this engine will always comply with the emissions legislation, but the result is a conservative design procedure and is not optimal in terms of fuel consumption.

The conventional EGR feedback loop controls the air mass, which (neglecting errors in the fuel injection) is equivalent to controling a desired AFR. The NO_x emissions *result* from the combination of all actual engine parameters and cannot be controlled independently of the AFR.

The emissions-controlled engine possesses one degree of freedom more than the standard engine, namely the SOI, and can thus control the NO_x emissions actively and almost independently of the AFR in each single operating point. It is possible to take advantage of this fact and influence the formation of NO_x in order to achieve lower fuel consumption levels.

7.1 Control Strategy

To reach the objective described above, a control strategy is proposed that increases (within the legislated limits, of course) the overall NO_x emissions during a defined driving cycle (Fig. 7.1), increasing in this way the thermal efficiency of the engine and thus reducing the fuel consumption. At the same time, due to the monotonically decreasing NO$_x$-PM tradeoff curve, this strategy leads to a minimization of the PM emissions as well.

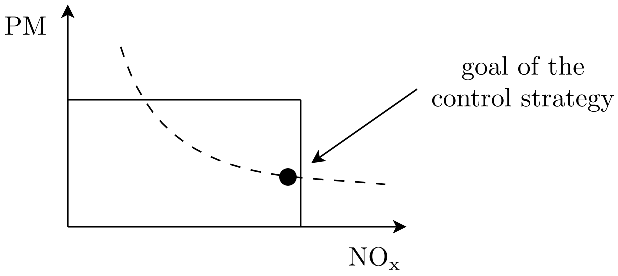

Figure 7.1: Control strategy based on the NO$_x$-PM tradeoff.

Of course, this strategy can only be followed if an emissions controller is used, that can compensate for manufacturing tolerances and engine ageing.

7.2 Formulation of the Problem

The optimization of the setpoint maps [11] for the AFR and for the NO$_x$ concentration has to be conducted in relation to a standard driving cycle. In this work, the European MEVG-95 is used as example, but the same procedure could be applied to other driving cycles.

The driving cycle defines the boundary conditions for the engine and provides information about the actual engine speed N_e and BMEP p_{me}. The setpoints are read from two two-dimensional maps with the independent variables N_e and p_{me}. The 72 elements of each map (6×12 matrices, cf. Fig. 4.22) are the parameters to be optimized.

The difficulty of solving this optimization problem is the fact that there are many parameters to be adjusted to achieve minimal fuel consumption while respecting the constraint (total NO$_x$ mass over the driving cycle) as depicted in Fig. 7.2. Considering all the possible combinations of varying the setpoint maps for the two quantities it becomes clear that, assuming that a unique solution exists, it is more probable to locate one of the many suboptimal solutions that lead to the same NO$_x$ target and to a locally minimal fuel consumption. A possible approach to increase the chance of finding a global optimum is to repeat the optimization many times by

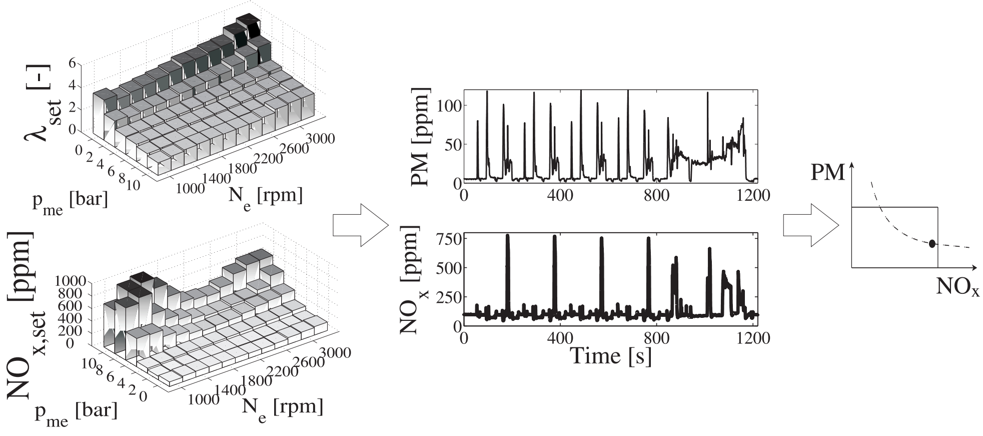

Figure 7.2: Optimization problem.

varying the starting values of the parameters to be optimized and checking whether the performance index achieved is always the same. This approach is investigated here even though, obviously, it does not guarantee that a global optimum can be found.

The optimization objective is expressed mathematically below. The performance index J for the minimization of the fuel consumption is given in Eq. 7.1. More precisely, the fuel variation $\Delta\dot{m}_f$ from the standard operating conditions of the engine is minimized. The entire cycle is considered for the integration, so that $t_0 = 0$ is the initial time and $t_1 = 1220$ s corresponds to the duration of the MEVG-95 cycle, in this case.

$$J = \int_{t_0}^{t_1} \Delta\dot{m}_{f,nom}\, dt \overset{!}{=} \min \tag{7.1}$$

The minimization of the PM is an implicit objective, since the PM are automatically reduced when NO_x is maximized, as discussed previously.

7.2.1 Fuel Consumption Model

For the numerical minimization of the performance index J, a fuel consumption model is required. Therefore, a simplified model has been developed that considers only variations from the conventionally driven engine, as shown in Fig. 7.3.

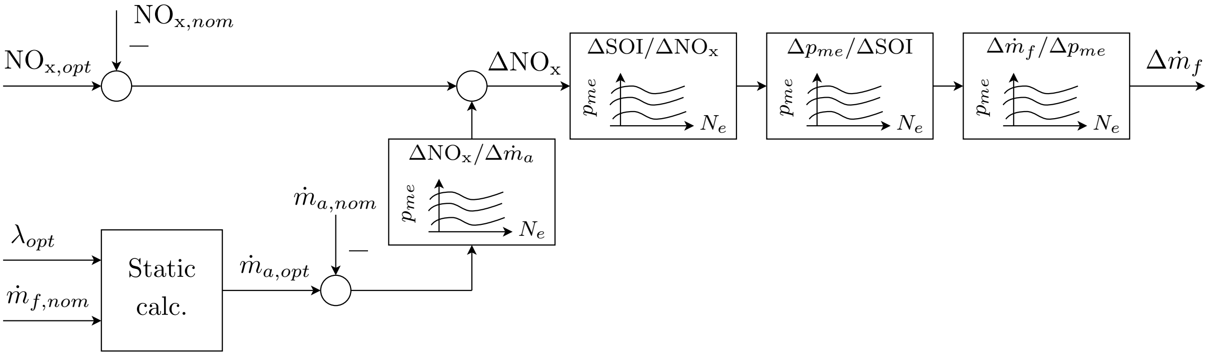

Figure 7.3: Fuel consumption model based on maps of the static gains.

The main assumption is that changes in the fuel consumption can be caused only by changes in the injection timing. This is reasonable since the SOI influences the combustion temperature, and thus the engine efficiency, the generated torque, and thus the fuel consumption. The input signals to the model are the differences $\Delta(.)$ between the optimized $(.)_{opt}$ and the nominal $(.)_{nom}$ setpoints, where the nominal values are obtained by steady-state measurements of the conventionally driven engine.

The static maps depicted in Fig. 7.3 contain the static gains calculated as byproducts of the control-oriented NO$_x$ model reported in [54]. The block called "Static calc." is represented by

$$\dot{m}_{a,opt} = \lambda_{opt} \cdot \dot{m}_{f,nom} \cdot \sigma_0 \,. \tag{7.2}$$

7.2.2 Calculation of the Overall NO$_x$ Mass

For the calculation of the total NO$_x$ mass m_{NOx} produced during the driving cycle

$$\begin{aligned} m_{NOx} &= \int_{t_0}^{t_1} \dot{m}_{NOx}\, dt \\ &= \int_{t_0}^{t_1} [NO_x] \cdot \dot{N}_{eg} \cdot M_{NOx} \cdot 10^{-6}\, dt \,, \end{aligned} \tag{7.3}$$

the concentration $[NO_x]$ measured in [ppm] has to be converted to a mass flow $\dot{m}_{NOx}$. The NO$_x$ molar mass M_{NOx} has been calculated assuming that NO_x consists of 15% NO and 85% NO_2. The molar flow $\dot{N}_{eg}$ of the exhaust gases can be estimated as

$$\dot{N}_{eg} = \frac{\dot{m}_{eg}}{M_{eg}}\,, \tag{7.4}$$

where $\dot{m}_{eg}$ is the exhaust gas mass flow, and its molar mass M_{eg} is determined from the combustion equation as a function of the actual AFR. With the assumption of a complete combustion according to [31], in the case of a $C_{14}H_{30}$ diesel type, the chemical reaction is described by Eq. 7.5. The fresh air composition is assumed to consist of 21% oxygen and 79% nitrogen.

$$\begin{aligned} &\frac{1}{21.5\lambda} \cdot C_{14}H_{30} + O_2 + \frac{79}{21} \cdot N_2 \\ &\qquad \rightarrow \alpha \cdot CO_2 + \beta \cdot H_2O + \gamma \cdot O_2 + \delta \cdot N_2 \end{aligned} \tag{7.5}$$

The coefficients of the stoichiometric balance are

$$\alpha = \frac{14}{21.5\lambda}\,, \quad \beta = \frac{15}{21.5\lambda}\,, \quad \gamma = 1 - \frac{1}{\lambda}\,, \quad \delta = \frac{79}{21}\,. \tag{7.6}$$

The molar fraction X_y of the elements in the exhaust gas, where $y = \alpha, \beta, \gamma, \delta$, is the ratio between the moles of the species y and the total number of moles in the exhaust gas, as

$$X_y = \frac{y}{\alpha + \beta + \gamma + \delta}\,. \tag{7.7}$$

Consequently, the molar mass of the exhaust gas is expressed as

$$\begin{aligned} M_{eg} = {} & X_\alpha \cdot (M_C + 2M_O) + X_\beta \cdot (2M_H + M_O) + \\ & + X_\gamma \cdot 2M_O + X_\delta \cdot 2M_N\,, \end{aligned} \tag{7.8}$$

where M_x are the molar masses of the corresponding elements.

7.3 Solution to the Problem

Considering each element of the look-up tables of the setpoints as one parameter to be optimized leads to a total of 144 parameters. This number can be reduced drastically if only the most important operating points are considered.

7.3.1 Analysis of the Driving Cycle

In order to determine the relevant operating points for the optimization, an analysis of the driving cycle (in this case the MEVG-95) is conducted in this section.

The frequency with which each operating point is driven during the test procedure has been determined, and the total time spent in each operating point during the driving cycle considered is depicted in Fig. 7.4 for the standard engine. It can be observed that about 40% of the operating points are not active during this driving cycle. The engine runs at idle most of the time and, in general, is driven at low speeds and low loads. However, this ranking does not yield information about the amount of pollutants generated.

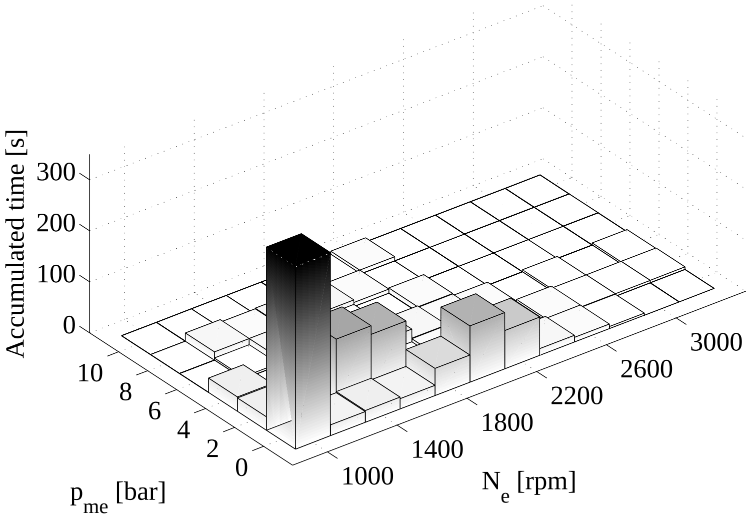

Figure 7.4: Accumulated time spent in every operating point.

Thus, the relevance of an operating point is classified by the amount of pollutant emissions produced in that point. The measured signals, i.e., the NO_x and the PM concentrations, have been corrected by inverting the dynamics of the exhaust gas measurement devices and removing the delay due to the mass transport in order to reconstruct the real emission values in the cylinder.

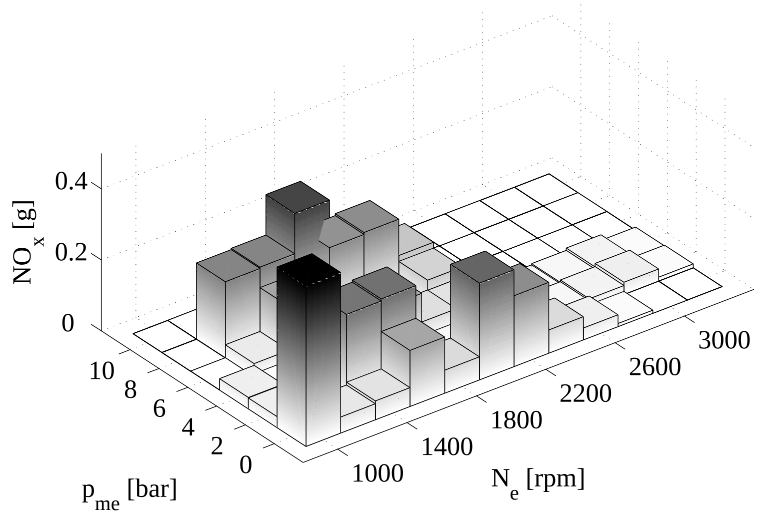

Figure 7.5: Accumulated NO_x mass.

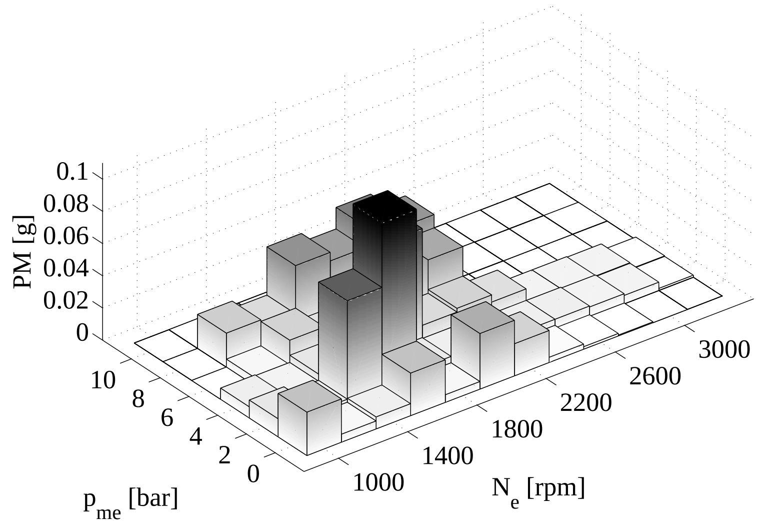

Figure 7.6: Accumulated PM mass.

The total mass of NO_x and PM emissions produced at every operating point are depicted in Figs. 7.5 and 7.6, respectively. Even if just a short time is spent in the operating points at high loads, these points are a big source of emissions. Also the accumulated fuel mass, as depicted in Fig. 7.7, correlates well with the production of NO_x.

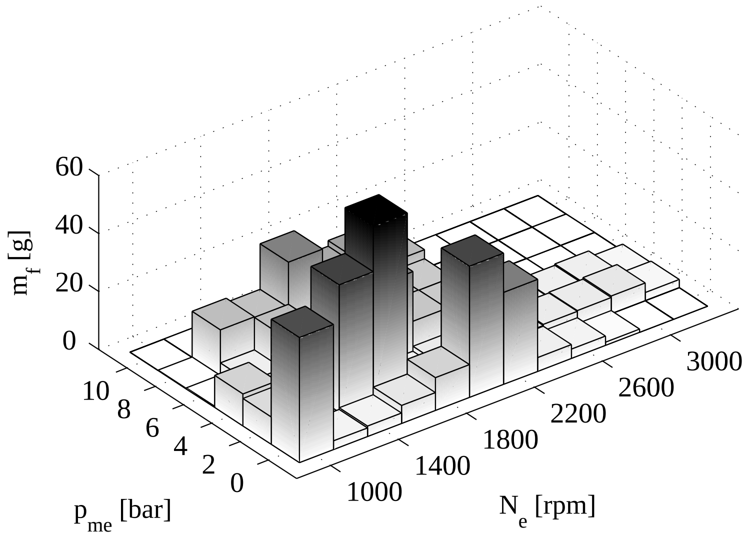

Figure 7.7: Accumulated fuel mass.

The results obtained above can be transformed and represented as the relative mass fraction that every operating point (OP) provides, as in Fig. 7.8. Actually, about 60% of the total amount of pollutants is generated in only eight operating points for every species, as listed in Table 7.1.

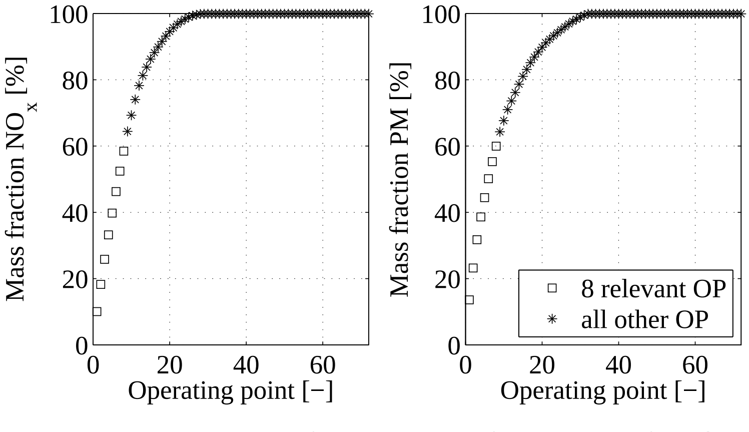

Figure 7.8: Distribution of the mass fraction of NO_x and PM.

Engine speed [rpm]	BMEP [bar]	NO_x	PM	m_f rank
1000	0	x	-	4
1200	8	x	-	11
1400	2	x	x	2
1400	8	x	-	13
1600	2	x	x	1
1600	8	x	x	7
1800	4	-	x	6
1800	8	-	x	9
2000	0	x	-	3
2000	8	x	x	8
2200	6	-	x	16
2200	8	-	x	10

Table 7.1: Relevant operating points.

Using these results, and considering that some of the eight operating points mentioned above are responsible for both the NO_x and PM production, the number of parameters for the optimization can be reduced “intelligently” by 92%, from 144 to 12.

7.3.2 Optimization with Constraints

The simulation of the complete nonlinear engine model with the parameterized emissions controller during an entire MVEG-95 takes about two minutes on a modern PC with a 3 GHz processor. Since a large number of iterations is required by the optimization routine and since the experiment is to be repeated several times with different initial conditions in order to ensure (with a large probability) that the result achieved is really a minimum, the system has been strongly simplified. It is assumed that the controlled system (emissions controller and nonlinear engine model) is so fast that it can follow instantaneously and exactly the actual AFR and NO_x setpoints. Under these assumptions the system can be considered as static and to consist essentially of the fuel consumption model only.

The NO_x target, i.e., the constraint for the optimization, is set 20% higher than in the conventionally driven engine, which represents approximatively the actual design safety margin necessary for production engines to always keep the NO_x and PM emissions within the legislated limits. In this way, it is possible to see the potential improvements that can be achieved with the new control strategy proposed here.

The starting values for the optimization of the AFR and NO_x setpoints are the steady-state measurements of the conventionally driven engine in each operating point considered. The optimization parameters cannot vary freely since the EGR-valve actuator is physically limited and too large variations of the injection timing would compromise the torque generated and thus the driveability of the engine. Therefore, constraints have to be placed on the parameters or, for the sake of simplicity, on the variation of the parameters from their nominal values. The nominal position of the actuators is known and the static gains of the AFR and NO_x on changes in the actuator positions can be determined from the linearized engine model. Therefore, with this information, an approximative and reasonable limit for the variation of each parameter is calculated. Moreover, due to the saturation of the actuators, in order to reach the defined NO_x target (with a certain reserve) by optimizing only the 12 parameters, the entire map of the NO_x setpoints has been augmented generally by 10% before starting the optimization. This amount has been chosen by rule of thumb, but it could be used as an additional parameter to be optimized.

7.3.3 Results of the Optimization

The variations of the setpoints after the optimization are depicted in Figs. 7.9 and 7.10. As expected, all the changes are strictly positive in both the AFR and the NO_x setpoints.

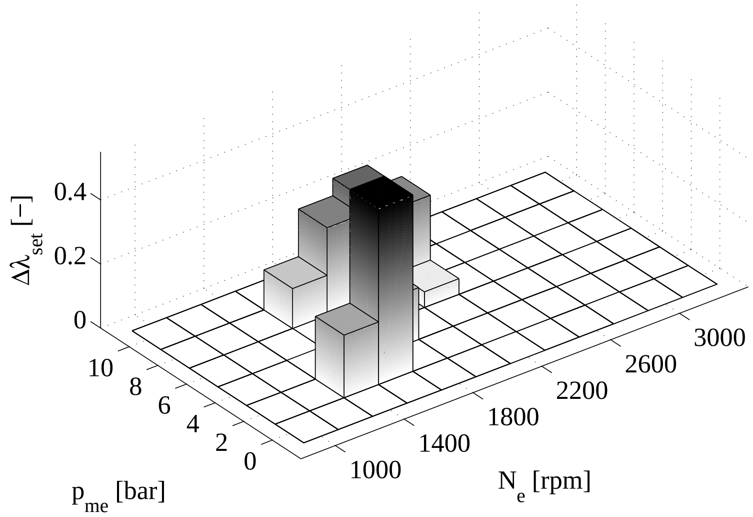

Figure 7.9: Variation of the AFR-setpoint map after the optimization.

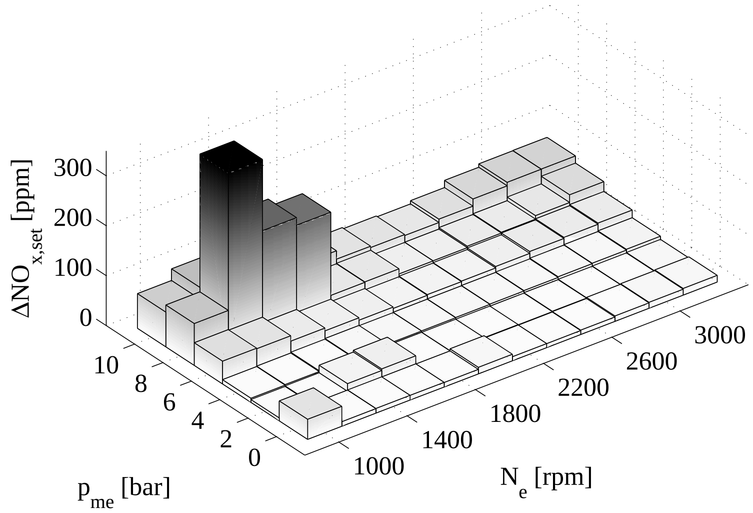

Figure 7.10: Variation of the NO_x-setpoint map after the optimization (including a +10% general offset).

7.4 Empirical Model for the PM

In order to quantify the advantages of using the proposed control strategy, a rudimentary empirical model for the prediction of the PM mass m_{PM} has been designed. The PM mass is calculated as in Eq. 7.9, where $\dot{N}_{eg}$ is the molar flow of the exhaust gases and M_{PM} is the molar mass of PM.

$$m_{PM} = \int_{t_0}^{t_1} \dot{m}_{PM}\, dt = \int_{t_0}^{t_1} [PM]\dot{N}_{eg} M_{PM}\, dt \tag{7.9}$$

The PM concentration $[PM]$ is read from a static look-up table that has the relative AFR and the engine speed as input signals, as

$$[PM] = f(\lambda, N_e)\,. \tag{7.10}$$

7.5 Experimental Results

The effectiveness of the control strategy proposed to minimize the fuel consumption is demonstrated experimentally on the test-bench engine. During the test, the setpoints for the emissions controller are used that have been optimized regarding the fuel consumption. Comparing the simulated data obtained with the methods described in this chapter with the experimental data measured on the test-bench engine as in Table 7.2, it can be observed that the measurements are in good agreement with the simulations.

The predefined theoretical $\mathrm{NO_x}$ target set to +20% has been confirmed by the measurements to be +17%. The amount of PM that are generated by the emissions-controlled engine with the optimized setpoints was roughly predicted to lie −9% below that of the conventionally driven engine while the measurements yielded −16%. This result is acceptable, considering the simplicity of the PM model. Even the static fuel consumption model provided good results with an estimation of −4.2% and a measurement of −3.4% of fuel necessary to drive the same test procedure as the standard engine with standard setpoints. The discrepancy of about 20% in the estimation of the fuel saving can be attributed to the approximation of the dynamic emissions-controlled engine system with a static model.

Quantity	Simulation	Measurement
$\mathrm{NO_x}$ mass (target)	+20%	+17%
PM mass	−9%	−16%
Fuel consumption	−4.2%	−3.4%

Table 7.2: Results of the setpoints optimization for the MEVG-95.

Chapter 8

Summary and Conclusions

In order to meet the increasingly restrictive legislation concerning the pollutant emissions of diesel passenger cars during the entire lifetime of the engines while taking into account engine wear, production tolerances, and drift of sensors and actuators, a novel approach for the closed-loop control of the $\mathrm{NO_x}$ and the particulate matter (PM) emissions is proposed. New on-board exhaust gas measurement devices are adopted and a multivariable emissions-feedback controller is designed for the $\mathrm{NO_x}$ emissions and for the air/fuel ratio (AFR), which is used as an indicator for the PM emissions. The controlled inputs are the command signal of the exhaust gas recirculation valve and the start of injection. In fact, besides the boost pressure that is regulated independently by the standard controller, those are the inputs that most significantly affect the formation of $\mathrm{NO_x}$ and PM emissions.

Although the investigation conducted in the scope of this thesis is only a first step towards fully emissions-controlled diesel engines, the results obtained with the new approach presented are encouraging. In fact, the dynamic tracking performance of the emissions setpoints and the driveability of the engine are at least as good as those attained by using the conventionally controlled engine. Moreover, besides the ability of such an emissions control system to operate the engine in a small range of uncertainty from a designed $\mathrm{NO_x}$-PM point even in the case the engine considered behaves in a different way than a nominal reference engine, the fuel consumption can be reduced substantially with the adoption of an adequate control strategy. The new control strategy proposes to increases the overall NO_x emissions during a defined driving cycle, within the legislated limits, increasing in this way the thermal efficiency of the engine and thus reducing the fuel consumption. At the same time, due to the monotonically decreasing NO_x-PM tradeoff curve, this strategy leads to a minimization of the PM emissions as well.

The development of the novel approach for the feedback control of the emissions of diesel engines presented in this thesis has been carried out taking into account its applicability on a standard-production engine. Considering that the memory and the computing power of an engine control unit are limited, the multivariable controller proposed consists of two independent internal model SISO control loops developed with a simplified model of the plant and connected with a decoupling term. Moreover, the steps required during the entire design process have been automated, namely:

- The calibration of the nonlinear model of the plant;
- The linearization of the nonlinear model around a grid of relevant operating points;
- The approximation of the paths of the high-order linear plant as a first-order model with a time delay element in each;
- The design and parametrization of a gain-scheduled controller with constant robustness over the entire operating range of the engine, in order to take into account for the different dynamics in the different operating conditions;
- The generation of the setpoints for the emissions controller, according to the control strategy proposed for minimizing the fuel consumption.

In this way, besides reducing the efforts to calibrate the control system, the results obtained in this work can be easily transferred to other engines.

References

[1] "Online information service on clean diesel engines and diesel emissions," 2008. [Online]. Available: www.dieselnet.com

[2] N. Abe and K. Yamanaka, "Smith predictor control as internal model control - A tutorial," in *SICE Annual Conference*, Fukui, Japan, August 2003.

[3] E. Alfieri, A. Amstutz, and L. Guzzella, "Gain-scheduled model-based feedback control of the air/fuel ratio in diesel engines," *Control Engineering Practice*, 2009, accepted for publication.

[4] E. Alfieri, A. Amstutz, C. H. Onder, and L. Guzzella, "Model-based feedback control of the air-to-fuel ratio in diesel engines based on an empirical model," in *Proceedings of the 2006 IEEE International Conference on Control Applications*, Munich, Germany, 2006, pp. 509–514.

[5] E. Alfieri, A. Amstutz, C. H. Onder, and L. Guzzella, "Automatic design and parametrization of a model-based controller applied to the AF-ratio control of a diesel engine," in *Proceedings of the IFAC Symposium on Advances in Automotive Control AAC07*, Monterey Coast, California, 2007, pp. 413–420.

[6] A. Amstutz and L. Del Re, "EGO sensor based robust output control of EGR in diesel engines," *IEEE Transactions on Control Systems Technology*, vol. 3, no. 1, pp. 39–48, 1995.

[7] P. Apkarian and P. Gahinet, "A convex characterization of gain-scheduled H_∞ controllers," *IEEE Transactions on Automatic Control*, vol. 40, no. 5, pp. 853–863, 1995.

[8] K. J. Åstrom, K. H. Johansson, and Q. G. Wang, "Design of decou-

pled PI controllers for two-by-two systems," in *IEEE Proceedings of Control Theory and Applications*, vol. 149, no. 1, 2002, pp. 74–81.

[9] H. D. Baehr, *Thermodynamik*, 8th ed. Springer-Verlag, 1992.

[10] D. Brand, "Control-oriented modeling of NO emissions of SI engines," Ph.D. dissertation, ETH Zurich, 2005.

[11] J. F. Cassidy, "A computerized on-line approach to calculating optimum engine calibrations." SAE paper 770078, 1977.

[12] J. Chauvin, G. Corde, N. Petit, and P. Rouchon, "Motion planning for experimental airpath control of a diesel homogeneous charge-compression ignition engine," *Control Engineering Practice*, vol. 16, no. 9, pp. 1081–1091, 2008.

[13] S. K. Chen and O. Yanakiev, "Transient $\mathrm{NO_x}$ emission reduction using exhaust oxygen concentration based control for a diesel engine." SAE paper 2005-01-0372, 2005.

[14] U. Christen, "Engineering aspects of H_∞ control," Ph.D. dissertation, ETH Zurich, 1996.

[15] J. C. Doyle, K. Glover, P. P. Khargonekar, and B. A. Francis, "State-space solutions to standard H_2 and H_∞ control problems," *IEEE Transactions on Automatic Control*, vol. 34, no. 8, pp. 831–847, 1989.

[16] H. Dym, T. T. Georgiou, and M. C. Smith, "Explicit formulas for optimally robust controllers for delay systems," *IEEE Transactions on Automatic Control*, vol. 40, no. 4, pp. 656–668, 1995.

[17] L. Eriksson, "Mean value models for exhaust system temperatures." SAE paper 2002-01-0374, 2002.

[18] J. Fredriksson and B. Egardt, "Backstepping control with integral action applied to air-to-fuel ratio control for a turbocharged diesel engine." SAE paper 2002-01-0195, 2002.

[19] S. Frei, "Performance and driveability optimization of turbocharged engine system," Ph.D. dissertation, ETH Zurich, 2004.

[20] S. García-Nieto, M. Martínez, X. Blasco, and J. Sanchis, "Nonlinear predictive control based on local model networks for air management in diesel engines," *Control Engineering Practice*, vol. 16, no. 12, pp.

1399–1413, 2008.

[21] H. P. Geering, *Regelungstechnik*, 6th ed. Springer-Verlag, 2004.

[22] H. P. Geering, "Concepts of LPV control with applications in automotive engine control," in *Proceedings of the IEEE International Symposium on Industrial Electronics – ISIE 2005*, Dubrovnik, Croatia, 2005, pp. 241–246.

[23] H. P. Geering and C. A. Roduner, "Entwurf robuster Regler mit der H_∞ Methode," *Bulletin SEV/VSE*, vol. 3, pp. 55–58, 1999.

[24] T. Glad and L. Ljung, *Control Theory, Multivariable and Nonlinear Methods.* Taylor & Francis, 2000.

[25] A. H. Glattfelder and W. Schaufelberger, *Control Systems with Input and Output Constraints.* Springer-Verlag, 2003.

[26] A. B. Greene and G. G. Lucas, *The Testing of Internal Combustion Engines.* English University Press Ltd., 1969.

[27] L. Guzzella and A. Amstutz, "Control of diesel engines," *IEEE Control Systems Magazine*, vol. 8, no. 9, pp. 55–71, 1998.

[28] L. Guzzella and C. H. Onder, *Introduction to Modeling and Control of Internal Combustion Engine Systems.* Springer-Verlag, 2004.

[29] L. Guzzella and A. Sciarretta, *Vehicle Propulsion Systems, Introduction to Modeling and Optimization.* Springer-Verlag, 2005.

[30] M. J. Hall, T. Diller, and R. Matthews, "Further development of an electronic particulate matter sensor and application to diesel engine transients." SAE Paper 2008-01-1065, 2008.

[31] J. B. Heywood, *Internal Combustion Fundamentals.* McGraw-Hill international edition, New York, 1998.

[32] F. P. Incropera and D. P. DeWitt, *Fundamentals of Heat and Mass Transfer*, 4th ed. John Wiley & Sons, Inc., 1996.

[33] M. Jankovic, M. Jankovic, and I. V. Kolmanovsky, "Constructive Lyapunov control design for turbocharged diesel engines," *IEEE Transactions on Control Systems Technology*, vol. 8, no. 2, pp. 288–299, 2000.

[34] N. F. Jerome and W. H. Ray, "High-performance multivariable control

strategies for systems having time delays," *AIChE Journal*, vol. 32, no. 6, pp. 914–931, 1986.

[35] T. Johnson, "Diesel engine emissions and their control: An overview," *Platinum Metals Review*, vol. 52, no. 1, pp. 23–37, 2008.

[36] N. Kato, Y. Hamada, and H. Kurachi, "Performance of thick film NO_x sensor on diesel and gasoline engines." SAE paper 970858, 1997.

[37] N. Kato, H. Kurachi, and Y. Hamada, "Thick film $Zr0_2$ NO_x sensor for the measurement of low NO_x concentration." SAE paper 980170, 1998.

[38] N. Kato, K. Nakagaki, and N. Ina, "Thick film ZrO_2 NO_x sensor." SAE Paper 960334, 1996.

[39] A. Kojima, K. Uchida, E. Shimemura, and S. Ishijima, "Robust stabilization of a system with delays in control," *IEEE Transactions on Automatic Control*, vol. 39, no. 8, pp. 1694–1698, 1994.

[40] A. J. Laub, M. T. Heath, C. C. Paige, and R. C. Ward, "Computation of system balancing transformations and other applications of simultaneous diagonalization algorithms," *IEEE Transactions on Automatic Control*, vol. 32, no. 2, pp. 115–121, 1987.

[41] D. L. Laughlin, K. G. Jordan, and M. Morari, "Internal model control and process uncertainty: Mapping uncertainty regions for SISO controller design," *International Journal of Control*, vol. 44, no. 6, pp. 1675–1698, 1986.

[42] J. Merten, "Mean-value modelling and robust control of the airpath of a turbocharged diesel engine," Ph.D. dissertation, University of Cambridge, 2003.

[43] B. C. Moore, "Principal component analysis in linear systems: Controllability, observability, and model reduction," *IEEE Transactions on Automatic Control*, vol. 26, no. 1, pp. 17–32, 1981.

[44] R. Moos, B. Reetmeyer, A. Hürland, and C. Plog, "Sensor for directly determining the exhaust gas recirculation rate - EGR sensor," *Sensors and Actuators B-Chemical*, vol. 119, no. 1, pp. 57–63, 2006.

[45] P. E. Moraal, I. V. Kolmanovsky, and M. J. van Nieuwstadt, "Model-

ing and identification of a current to vacuum transducer and VNT actuator," in *Proceedings of the 1999 IEEE/ASME International Conference on Advanced Intelligent Mechatronics*, Atlanta, 1999, pp. 257–262.

[46] M. Morari and E. Zafiriou, *Robust Process Control.* Prentice-Hall, 1989.

[47] S. Nakayama, T. Fukuma, A. Matsunaga, T. Miyake, and T. Wakimoto, "A new dynamic combustion control method based on charge oxygen concentration for diesel engines." SAE Paper 2003-01-3181, 2003.

[48] P. Ortner and L. Del Re, "Predictive control of a diesel engine air path," *IEEE Transactions on Control Systems Technology*, vol. 15, no. 3, pp. 449–456, 2007.

[49] R. Ravi, K. M. Nagpal, and P. P. Khargonekar, "H_∞ control of linear time-varying systems: a state-space approach," *SIAM J. Control and Optimization*, vol. 29, no. 6, pp. 1394–1413, 1991.

[50] C. A. Roduner, "H_∞-Regelung linearer Systeme mit Totzeiten," Ph.D. dissertation, ETH Zurich, 1997.

[51] C. A. Roduner, C. H. Onder, and H. P. Geering, "Automated design of an air/fuel controller for an SI engine considering the three-way catalytic converter in the H_∞ approach," in *Proceedings of the 5th Mediterranean Conference on Control and Systems*, Paphos, Cyprus, 1997, pp. 1–7.

[52] W. J. Rugh and J. S. Shamma, "Research on gain scheduling," *Automatica*, vol. 36, pp. 1401–1425, 2000.

[53] A. Schilling, "Model-based detection and isoliation of faults in the air and fuel paths of common-rail DI diesel engines equipped with a lambda and a nitrogen oxide sensor," Ph.D. dissertation, ETH Zurich, 2008.

[54] A. Schilling, A. Amstutz, C. H. Onder, and L. Guzzella, "A real-time model for the prediction of the NO_x emissions in DI diesel engines," in *Proceedings of the 2006 IEEE International Conference on Control Applications*, Munich, Germany, 2006, pp. 2042–2047.

[55] A. Schilling, A. Amstutz, C. H. Onder, and L. Guzzella, "Model-based detection and isolation of faults due to ageing in the air and fuel paths of common-rail DI diesel engines equipped with a lambda and a nitrogen oxides sensor," *IMechE Part D - Journal of Automobile Engineering*, vol. 222, no. 1, pp. 101–118, 2008.

[56] W. Schindler, C. Haisch, H. A. Beck, R. Niessner, E. Jacob, and D. Rothe, "A photoacoustic sensor system for time resolved quantification of diesel soot emissions." SAE paper 2004-01-0968, 2004.

[57] J. S. Shamma and M. Athans, "Gain scheduling: Potential hazards and possible remedies," *IEEE Control Systems Magazine*, vol. 12, no. 3, pp. 101–107, 1992.

[58] O. J. M. Smith, "Closer control of loops with dead time," *Chemical Engineering Progress*, vol. 53, no. 5, pp. 217–219, 1957.

[59] A. Stefanopoulou, I. V. Kolmanovsky, and J. S. Freudenberg, "Control of variable geometry turbocharged diesel engines for reduced emissions," *IEEE Transactions on Control Systems Technology*, vol. 8, no. 4, pp. 733–745, 2000.

[60] G. Szita and C. K. Sanathanan, "A model matching approach for designing decentralized MIMO controllers," *Journal of The Franklin Institute*, vol. 337, no. 6, pp. 641–660, 2000.

[61] D. R. Tree and K. I. Svensson, "Soot processes in compression ignition engines," *Progress in Energy and Combustion Science*, vol. 33, no. 3, pp. 272–309, 2007.

[62] V. I. Utkin, H. C. Chang, I. V. Kolmanovsky, and J. A. Cook, "Sliding mode control for variable geometry turbocharged diesel engines," in *Proceedings of the American Control Conference*, Chicago, Illinois, 2000, pp. 584–588.

[63] M. J. van Nieuwstadt, I. V. Kolmanovsky, P. E. Moraal, A. Stefanopoulou, and M. Jankovic, "EGR-VGT control schemes: Experimental comparison for a high-speed diesel engine," *IEEE Control Systems Magazine*, vol. 20, no. 3, pp. 63–79, 2000.

[64] M. J. van Nieuwstadt, P. E. Moraal, I. V. Kolmanovsky, A. Stefanopoulou, P. Wood, and M. Criddle, "Decentralized and multivari-

able designs for EGR-VGT control of a diesel engine," in *IFAC Workshop, Advances in Automotive Control*, Loudenville, Ohio, 1998, pp. 191–196.

[65] K. Vantine, U. Christen, K. Glover, and N. Collings, "Analysis of an event-based diesel engine model for control purposes," in *3rd IFAC Workshop on Advances in Automotive Control*, Karlsruhe, Germany, 2001.

[66] Q. G. Wang, B. Zou, and Y. Zhang, "Decoupling Smith predictor design for multivariable systems with multiple time delays," *Trans IChemE*, vol. 78, part A, pp. 565–572, 2000.

[67] X. Wei and L. del Re, "Gain scheduled H_∞ control for air path systems of diesel engines using LPV techniques," *IEEE Transactions on Control Systems Technology*, vol. 15, no. 3, pp. 406–415, 2007.

Curriculum Vitae

Personal Data

Name:	Ezio Alfieri
Date of birth:	August 30, 1979
Citizen of:	Pedrinate TI, Switzerland
Parents:	Claudio Alfieri and Vanda Alfieri-Solcà

Education

1985–1990	Primary school in Chiasso TI, Switzerland
1990–1994	Secondary school in Chiasso TI, Switzerland
1994–1998	High school in Mendrisio TI, Switzerland
1998	Matura certificate, type C
1998	Military service
1998–2003	Studies in mechanical engineering, Swiss Federal Institute of Technology (ETH) Zurich, Switzerland Major in control systems and nanotechnologies
2003	Diploma as *Dipl. Masch.-Ing. ETH*
2003–2009	Doctoral student and research assistant at the Measurement and Control Laboratory, ETH Zurich, Switzerland

Professional Experience

2002	Development of a test software for the ultrasonic transit time flow measurement sensor for Rittmeyer AG, Zug, Switzerland
since 2007	System engineer at Oerlikon Contraves AG, Zurich, Switzerland